

From Lab to Fab: Optimization of a Cost-Effective and Scalable Fabrication Process for Perovskite Solar Cells

Dissertation presented to the Faculty of Engineering of the University of Porto for obtaining the degree of

Doctor in Chemical and Biological Engineering

by

Ana Cristina Ornelas Teixeira

Luísa Manuela Madureira Andrade Silva, Assistant Professor – Supervisor

Adélio Miguel Magalhães Mendes, Full Professor – Co-supervisor

Dávid Forgács, PhD – Co-supervisor



Department of Chemical Engineering,
Faculty of Engineering, University of Porto,
Portugal



SAULE Technologies,
Poland

2023

The work developed in this thesis was financially supported by Foundation for Science and Technology (FCT) through the PhD grant SFRH/BD/148194/2019 (1st and 2nd chapter), by SAULE Technologies (3rd and 4th chapters) and by projects: i) SolarPerovskite (NORTE-01-0145-FEDER-028966) funded by European Regional Development Fund (ERDF) funds through North Portugal Regional Operational Programme (NORTE 2020) by national funds (PIDDAC) through FCT/MCTES; ii) InPSC (PTDC/EQU-EQU/4193/2021) funded by national funds through the FCT/MCTES (PIDDAC); iii) WinPSC (POCI-01-0247-FEDER-017796) co-funded by ERDF, through the Operational Program for Competitiveness and Internationalization (COMPETE 2020), under Portugal 2020 Partnership Agreement; iv) GOTSolar project (687008) European Union's Horizon 2020 Program, through a FET Open research and innovation; v) LA/P/0045/2020 (ALiCE), UIDB/00511/2020 and UIDP/00511/2020 (LEPABE), funded by national funds through FCT/MCTES (PIDDAC); v) POIR.01.01.01-00-1482/19-00 from the ERDF provided by the National Centre of Research and Development (NCBR).



UNIÃO EUROPEIA

Fundo Europeu de
Desenvolvimento Regional



ACKNOWLEDGMENTS

I would like to thank the supervision of Professor Luísa Andrade and Professor Adélio Mendes during my stay at the University of Porto, and of Doctor Dávid Forgács during my period at SAULE Technologies. I want to thank my family, especially my parents and sister, my co-workers and friends in Madeira, Porto and in Wroclaw, for all the support, friendship, and kindness during the development of this Ph.D. Special thanks to André, Carolina, Julia, and Melissa.

To José Manuel Teixeira
(1962-2023)

PREFACE

This thesis is composed of five chapters: an introduction chapter based on a published review article; three chapters discussing the results of the scientific plan executed (each chapter corresponding to a published/submitted scientific article); and a final chapter with the general conclusions and prospects of future work.

The published documents that originated chapter 1 and chapter 2 of the present thesis were developed at the Laboratory for Process Engineering, Environment, Biotechnology and Energy (LEPABE) facilities, in the Chemical Engineering Department of the Faculty of Engineering - University of Porto (FEUP), between 2019 and 2020 and under the FCT (Foundation for Science and Technology) grant SFRH/BD/148194/2019. The work that originated chapters 3 and 4 was developed at (and financed by) company SAULE Technologies in Wroclaw, Poland, between 2021 and 2023. Chapter 3 was done in collaboration with six other research institutions: i) LEPABE; ii) Saule Research Institute; iii) Centre for Hybrid and Organic Solar Energy, University of Rome “Tor Vergata” (CHOSE); iv) Freiburg Materials Research Center (FMF), University of Freiburg; v) Fraunhofer Institute for Solar Energy Systems (Fraunhofer ISE); and vi) the German company Solaveni GmbH.

The work developed in chapter 3 was also used for a high-impact joint paper (in which the candidate is a co-author) led by Fraunhofer ISE and in collaboration with six other research institutes, and supported the development of the patent EP21461626.0 filed on November 2021 to the European Patent Office (EPO). Furthermore, SAULE Technologies designed and ordered a 20 m long pilot-line based on slot-die coating to fabricate perovskite modules (to be delivered in 2023), and the knowledge acquired in chapter 4 will be essential for the initial optimization of that line. Moreover, for the development of chapter 4, three weeks were spent on secondment at the SPECIFIC lab in Swansea University under the supervision of Prof. Trystan Watson, an opportunity funded by the Viperlab project.

CONTENTS

Abstract	XIII
Sumário	XV
List of abbreviations and symbols	XVII

CHAPTER 1

INTRODUCTION

1.1 Perovskite Solar Cells	3
1.2. Motivation	4
1.3. Working Principles	8
1.3.1. PSC operation	10
1.3.2. PSC structure	14
1.4. Commercialization challenges	16
1.4.1. Costs	16
1.4.2. Stability	20
1.4.3. Upscaling	25
1.4.4. Environmental Impact	29
1.5. Applications	35
1.5.1. Space applications	36
1.5.2. Outdoor applications	37
1.5.3. Indoor applications	37
1.6. Scope of the thesis	41
References	43

CHAPTER 2

CARBON BASED ELECTRODE FOR RIGID PEROVSKITE SOLAR CELLS

2.1. Introduction	55
2.2. Experimental Section	57
2.2.1. Materials and rigid PSC fabrication	57
2.2.2. Characterization methods	61
2.3. Results and discussion	62
2.4. Conclusion	73
Acknowledgments	74
References	75

CHAPTER 3

OPTIMIZATION OF A HIGHLY EFFICIENT AND FLEXIBLE PEROVSKITE SOLAR CELL FOR INDOOR APPLICATIONS

3.1. Introduction	79
3.2. Experimental Section	81
3.2.1. Materials and flexible PSC fabrication	81
3.2.2. Characterization methods	82
3.3. Results and discussion	85
3.3.1. Perovskite layer characterization	85
3.3.2. Photovoltaic performance	88
3.3.3. Device opto-electrochemical characterization	92
3.3.4. Stability tests	103
3.4. Conclusion	109
Acknowledgments	110
References	111

CHAPTER 4

FABRICATION OF A FLEXIBLE PEROVSKITE SOLAR CELL BY SLOT-DIE COATING IN AMBIENT CONDITIONS

4.1. Introduction	115
4.2. Experimental Section	117
4.2.1. Materials and experimental procedure	117
4.2.3. Characterization methods	121
4.3. Results and discussion	123
4.3.1. Solutions optimization	123
4.3.2. Pre-treatment	130
4.3.3. Slot-die coating	132
4.3.4. Characterization	137
4.4. Conclusion	141
Acknowledgements	141
References	142

CHAPTER 5

GENERAL CONCLUSIONS AND OUTLOOK	147
---------------------------------	-----

ABSTRACT

The fast progress of Perovskite Solar Cells (PSC) is grounded on their very high power conversion efficiency under different lighting conditions, high stability concerning intrinsic factors, low production cost and the use of Earth abundant materials; moreover, this technology has advantages on decentralized production. Operation under low-light conditions is of particular interest since PSCs have already surpassed the efficiency of the well-established amorphous silicon technology. However, PSC's industrialization will only be possible if the manufacturing process of the whole device is compatible with mass production.

The work presented in this thesis aims to contribute to the lab-to-fab transition of PSC, by developing step wise a large-scale fabrication process for a low-cost, stable, and efficient PSC. An introductory chapter briefly presents the motivation for working in this technology, the working principles of solar cells, possible applications for PSCs, and the current state-of-the-art of the commercialization challenges. The following 3 chapters describe and discuss the results of the experimental work plan developed to reach the final device.

The starting point is a standard mesoporous n-i-p PSC with a glass substrate and an evaporated gold electrode. The first task is to replace the expensive metallic electrode with a highly conductive carbon paper, aiming for a low-cost and stable device. The carbon-based PSC displayed a maximum PCE of 12.9 %, which corresponds to 89 % of the PCE obtained with the metallic electrode.

Then, the research was redirected towards one of the most promising applications for PSC – indoor applications. A low-temperature fabrication process for small cells with flexible substrates was developed and optimized. The perovskite composition was tuned to maximize the light absorption at low-light conditions. The maximum PCE obtained at 1000 lux was 30.9 % for a PSC with a metallic electrode, 25.4 % for a PSC with a carbon-based electrode, and 23.1 % for a PSC without hole-transport material (HTM) and with a carbon-based electrode. The latter PSC maintained 84 % of its initial PCE after 1000 hours at maximum power

point tracking, and lost virtually no efficiency after 1000 hours at 85 °C. At this point, the stability, cost of materials and energy requirements for the fabrication steps are already close to those necessary for industry.

The last chapter describes the development of an experimental procedure to fabricate perovskite devices in large scale, using a slot-die coating technique in ambient atmosphere and using a flexible HTM-free carbon-based architecture. For each active layer, the influence of the operational and rheological parameters on the low-flow limit was studied, aiming for a stable coating at 1 m min⁻¹. The optimized procedure resulted in a PSC with a maximum PCE of 16.5 % at 1000 lux, that kept 92 % of its initial PCE after 550 h under maximum power point tracking. By slot-die coating a 2D perovskite passivation layer, the PCE was increased up to 18.6 %.

Overall, the step-by-step plan designed and executed resulted in a simple, flexible, and stable device, manufactured using exclusively large-scale processes at a low cost, and with a moderately high efficiency in indoor environments. The work presented in this thesis will support the transition of perovskite technology from lab-scale into large-scale manufacturing in a 20 m long roll-to-roll pilot line at the company SAULE Technologies, which is scheduled to start by the end of 2023.

SUMÁRIO

O rápido progresso das Células Solares de Perovskita (PSC) no que diz respeito ao desempenho fotovoltaico sob diferentes condições de iluminação, sua estabilidade e estratégias de aumento de área demonstram o grande potencial desta tecnologia para transitar para escala industrial. A operação sob condições de baixa luz é de particular interesse, pois as PSCs já superaram a eficiência da tecnologia bem estabelecida de silício amorfo. No entanto, a industrialização das PSC só será possível se o processo de fabricação de todo o dispositivo for compatível com a sua produção em larga escala.

O trabalho apresentado nesta tese visa contribuir para a transição *lab-to-fab* das PSC, desenvolvendo passo a passo um processo de fabricação de grande escala de uma PSC de baixo custo, estável e eficiente. Um capítulo introdutório apresenta brevemente a motivação para trabalhar nesta tecnologia, os princípios de funcionamento das células solares, possíveis aplicações para PSCs e o estado atual da arte dos desafios de comercialização. Os três capítulos seguintes descrevem e discutem os resultados do plano de trabalho experimental desenvolvido para chegar ao dispositivo final.

O ponto de partida é uma PSC n-i-p mesoporosa padrão com um substrato de vidro e um eletrodo de ouro evaporado. A primeira tarefa é substituir o eletrodo metálico por um papel de carbono altamente condutor, visando um dispositivo estável e de baixo custo. A PSC à base de carbono apresentou uma eficiência máxima de conversão de energia (PCE) de 12,9 %, o que corresponde a 89 % do PCE obtido com o eletrodo metálico.

A pesquisa foi então redirecionada para uma das aplicações mais promissoras para PSC – dispositivos fotovoltaicos para interiores. Um processo de fabricação de baixa temperatura para células pequenas com substratos flexíveis foi desenvolvido e otimizado. A composição de perovskita foi ajustada para maximizar a absorção de luz em condições de baixa luz. A PCE máxima obtido a 1000 lux foi de 30,9 % para uma PSC com eletrodo metálico, 25,4 % para uma

PSC com elétrodo à base de carbono e 23,1 % para uma PSC sem material transportador de lacunas (HTM) e com um elétrodo à base de carbono. A última PSC manteve 84 % da sua PCE inicial após 1000 horas no rastreamento do ponto de potência máximo e praticamente não perdeu eficiência após 1000 horas a 85 °C. Neste ponto, a estabilidade, o custo dos materiais e os requisitos de energia para as etapas de fabricação já estão próximos dos necessários para a indústria.

Em seguida, segue o aumento de escala da arquitetura com substrato flexível, sem HTM e com elétrodo de carbono. O último capítulo descreve o desenvolvimento de um procedimento experimental para fabricar dispositivos de perovskita em larga escala, usando uma técnica de *slot-die* em atmosfera ambiente. Para cada camada ativa, foi estudada a influência dos parâmetros operacionais e reológicos no limite de baixo-fluxo, visando um revestimento estável a 1 m min⁻¹. O procedimento otimizado resultou numa PSC com PCE máxima de 16,5 % a 1000 lux, que manteve 92 % da sua PCE inicial após 550 h sob rastreamento de ponto de potência máxima. A PCE foi aumentado para 18,6 % através da deposição por *slot-die* de uma camada de passivação de perovskita 2D.

No geral, o plano passo a passo executado resultou num dispositivo simples, flexível, estável, de baixo custo, com eficiência moderadamente alta em interiores, e que pode ser fabricado usando exclusivamente processos de grande escala. O trabalho apresentado nesta tese apoiará a transição da tecnologia de perovskita de escala laboratorial para fabricação em larga escala numa linha piloto *roll-to-roll* de 20 m de comprimento na empresa SAULE Technologies, com início previsto para o final de 2023.

LIST OF ABBREVIATIONS AND SYMBOLS

Abbreviations	Definition
2D	two dimensional
3D	three dimensional
a-Si	amorphous silicon
AFM	atomic force microscopy
ALD	atomic layer deposition
bn	billion
CdTe	cadmium telluride
CIGS	copper indium gallium selenide
CVD	chemical vapor deposition
CP1	carbon paper H24C5 from Freudenberg
CP2	carbon paper H14C10 from Freudenberg
CP3	carbon paper 28BC from SIGRACET®
EIS	electrochemical impedance spectroscopy
ETM	electron transport material
fwd	forward
GB	glove box
HTM	hole transport material
IoT	Internet of Things
I-V	current-voltage
J-V	current density-voltage
LED	light emitting diode
MPPT	maximum power point tracking
NIR	near-infrared
NPs	nanoparticles
OD	optical density filters
OWRK	Owens, Wendt, Rabel and Kaelble
prvk	perovskite
PL	photoluminescence
PSC	perovskite solar cell
PTFE	polytetrafluoroethylene
PV	photovoltaic
QFLS	quasi-fermi level splitting
R2R	Roll-to-roll

rev	reverse
ROI	regions of interest
S2S	Sheet-to-sheet
SEM	scanning electron microscope
TCO	transparent conductive oxide
TPC	transient photocurrent decay
TPV	transient photovoltage decay
UV	ultraviolet
UV-Vis	ultraviolet-visible
XPS	X-ray photoelectron spectroscopy
XRD	X-ray diffraction

Substances	Definition
2-ME	2-methoxyethanol
2PACz	[2-(9 <i>H</i> -Carbazol-9-yl)ethyl]phosphonic Acid
4F-PEAI	4-fluoro-phenethylammonium iodide
5-AVAI	5-ammonium valeric acid iodide
ACN	acetonitrile
Al ₂ O ₃	aluminum (III) oxide
Au	gold
BAI	n-butylammonium iodide
BCP	bathocuproine
Br ⁻	bromide
C60	buckminsterfullerene
Ca	calcium
Cl ⁻	chlorine
Cs	cesium
Cu	copper
CuPc	copper phthalocyanine
CuSCN	copper(I) thiocyanate
DBC-OMeDPA	<i>N</i> ^β , <i>N</i> ^β , <i>N</i> ^δ , <i>N</i> ^δ , <i>N</i> ¹¹ , <i>N</i> ¹¹ , <i>N</i> ¹⁴ , <i>N</i> ¹⁴ -octakis(4-methoxyphenyl)dibenzo-[<i>g,p</i>]chrysene-3,6,11,14-tetraamine
DFH	<i>N</i> ^ρ , <i>N</i> ^ρ , <i>N</i> ^τ , <i>N</i> ^τ -tetra- <i>p</i> tolylspiro[fluorene-9,20-[1,3]dioxolane]-2,7-diamine
DMF	<i>N,N</i> -dimethylformamide
DMSO	dimethyl sulfoxide

DTPC13-ThTPA	dithieno[3,2-b:2',3'-d]pyrrole (DTP) cored molecular semiconductor
DTP-C6Th	dithieno[3,2-b:2',3'-d]pyrrol-cored small molecule
FA ⁺	formamidinium
Fe	iron
FK209	tris(2-(1 <i>H</i> -pyrazol-1-yl)-4- <i>tert</i> -butylpyridine)cobalt(III) tri[bis(trifluoromethane)sulfonimide]
FTO	fluorine-doped tin oxide
GaAs	gallium arsenide
GBL	γ -butyrolactone
HMPA	hexamethylphosphoramide
I ⁻	iodide
ImAcHCl	imidazole hydrochloride
IPA	2-propanol
ITCPTC-Th	(3,9-bis(2- methylene-(3-(1,1-dicyanomethylene)-cyclopentane-1,3- dione-[<i>c</i>]-thiophen))-5,5,11,11-tetrakis(4-hexylphenyl)- dithieno[2,3-d:2',3'- <i>d'</i>]- <i>s</i> -indaceno[1,2-b:5,6- <i>b'</i>]dithiophene) modified with thiophene
ITO	indium tin oxide
IZO	indium zinc oxide
KOH	potassium hydroxide
LiTFSi	lithium bis(trifluoromethanesulfonyl)imide
MA ⁺	methylammonium
MAPbBr ₃	methylammonium lead bromide
MeO-2PACz	[2-(3,6-Dimethoxy-9 <i>H</i> -carbazol-9-yl)ethyl]phosphonic acid
MPA-BTTI	2,8-bis(4-(bis(4-methoxyphenyl)amino)phenyl)-5-dodecyl-4 <i>H</i> -thieno[2',3':4,5]cthieno[3,2- <i>c</i>]thieno[2',3':4,5]thieno[2,3- <i>e</i>]azepine-4,6(5 <i>H</i>)-dione
N ₂	nitrogen
NDI-ID	<i>N,N'</i> -Bis(1-indanyl)naphthalene-1,4,5,8-tetracarboxylic diimide
NH ₂ -TiO ₂	amino-functionalized titanium dioxide
NiO _x	nickel oxide
NMP	<i>n</i> -methyl-2-pyrrolidone
OAI	<i>n</i> -octylammonium iodide
OMe-TATPyr	1,3,6,8-tetrakis[5-(<i>N,N</i> -di(<i>p</i> -methoxyphenyl)amino- <i>p</i> -phenyl)- thiophen-2-yl] pyrene

P3CT-Rb	Rb doped Poly[3-(4-carboxybutyl)thiophene-2,5-diyl]
Pb	lead
PCBM	phenyl-C61-butyric acid methyl ester
PDMS	polydimethylsiloxane
PDO2	phenothiazine 5,5-dioxide
PEAI	phenethylammonium iodide
PEDOT:PSS	poly(3,4-ethylenedioxythiophene) polystyrene sulfonate
PET	polyethylene terephthalate
PHPT-py	poly(1-(4-hexylphenyl)-2,5-di(thiophen-2-yl)-1H-pyrrole)
PTAA	poly[bis(4-phenyl)(2,4,6-trimethylphenyl)amine]
Rb	rubidium
Si	silicon
Sn	tin
SnO ₂	tin dioxide
SnS ₂	tin(IV) sulfide
spiroOMeTAD	2,2',7,7'-Tetrakis[N,N-di(4-methoxyphenyl)amino]-9,9'-spirobifluorene
Sr	strontium
TFB	poly[(9,9-dioctyl-fluorenyl-2,7-diyl)-co-(4,4'-(N-(4-secbutylphenyl) diphenylamine)]
ThMAI	2-thiophenemethylammonium iodide
TiO ₂	titanium dioxide
TMAH	tetramethylammonium hydroxide
WO ₃	tungsten trioxide
Zn	zinc
ZnO	zinc oxide

Variables	Definition	Units
μ	viscosity	cP
Ca	capillary number	-
CPE	constant phase element	F
E_{fn}	electron quasi-fermi level	eV
E_{fp}	hole quasi-fermi level	eV
EQE	external quantum efficiency	%

FF	fill factor	%
F_{ph}	incident photon-flux density	$\mu\text{mol m}^{-2} \text{s}^{-1}$
H_0	gap	μm
I	output current	mA
I_0	dark saturation current	mA
I_{diode}	current that passes through the diode	mA
I_L	light generated current	mA
I_{MP}	current at the maximum power point	mA
I_{SC}	short circuit current	mA
J_{SC}	short-circuit current density	mA cm^{-2}
n_{id}	ideality factor	-
P	power output	mW
PCE	power conversion efficiency	%
P_{in}	incident power	mW
P_{MP}	power at the maximum power point	mW
Q	pumping rate	$\mu\text{L min}^{-1}$
R	resistor element	Ω
r_A	effective ionic radius for A cation	\AA
r_B	effective ionic radius for B cation	\AA
r_X	effective ionic radius for X anion	\AA
SPO	stabilized power output	%
t	thickness	μm
t	Goldschmidt tolerance factor	-
T	temperature	$^{\circ}\text{C}$
t_{wet}	wet film thickness	μm
V	coating speed	m min^{-1}
v	volume	mL
V_{MP}	voltage at the maximum power point	V
V_{OC}	open-circuit voltage	V
V_T	thermal voltage	V
WF	work-function	J
wt	weight	mg
σ	surface energy	mN m^{-1}

Constants	Definition	Units
k	Boltzmann constant	$\text{m}^2 \text{kg s}^{-2} \text{K}^{-1}$
q	elementary charge	C

Subscripts	Definition
A	cation A
B	cation B
f	final value
hf	high frequencies
i	initial value
in	incident
lf	low frequencies
max	maximum
min	minimum
MP	maximum power point
OC	open-circuit
s	series
SC	short-circuit
X	anion X

CHAPTER 1

INTRODUCTION

Adapted from the peer-reviewed article:

Selection of the ultimate perovskite solar cell materials and fabrication processes towards its industrialization: A review

Cristina Teixeira, Diogo Castro, Luísa Andrade, Adélio Mendes; Energy Science & Engineering **10** (2020) p: 1478-1525.

INTRODUCTION

1.1. Perovskite Solar Cells

Organic-inorganic perovskites were first studied by Weber in 1978^{1, 2} but only in 2006 this material was used as photovoltaic (PV) absorber by Miyasaka and co-workers.³ These authors were interested in the self-organization potential of perovskite on the nanoporous TiO₂ layer of dye-sensitized cells, reporting a power conversion efficiency (PCE) of 2.2 % for devices prepared with methylammonium lead bromide (MAPbBr₃). Three years later, by replacing bromine for iodine, they were able to increase the PCE to 3.8 %.⁴ This discovery triggered a strong interest in using perovskite as a light absorbing material to generate power. Throughout the next years, different research groups worldwide kept developing this technology, resulting in an ultra-fast progress with efficiency records being broken almost every year. Ten years after the Miyasaka's publication, perovskite solar cell PCE surpassed 25 %, being now among the most efficient thin-film solar cells and competing closely to the well-established crystalline silicon technology. In 2023, the Ulsan National Institute of Science and Technology in South Korea reached 26.1 % (certified 25.7 %), which is the current PCE record.⁵

Increasing the PV performance under 1 sun has been the main research focus of PSC development. However, with the approaching of this technology to industrialization phase, there are other factors that must be also considered, namely: environmental and operational stability, cost of materials and of manufacturing processes, large-scale deposition methods and the environmental

impact. Industrial production of solar modules based on perovskite will only be feasible if results obtained in all of these fields fulfill the minimum requirements. Furthermore, the success of the PSC's entry into the market will also depend on its final application. For instance, indoor PVs are a promising niche market for PSC given their high performance under indoor lighting, that actually surpasses the efficiency of the mature amorphous silicon technology.⁶ Also, PSCs can be fabricated in flexible lightweight substrates, which broadens the range of possible applications for PSCs, like wearables and building-integrated PVs.⁷

The following sub-chapters will clarify the motivation for working on the lab to fab transition of PSCs, explain the working principles and operation of a solar cell, and provide an overview of the latest advancements in the main research topics related with PSC industrialization: stability, costs, scalability, and environmental impact; so a clear picture of the current state of the art of the PSC commercialization challenges is depicted. Furthermore, some promising and attractive applications for this specific PV technology are also identified and discussed in the final subchapter.

1.2. Motivation

Looking into the PV energy market by technology – Figure 1 – it is evident the monopoly of the crystalline silicon (Si) solar panels, owning a worldwide market share close to 95 %.⁸ These technologies started being developed in 1954 as a power source for space equipment and just became viable as a terrestrial energy source at the mid-1970s.^{9, 10} Recently, the urge to fight climate change and reduce the carbon footprint has increased, mainly due to the change of the society's mindset about sustainable development coupled with government incentive regulations. Consequently, the interest in building solar power plants and also the sales of domestic PV panels are expected to increase in the following years.

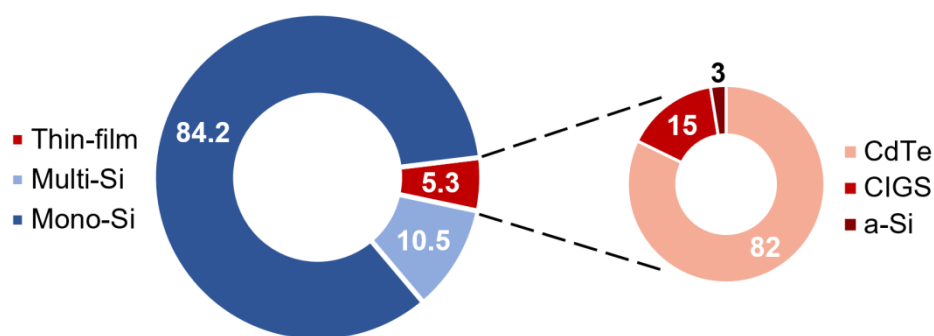


Figure 1 - Percentage of global annual production by technology in 2022.⁸

Indeed, silicon PV technology is being effective at fulfilling its duty: provide clean energy on a massive scale. Currently, there is no other type of solar cell technology good enough to compete against it on a cost of electricity basis. However, like every technology, it has its own drawbacks. First, China is the world's largest producer of silicon for solar panels (produced from extracted silicon dioxide), accounting for two-thirds of the global silicon production. This centralization of solar industries makes it difficult for other countries to grow in this industry sector, resulting in a market monopolization by one single country.¹¹ Second, after extraction, silicon dioxide undergoes a highly energetic and expensive purification process at ~ 1400 °C, usually powered by coal or other fossil fuel-burning plants.¹² This means that silicon technology takes approximately 1 year to generate the equivalent amount of primary energy used to fabricate it.^{8, 13} Besides, the silicon industry releases a highly toxic substance - silicon tetrachloride; and the thickness required for silicon to achieve the same absorption as thin-films like perovskite is significantly greater due to the indirect band gap of silicon: 25 μm of silicon is necessary, whereas only 500 nm is sufficient for perovskite.^{14, 15} Finally, due to their rigid shape, size, colour and opacity, silicon solar panels lack versatility regarding their final application. They may do well in solar farms, but bringing PVs to our cities without compromising buildings' aesthetics is a current struggle for architects and engineers.¹⁶

Regarding thin-film technologies, the commercially available ones include cadmium telluride (CdTe), copper indium gallium selenide (CIGS), gallium

arsenide (GaAs) and amorphous thin-film silicon (a-Si). CdTe is the most common thin-film technology – Figure 1 – because it is highly efficient (maximum PCE of 22.1 %), cheaper than silicon devices and is the thin-film technology with the lower payback time and carbon footprint. However, cadmium is toxic, and tellurium is scarce, which makes large-scale production unsustainable. CIGS demonstrated to be a good alternative to CdTe since it does not present toxic metals and is also highly efficient (maximum PCE of 23.3 %). Nevertheless, it is more expensive to fabricate and also has a scarce metal: indium. Despite its earth abundance, non-toxicity and relatively low cost, a-Si has a low market share due to its low efficiency (maximum PCE of 14.0 %). GaAs thin-film technology (although sometimes it is not considered to belong to this group) is the most efficient one (maximum PCE of 29.1 %) but since gallium is scarce and its manufacturing cost is very high, it is just produced for space applications.¹⁷⁻¹⁹

There is still the category called “emerging PVs” which are the most recent and immature PV technologies that are not yet commercialized (or commercialized with a very small market expression). This category comprises dye-sensitized, perovskite, quantum dots, organic and inorganic solar cells. Each technology presents critical challenges that are under development in several research centers worldwide and hopefully some of them will be on the market in the near future. Regarding the perovskite solar cells (PSC), they are the emerging PV with the efficiency (maximum PCE of 26.1 %) closer to the crystalline silicon solar panels and are even more efficient than CIGS, CdTe and a-Si thin-film technologies.¹⁸ In what concerns final usage, PSCs allow the possibility of different transparencies, colour-tuning and shape flexibility unlike silicon panels.¹⁷ However, there are still several critical features blocking their way through commercialization, specifically relating to costs, stability, upscaling and environmental impact – Figure 2.

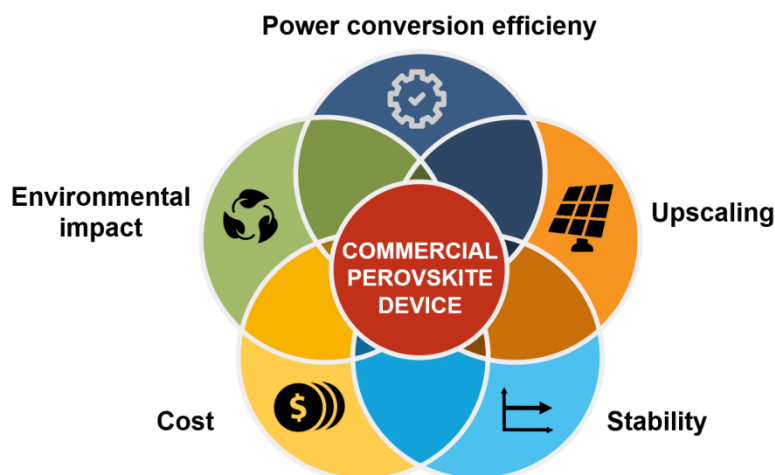


Figure 2 - Five research fields of the development of perovskite solar devices towards its commercialization.

Concerning costs, one of the big advantages of perovskite technology is the variety of materials and processes that can be used to prepare a PSC device without compromising its efficiency. It is possible to fabricate a PSC using low-cost materials (such as carbon electrodes and inorganic selective layers) and with no high energy consuming steps that require high temperatures or vacuum processes. Ye et al. reported a PSC with 17.78 % PCE using low-cost materials, no vacuum step and maximum temperature of 200 °C.²⁰ Then, stability is also a main topic of concern and Li et al.²¹ already reported a encapsulated PSC that operated 1 year under outdoor conditions with no loss of efficiency. Towards upscaling goal, SAULE Technologies already built a sun breaker wall using 32 m² of Perovskite Solar Modules.²² Finally, the use of lead is perhaps the major obstacle because of its high toxicity, but removing it from the configuration without significantly compromising the PCE has proved to be an uphill battle. Nevertheless, the load of this metal in a perovskite solar module is relatively low. Actually a square meter only contains ~0.4 grams of lead (300 nm thick perovskite layer), which compared to other commercial technical sources of lead is insignificant: one typical 14.5 kg lead-acid battery has 8.7 kg of lead.^{23, 24} Additionally, strategies can be adopted to avoid lead leakage from the perovskite solar module in case of an accident, such as the coating of lead-absorbing

materials or the use of a self-healing resin as sealant.²⁴⁻²⁶ Another important but sometimes overlooked fact is the end-of-life treatment, but PSCs can be totally recycled, and substrates can be re-used.^{27, 28}

Overall, the current energy crisis related to the unsustainable fossil fuels boosted the research of new clean technologies for generating electricity, like the PV energy technology. Although the PV market is dominated by the crystalline silicon technology, currently there are other technologies being developed. Even though there are still challenges that must be addressed concerning costs, stability, upscaling and environmental impact, PSCs are probably the most promising emerging PV technology, due to its features like high efficiency, versatility and easy fabrication process.

1.3. Working Principles

The core of a PV device is the photoactive semiconductor, which is responsible for the light absorption and its conversion into electrical energy. The semiconductor in a PSC device is the perovskite itself. Perovskite, named after the Russian mineralogist L.A. Perovski, has a specific crystal structure with the generic ABX_3 formula, where A, B and X refer to a large organic cation, a large inorganic cation, and a slightly smaller anion, respectively.²⁹ For use in solar cells, cation A is generally either a methylammonium (MA^+), formamidinium (FA^+), cesium (Cs^+), rubidium (Rb^+) cation or a combination of them, cation B is usually lead (Pb) and anion X is usually a halogen: iodine (I^-), bromine (Br^-), chlorine (Cl^-), or a mix of them.^{30, 31} The larger A cation occupies a cube-octahedral site shared with twelve X anions, while the smaller B cation is stabilized in an octahedral site shared with six X anions – Figure 3.³²

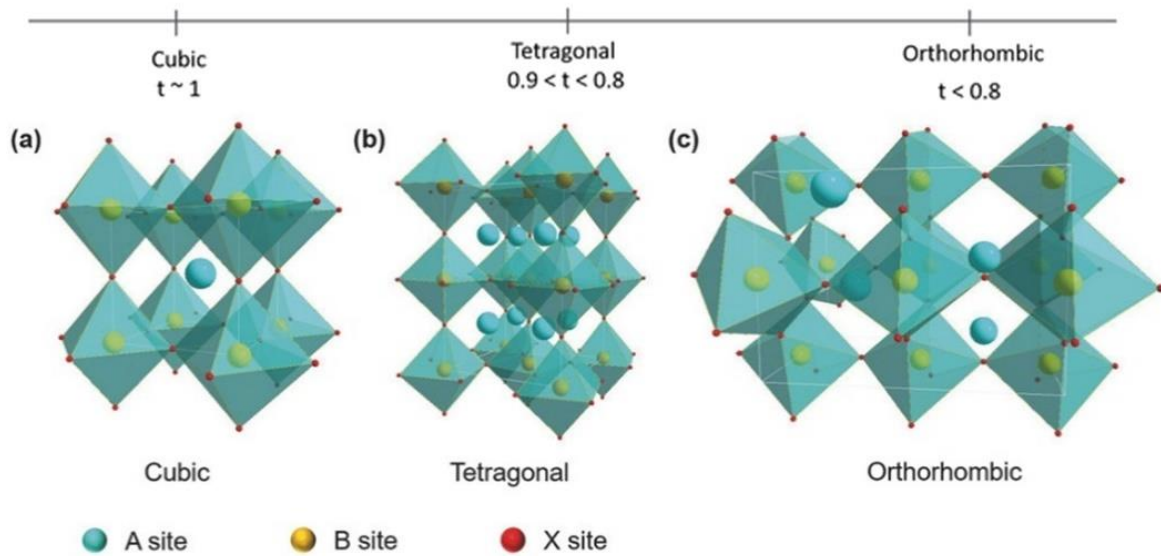


Figure 3 - Molecular structure of the perovskite crystal according to the Goldschmidt tolerance factor.³²

The anion/cation combination to form the perovskite structure is chosen based on its Goldschmidt tolerance factor t defined by the equation 1, where r_A , r_B and r_X are the effective ionic radius for A, B and X ions, respectively.³³

$$t = \frac{(r_A + r_X)}{\sqrt{2}(r_B + r_X)} \quad (1)$$

The tolerance factor must be between 0.9 and 1 to obtain the desired cubic lattice structure – Figure 3. The ions combination can also be optimized to achieve a suitable band gap and high stability to moisture, heat and oxygen. Besides being synthesized from abundant sources (inorganic and organic perovskite compounds), perovskites can have an impressive array of interesting properties depending on which atoms/molecules are used in the structure, including superconductivity, high magnetoresistance, large charge carrier mobility, high absorption coefficient, spin-dependent transport (spintronics) and defect tolerance.^{4, 29} However, any defect in the crystal structure may act as a site for undesired charge recombination, which decreases the correspondent PCE and stability. Thus, the perovskite crystallization must be engineered towards a defect-free, uniform and compact perovskite layer.

1.3.1. PSC operation

As mentioned before, the heart of any PV device is the semiconductor. In PSCs, when the perovskite film absorbs a photon, an electron located at the valence band is excited to the conduction band, creating a hole in the valence band, i.e. an electron/hole pair is created. Electrons are then driven to the n-i junction while holes are driven to the i-p junction through a hopping mechanism, creating thereby a planar-junction diode, which is responsible for charges separation – Figure 4a). Then, each charge carrier is extracted at the respective electrode and a directional electric charge flow is created, i.e. electricity. The perovskite band gap must not be too wide, otherwise only the most energetic photons (energy higher than the band gap energy) would be absorbed, but must also not be too small, because the smaller the band gap, the smaller the energy generated – Figure 4a).^{34, 35} Usually, solar cells are assessed through the PCE, which is the percentage of incident solar energy that is converted into usable electrical energy. To determine the PCE, the solar cell is subjected to a varying potential (V) and the output current (I) is recorded. The obtained curve is called the current-voltage (I - V) characteristic curve – Figure 5a) - and contains significant information about the operation of the solar cell, which will be briefly explained.³⁶

A solar cell can be observed as a diode, i.e., it only allows the current to flow in one direction, while blocking in the other direction – Figure 5c). The current blockage occurs due to the formation of an electrical field at the interface between the two terminals (n-contact and p-contact). When the potential applied overcomes the potential barrier caused by the electrical field, the diode breaks and current flows abruptly in the forbidden direction. This potential barrier in solar cells is near the open-circuit voltage (V_{OC}). Thus, when a solar cell is in the dark, the obtained current is null until reaching the V_{OC} – Figure 5b).

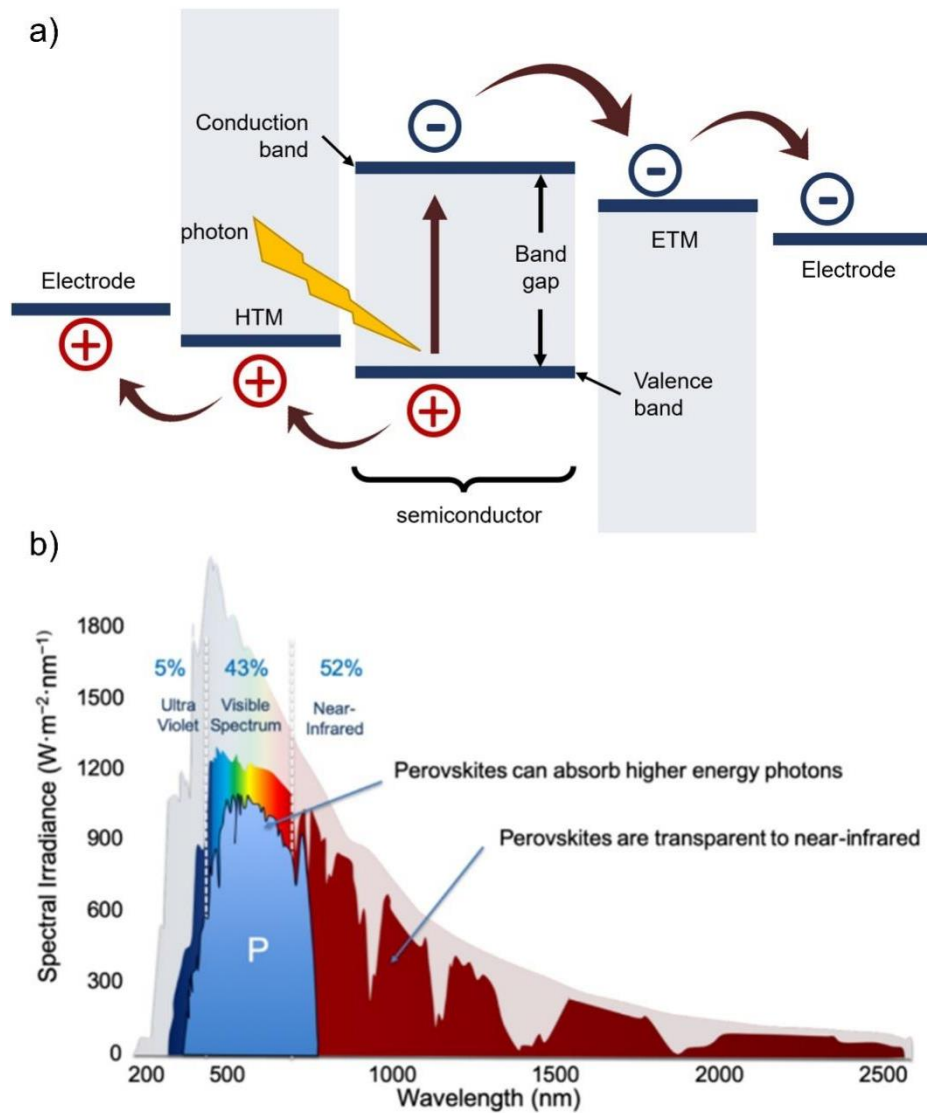


Figure 4 – a) Energy diagram of a PSC and b) spectral irradiance in function of the light wavelength, with the perovskite absorption spectrum represented.²⁹

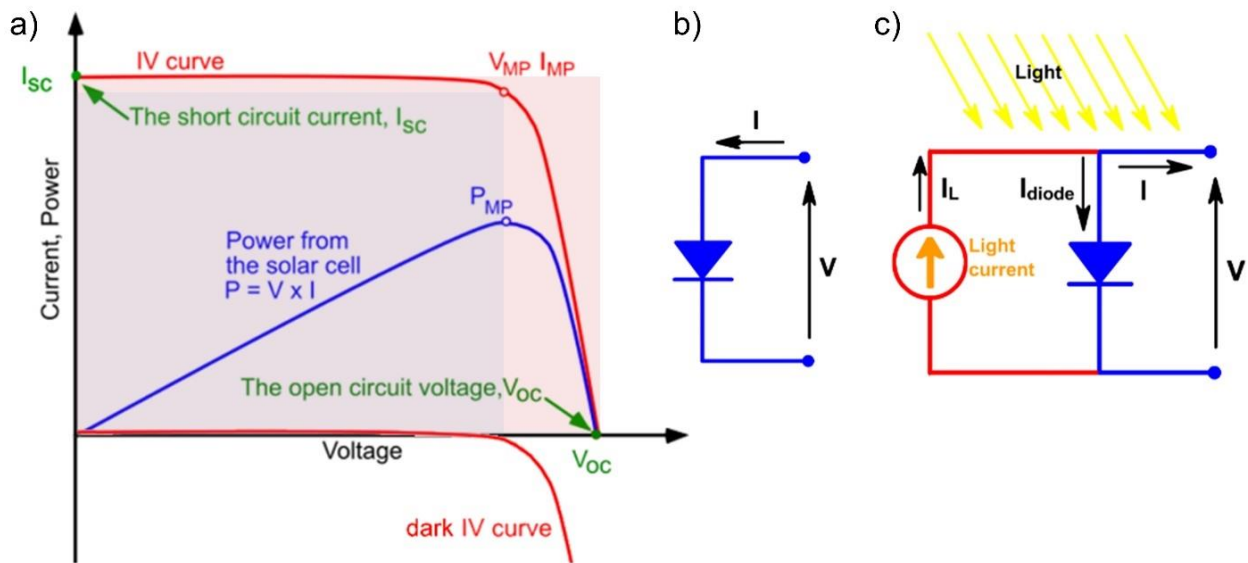


Figure 5 - a) Characteristic current-voltage curve in light and in dark, and the respective power curve. The PV parameters are identified. Equivalent electrical circuit of a PSC b) in dark and c) in the light.³⁷

When a solar cell is lighted, a new phenomenon happens: the generation of charge carriers (electron-hole pairs) as previously explained. Hence, in the I - V curve in the light, it can be seen the superposition of the diode curve and the light-generated current curve – Figure 5a). This curve is generically given by equation 2:^{36, 37}

$$I = I_0 \left[\exp\left(\frac{qV}{n_{id}kT}\right) - 1 \right] - I_L \quad (2)$$

where I is the output current, I_0 is the dark saturation current, q is the elementary charge (1.602×10^{-19} C), V is the applied potential, n_{id} is the ideality factor (1 for an ideal diode), k is the Boltzmann constant (1.38×10^{-23} J K⁻¹), T is the temperature, I_L is the light generated current, P is the power output produced by the solar cell, I_{sc} is the short circuit current, V_{oc} is the open-circuit voltage, P_{MP} is the power at the maximum power point, V_{MP} is the voltage at the maximum power point, I_{MP} is the current at the maximum power point and I_{diode} is the current that passes through the diode.

The PV parameters characterizing the solar performance that can be obtained from this curve are: short-circuit current (I_{sc}), open-circuit voltage (V_{oc}), fill factor (FF), and power conversion efficiency (PCE). J represents the current density, i.e. the current normalized for a specific area; in particular, J_{sc} is the current density produced at a zero potential, being the largest current which may be drawn from the solar cell. Its value is dependent on the light intensity and the series resistance throughout the whole device. V_{oc} is the maximum potential that a cell can provide and occurs when the current is null. Its value is related with the perovskite band gap and the electronic levels of the other active layers. The FF parameter is a measurement of the quality of the solar cell – the closer to 1, the better quality of the solar cell. It is the ratio between the blue and red squares in Figure 5a), and it is obtained by equation 3. Finally, the PCE is the most relevant parameter for performance assessment, and it is calculated with the other PV parameters by equation 4:^{36, 37}

$$FF = \frac{J_{MP} \cdot V_{MP}}{J_{SC} \cdot V_{OC}} \times 100 \quad (3)$$

$$PCE = \frac{J_{MP} \cdot V_{MP}}{P_{in}} \times 100 = \frac{J_{SC} \cdot V_{OC} \cdot FF}{P_{in}} \times 100 \quad (4)$$

where P_{in} is the incident power dependent of the sunlight illumination level.

For typical solar cells (single-junction) the maximum PCE possible to attain is about 30 %, denominated the theoretical Shockley–Queisser limit, which is calculated by the amount of electrical energy that is extracted per photon of incoming sunlight.³⁸ The solar cell's series and shunt resistances can also be extrapolated by the curve's slope near the V_{oc} and J_{sc} , respectively. For achieving a good PV performance, it is forecasted a low slope near the J_{sc} (which means that the cell has high shunt resistances, i.e. low current is being shunted in traps or defect sites throughout the current flow in the whole device) and a high slope near the V_{oc} (which means that the series resistances is low, i.e. the interfacial and bulk resistances of all layers are barely compromising the current flow).

1.3.2. PSC structure

For having a fully operational PSC device, several structures can be considered. Usually, two selective extraction layers are added at the perovskite layer interfaces - electron transport material (ETM) or hole transport material (HTM) - to decrease the non-radiative charge recombination and indeed increase the current density output. ETM acts as an n-type material whereas the HTM acts as a p-type material. The energy levels of these selective materials must be correctly aligned and close to the perovskite energy levels, to minimize the potential barrier for charge injection at the perovskite interfaces – Figure 4a). The bigger the energy levels difference, the bigger the loss in the open circuit voltage (V_{OC}) output, which consequently will decrease the PCE. Actually, in theory the V_{OC} is determined by the Equation: $V_{OC} = E_{fn} - E_{fp}$, in which E_{fn} refers to the electron quasi-fermi level (defined by the interactions between the ETM and perovskite layers) and E_{fp} refers to the hole quasi-fermi level (defined by interactions between the HTM and perovskite layer).³⁹ In particular cases, the layer on which the perovskite is deposited can also have a mesoporous morphology to increase the surface area for charge extraction and also to enhance perovskite crystallization.³⁵ Then, electrodes are incorporated at the selective layers' interface for extracting charges and closing the circuit. One of the electrodes must have a high transmittance to allow light to pass with minimum absorption – photoelectrode side. It is usually a glass coated with a transparent conductive oxide (TCO). The other electrode (back-contact) is usually a metal or a carbon material, since no transparency is required. In the case of tandem or semi-transparent devices, both electrodes require high transparency. These electrodes must be inert, have a high conductivity, chemical compatibility with the underlying layer and a suitable work function value.⁴⁰

There are several ways for assembling the aforementioned layers, the four most common ones are presented in Figure 6. The first PSCs being produced had a mesoporous n-i-p architecture, also known as conventional architecture, very similar to the solid-state dye-sensitized solar cells, in which the n-type material

composed by a compact layer and a mesoporous layer is in the glass side where the light is collected, and the p-type material in the back side – Figure 6a).³ Although this is the structure with more know-how, the current most efficient PSC is a planar n-i-p device, with no mesoporous layer – Figure 6b).⁵ If the p-type and n-type material exchange places, p-i-n planar device is created, also known as inverted PSC – Figure 6c). Furthermore, it is also possible to deposit macroporous extracting layers separated by a macroporous insulating material, and infiltrate the perovskite afterwards - mesoscopic architecture – Figure 6d). However, PCE of this last architecture is usually lower due to the uncontrolled and limited perovskite crystallization inside the tri-layer porous stack. For this thesis, the selected architectures were the mesoporous and planar n-i-p architecture.

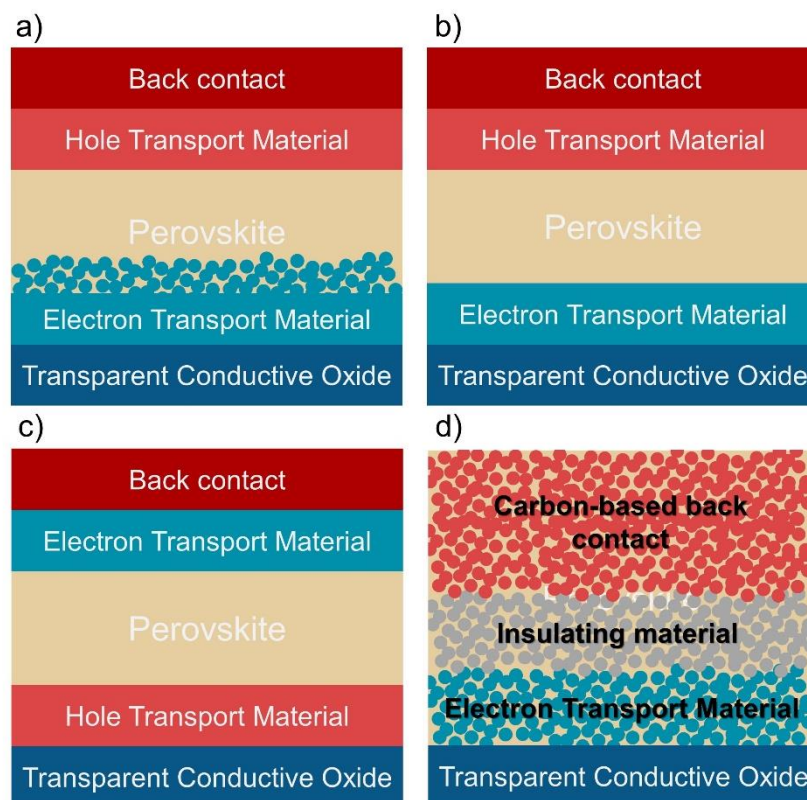


Figure 6 - Illustrations of the four most common PSC architectures: a) mesoporous n-i-p, b) planar n-i-p, c) planar p-i-n and d) n-i mesoscopic structure.

1.4. Commercialization challenges

1.4.1. Costs

A big advantage of the PSC is that there is a wide range of possible structures for building it, keeping always a high efficiency. Thus, despite the champion cells usually have very expensive materials in their configuration like gold or an expensive HTM – e.g. poly[bis(4-phenyl)(2,4,6-trimethylphenyl)amine (PTAA) or spiroOMeTAD, it is also possible to build a high-quality PSC out of cheap raw-materials. In this subchapter, a cost assessment to each PSC component will be made, to understand which are the low-cost materials that can still provide high efficiencies. Although a complete cost assessment also includes other parameters like the cost of the PV installation and other electrical components (like inverters and electrical wiring), only the material cost and the cost associated to the production process (energy consumption) – which can represent more than 50 % of the final costs – will be considered.^{41, 42} The PSC components that will be assessed are: substrate, electron transport material, hole transport material, perovskite, back-contact and extra-layers.

Substrate

PSCs substrates can be divided in two categories: rigid - glass materials; and flexible - ultrathin glass, metal, and plastic materials. All these substrates are covered by a thin layer of a metal oxide such as Fluorine-doped Tin Oxide (FTO), Indium Tin Oxide (ITO), and Indium Zin Oxide (IZO); which confers the substrate its high conductivity. Apart from flexibility, these substrates differ in other properties like transmittance and conductivity, which will influence the PSC performance. However, to fabricate a cost-effective PSC, the price of each possible substrate must also be considered, since several studies identified it as one of the most expensive part of the PSC – Figure 7.⁴¹ When considering the transparent substrates, plastic flexible substrates offers a cost-effective solution.

Furthermore, they present a good optical, electrical, mechanical, and chemical properties, thereby making it the most feasible alternative.⁷

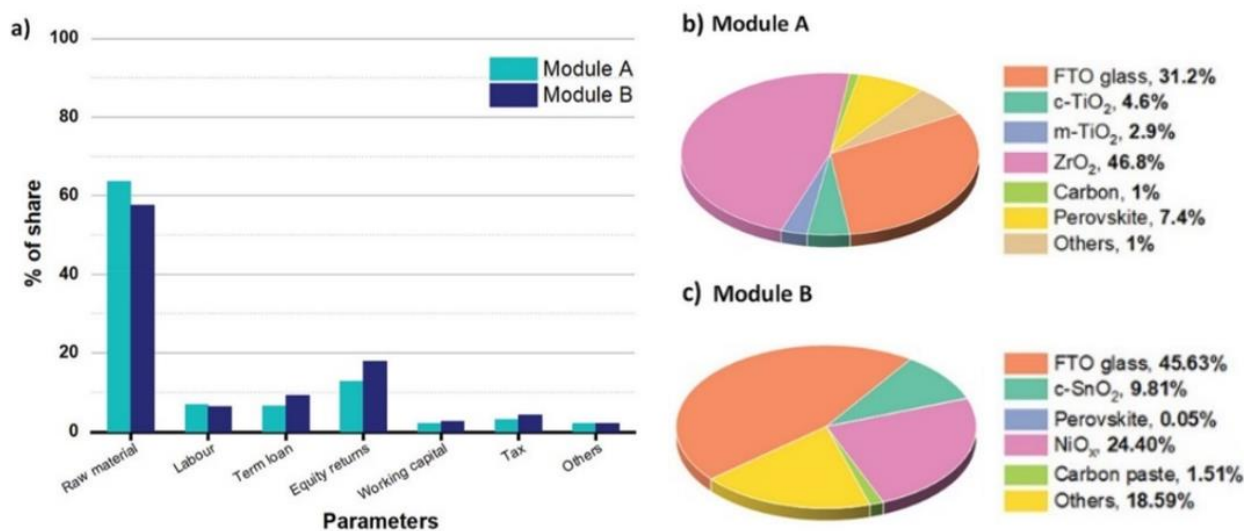


Figure 7 - Charts presenting the cost ratio of each component in a PV installation for 2 hypothetical perovskite modules, and b,c) the respective ratio of the cost per material.

Copyright © 2021 Priyanka Kajal et al. Global Challenges published by Wiley-VCH GmbH

Electron Transport Material

Traditional ETM are mesoporous TiO₂ (n-i-p) and phenyl-C61-butyric acid methyl ester (PCBM) (p-i-n) with PCEs surpassing 23.7 %⁴³ and 24.6 %⁴⁴ respectively. However, since mesoporous TiO₂ needs a sintering step at 450 °C - 500 °C and PCBM is expensive, both become economically problematic. Regarding the n-i-p devices, there are other ETMs that are also high efficient and do not require very high temperature annealing steps, such as: planar TiO₂,⁴⁵ NH₂-TiO₂ nanoparticles (NPs),⁴⁶ SnO₂ (bare⁵ and with an extra layer of Al₂O₃⁴⁷ or ImAChCl⁴⁸), TMAH,⁴⁹ ZnO,⁵⁰ WO₃⁵¹ and 2D SnS₂⁵². Devices have been reported using these materials and exhibiting PCEs higher than 19.9 %, thickness lower than 60 nm, relatively low acquisition cost and maximum sintering temperature of 150 °C – 180 °C. Very recently SnO₂ has emerged as a promising replacement for TiO₂, due to the detrimental photocatalytic effect of TiO₂ under ultraviolet (UV) light. Indeed, the

PSC holding the current PCE record has a ETM of SnO₂.⁵ Some of the most cost-effective ETMs for p-i-n architecture are: buckminsterfullerene (C₆₀),⁵³ NDI-ID⁵⁴ and ITCPTC-Th⁵⁵. Even though C₆₀ is deposited by a high energetic step (thermal evaporation under high vacuum), it is the only ETM raw-material already commercialized among these three.

Hole Transport Material

The most common HTM for n-i-p structure, spiroOMeTAD, is also one of the most expensive ones.⁵³ Other good-performing (PCE > 20 %) but not so expensive HTMs are CuSCN,⁵⁶ CuPc,⁵⁷ PDO₂,⁵⁸ PHPT-py,⁵⁹ DBC-OMeDPA,⁶⁰ OMe-TATPyr,⁶¹ DTP-C6Th⁶² and DTPC13-ThTPA⁶³. None of them need post-treatment, but only CuSCN and CuPc are already commercialized. Regarding the p-i-n architecture, the costly parameter is the temperature needed for the annealing step rather than the acquisition price. Among the best HTMs (PCE > 19 %), the ones with sintering steps at lower temperatures (< 235°C) are 2PACz,⁶⁴ P3CT-Rb,⁶⁵ NiO (doped with Cs⁶⁶ or Sr⁶⁷), PEDOT:PSS,⁶⁸ DFH,⁶⁹ TFB⁷⁰ and MPA-BTTI⁷¹. Also, they don't require a high thickness (thickness ≤ 25 nm), which makes the acquisition cost less significant to the overall cost.

Perovskite layer

Since there are plentiful precursors possible and more than one atom/molecule can be used with the same crystallographic function, there are an infinite number of possible arrangements for fabricating the perovskite layer. Regarding solvents, N,N-dimethylformamide (DMF) and dimethyl sulfoxide (DMSO) are the most used, but many others have already been reported with good performances. Among all PSC layers, this is the most challenging one, given the difficulty to flawlessly crystallize the perovskite precursor solution in large-scale substrates, and to make it environmentally safe and stable for long periods of time. Thus, the selection of

the best perovskite crystal and fabrication conditions should depend more on the stability, upscaling and environmental impact rather than the cost.

Back-contact

The record-breaking n-i-p devices uses the expensive gold as back-contact (BC).⁵ P-i-n devices have a good performance with cheaper metals like silver and copper, but the main drawback of metallic electrodes is the highly energetic deposition method - thermal evaporation under high vacuum. There is still the possibility of using the same material of the front-contact as BC: metal oxide, like ITO⁷² and IZO⁷³. The big advantage is transparency, however part of the PCE is sacrificed due to conductivity restrictions. Carbon-based materials may be the best alternative for a metal-free BC. They have a high chemical stability, conductivity, abundance, non-toxicity and the common carbon pastes made of graphite and carbon black are also relatively cheap.^{74, 75} Nevertheless, the more complex carbon materials as carbon nanotubes³⁹ and graphene⁷⁶ are very expensive.

Extra layers

There are other extra layers that can be used to increase either PCE (by improving the selective charge carriers' extraction or passivating surface defects) or the stability. In some cases, like bathocuproine (BCP) between C60 and copper (Cu),⁷⁷ they are essential for the device's performance, but in the majority of the cases their use is optional. Usually, these layers do not exceed 10 nm and consequently it will not have a significant influence on the final price of the device, as long as it is deposited by a low energy-consuming process. Nonetheless, the more complex the system, the more fabrication issues can arise, and so the number of these extra layers should be minimized.

1.4.2. Stability

Degradation mechanisms

Typically, a PV panel has to keep 80 % of its initial PCE after 25 years of lifetime to be commercialized, i.e. a perovskite solar module starting with a PCE of 20 %, after 25 years should still present a PCE higher than 16 %. This challenging goal only more recently has been pursued by the PSC research community and the number of published works regarding this topic is now increasing exponentially. It is then needed to adequately understand the degradation mechanisms of a PSC device to overcome the stability challenges. Degradation mechanisms can be divided in two categories according to the cause: intrinsic and extrinsic. An intrinsic degradation pathway is related to the cell operation: defects on the perovskite crystal structure, reactivity between adjacent layers, electrical-field, temperature-induced by light; whereas extrinsic is related to the environmental factors such as moisture, oxygen, heat and UV radiation – Figure 8.

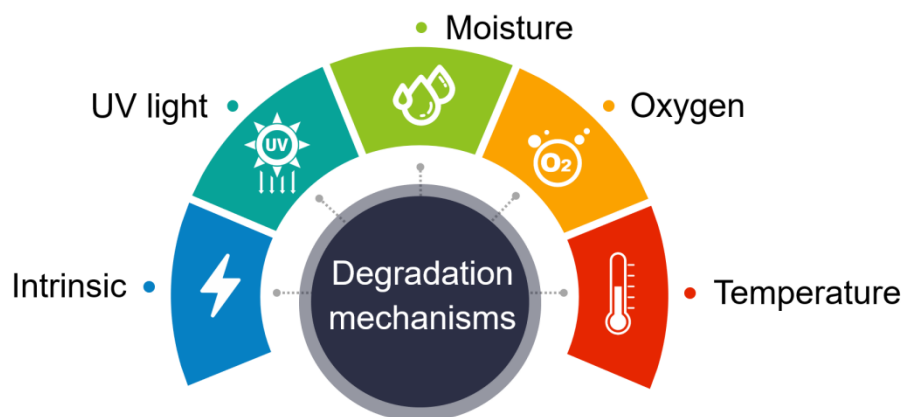


Figure 8 - Five degradation mechanism of PSCs: Intrinsic, UV light, moisture, oxygen and temperature.

Among all these degradation factors, moisture is the most severe because the perovskite has a polar nature and when $\text{CH}_3\text{NH}_3\text{PbI}_3$ is exposed to moisture tends to hydrolyse to PbI_2 , CH_3NH_2 and HI species. This reaction is visible through the change of colour from dark brown to yellow. Another atmospheric hazard is

oxygen since it diffuses into the perovskite layer and traps into the iodine vacancies, leading to the formation of PbI_2 , CH_3NH_2 , I_2 and water upon exposure to light. Thus, usually the perovskite fabrication is done under an inert atmosphere, and the final device is usually encapsulated to protect it from the ambient humidity and oxygen. The commonly employed perovskite is also thermally unstable and decomposes when exposed to temperatures higher than $85\text{ }^\circ\text{C}$ due to structural phase transitions. Apart from perovskite, there are many other selective layers sensitive to these environmental factors, in particular the typical hole transport materials, which should be taken into account when selecting the final design. For instance, UV radiation is harmful to wide band gap ETMs such as TiO_2 and Al_2O_3 , which can be easily suppressed for instance by employing UV cut off filters.⁷⁸

Several good solutions to enhance the PSC stability were already proposed, such as looking for synthesis of perovskite materials without non-reversible degradation pathways, fabrication of pure inorganic PSCs, mix of cations and halides in the perovskite layer configuration, use of additives, passivation materials and encapsulation.⁷⁹ Maximum Power Point Tracking (MPPT) is one of the solidest and most common tests performed for PSC stability assessment and consists in maintaining the PSC under constant 1 sun illumination and under the voltage that produces maximum current. In this way, it is possible to assess how a panel would behave if continuously working under its full power. Moreover, the PCE is not inflated due to the hysteresis effect and its value corresponds to a stabilized and real performance value.^{80, 81} Still, other tests related to the reliability of long-term outdoor must be performed before making any solar module commercial. The complete set of stability tests that a terrestrial PV module must successfully endure are methodically defined in IEC standards, such as 61215 for generic PV modules, 61646 for thin film PV modules, and 63163 - PV modules for consumer electronics.⁸²

Stability enhancing strategies

Up to the writing date (April 2023) the current longest MPPT reported in literature lasted 4390 h (~183 days). The selected device structure was: glass ITO / SnO₂ / (FAPbI₃)_{0.95}(MAPbBr₃)_{0.05} doped with MACl / cross-linking polymer / 4F-PEAI / mix P3HT-spiro-OMeTAD / carbon – Figure 9. Using an inorganic metal oxide as ETM and a carbon-based material for BC are strategic approaches to enhance the long-term stability that also contributes for a low-cost device. Furthermore, the stability was further enhanced by incorporating a cross-linked polymer between the 2D perovskite capping layer and the 3D perovskite bulk, to hinder the ionic diffusion at this interface. As a result, a PSC with 21.2 % PCE retained 90 % of its initial PCE after the 183 days at MPPT.⁸³

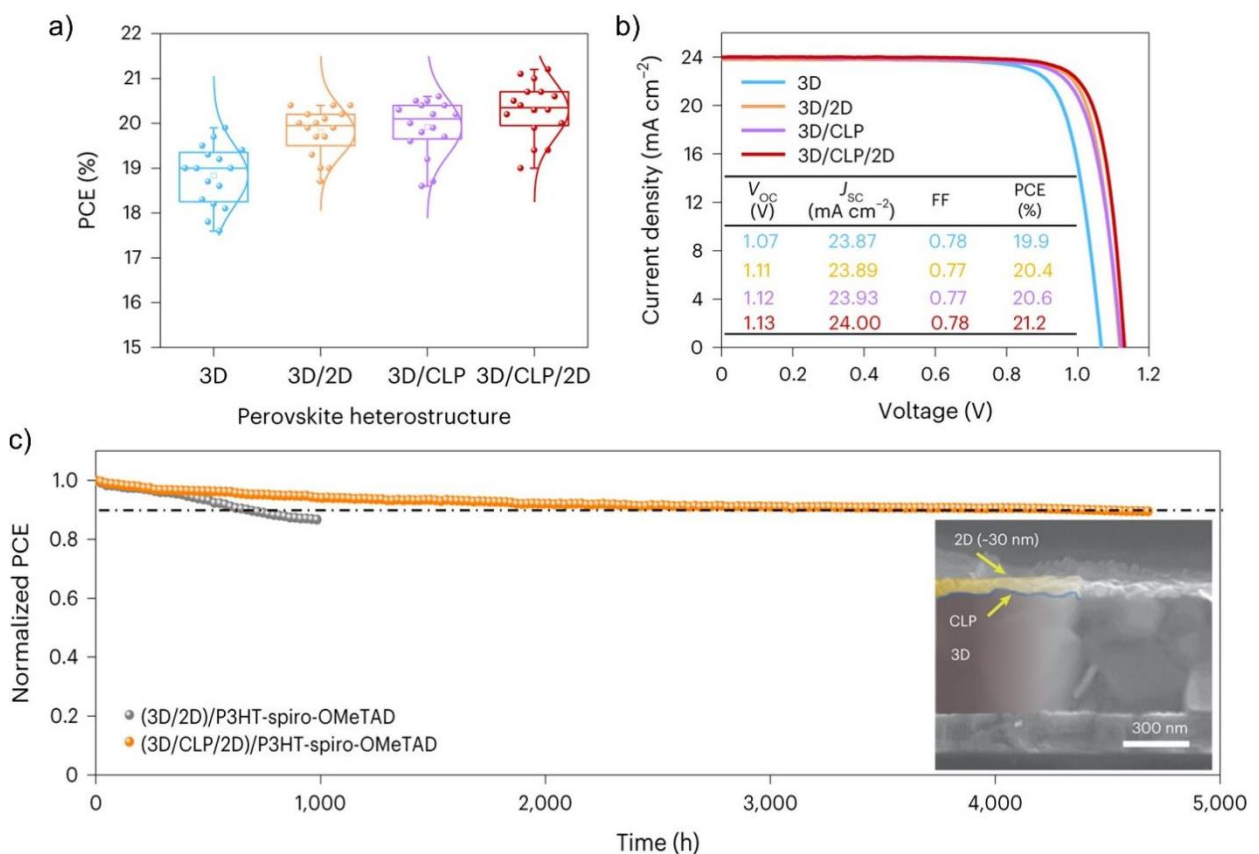


Figure 9 - a) Box plots with the PCE distribution and b) J-V curves of 3D, 3D/2D, 3D/CLP and 3D/CLP/2D perovskite heterostructures. c) MPPT for a 3D/CLP/2D device for almost 5000 h in N₂ and at 60 °C. Inset corresponds to a cross-section SEM image of a 3D/CLP/2D perovskite heterostructures. Copyright © 2023, Luo et al., under exclusive license to Springer Nature Limited.⁸³

In the case of p-i-n architecture, a long-term stability of 3479 h was achieved with the structure: glass ITO / NiO_x / CsFAPbI_{3-x}Cl_x / C60 / BCP / Cu. Once more, the first deposited layer consists of an inorganic metal oxide, which is highly stable due to the strong ionic bonds between the metal cation and oxygen anion (the relatively high annealing temperature required for metal oxides makes it impractical to deposit them onto a perovskite layer). Also, since using a carbon-based BC in p-i-n structures is more complex (due to the energetic mismatch), a buffer layer (BCP) was added to hinder the diffusion of metallic atoms from the Cu BC to the inner layers of the device. Moreover, perovskite was doped with chlorine to suppress the formation of lead iodide and pure CsPbI₃. Impressively, the chlorine doping was responsible for the T80 (time taken for the performance of the solar cell to degrade to 80 % of its initial value) increase from 1128 h to the 3479 h.⁸⁴

Another strategies to increase the PSC long-term operation (longer than 2400 h) include: use of a molten salt in the inorganic perovskite precursor - Cs_{0.1}Pb(I_{1-x}Cl_x)₂ - to stabilize the temperature during its evaporation onto SnO₂ and the perovskite composition in the final film (PCE_{initial} = 24.0 %, PCE_{lost} = 15 %, duration = 3600 h)⁸⁵; adjustment of DMSO content in the perovskite solution and performing the deposition onto a heated SnO₂ substrate (hot-casting method) to enhance the contact at this interface and to suppress the formation of unwanted byproducts (PCE_{initial} = 23.4 %, PCE_{lost} = 25 %, duration = 3000 h)⁸⁶; inhibit lattice distortion of the inorganic perovskite CsPbI₃ by incorporating alkyltrimethoxysilane strain-release layers at the perovskite/TiO₂ interface (PCE_{initial} = 20.1 %, PCE_{lost} = 20 %, duration = 3000 h)⁸⁷; modification of the perovskite bulk with a n-type wide-band gap semiconductor in a p-i-n structure, to suppress nonradiative recombination (PCE_{initial} = 23.5 %, PCE_{lost} = 20 %, duration = 2400 h)⁸⁸. Overall, most of these works reporting highly stable PSCs use a n-i-p configuration, with an inorganic metal oxide planar ETM, and high-quality hybrid perovskites, without methylammonium and with low content of cesium and bromide.

Concerning flexible devices, only MPPT up to 1000 h has been reported. In 2020 Babu et al. published a 15.2 % efficient p-i-n PSC with a carbon BC, that worked 1000 h at MPPT with no loss of performance.⁸⁹ By incorporating an ultra-thin buffer layer composed of a 5 nm thick chromium layer at the ETM/carbon interface, the charge extraction efficacy at that interface was improved, resulting in a record PCE for a p-i-n carbon-based PSC – Figure 10. Both HTM and ETM selected are known to be highly stable (PTAA and PCBM), but the long-term stability was assigned to the carbon BC – if silver is used instead, PCE drops 20 % in only 600 h.⁸⁹ Two years later, the same research institution (SAULE Technologies) reported another 1000 h long MPPT using a p-i-n PSC, with the same HTM, but with a metallic BC and C60/BCP as ETM. This time, Dasgupta et al. added a passivation layer of 4-fluoro-phenethylammonium iodide (4F-PEAI) at the perovskite/HTM interface, which resulted in a better hole extraction and reduced nonradiative recombination loss at that interface. The device with 18.7 % PCE lost less than 10 % of its initial PCE after 1000h at MPPT.⁹⁰

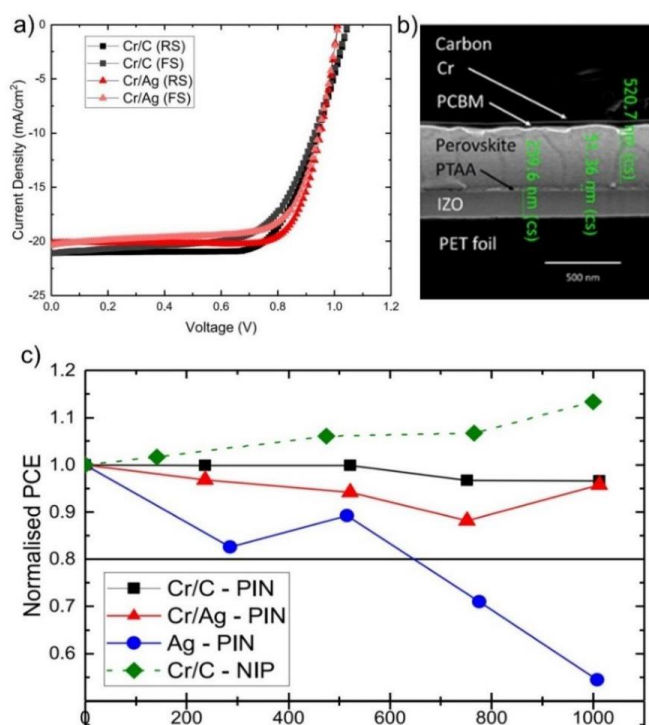


Figure 10 - a) J-V curves for a PSC with carbon and silver BC; b) cross section SEM image of the PSC and c) MPPT results for different PSC configurations: p-i-n with Cr/C, Cr/Ag and Ag BC and n-i-p Cr/C BC. Copyright © 2020 American Chemical Society.⁸⁹

1.4.3. Upscaling

A loss of PCE is inevitable when active areas increase, namely from lab cells ($\sim 0.1 \text{ cm}^2$) to large-area cells ($\sim 1 \text{ cm}^2$) and modules ($> 10 \text{ cm}^2$). There are two main reasons for the PCE drop in larger substrates. First, the decrease in the uniformity and quality of the perovskite absorber layer increases the resistance in the vertical current flow (between electrodes). The current best method to deposit perovskite is spin coating, but the amount of wasted material (ca 90 %) along with the loss of uniformity for substrates larger than $10 \times 10 \text{ cm}^2$ (due to the centrifugal force)⁹¹ keep this deposition method away from industrialization. Second, since the cell is larger, charge carriers will have to go through a longer path in the electrodes (TCO and BC), which increases the horizontal current flow resistance. The front-contact is the most critical because the resistance has to be minimized (by making the TCO layer thicker) without compromising the substrate transparency; otherwise, PCE would also drop due to less photon harvesting. Moreover, for modules it has to be considered also the unavoidable dead areas of bus bars and interconnections. In 2014 Di Carlo *et al.* produced the first solid state modules composed by 5 series-connected individual solar cells based on organometal halide perovskite $\text{MAPbI}_{3-x}\text{Cl}_x$, reporting a PCE of 5.1 % for an active area of 16.8 cm^2 .⁹² Since then, several works were published aiming the PSC upscaling, with topics regarding scalable deposition techniques for the production of uniform and pinhole-free perovskite films, the decrease of the substrate resistance (less studied) and optimization of modules designs.⁹³⁻⁹⁷

Scalable deposition methods

The manufacture of perovskite devices at industrial scale requires also large-scale deposition processes. The main parameters that must be taken in account are: uniformity and quality of the layer produced, amount of wasted material, safety, complexity, energy required for the deposition, cost of equipment and maintenance. Perovskite layer is the most challenging one, due to the complexity

on creating defect-free perovskite crystals.⁹⁸ The most promising high-throughput and large-scale methods for perovskite are: blade coating, slot-die coating, and inkjet printing. Blade coating is a very simple technique in which a blade is used to spread a solution along a substrate, whereas in the slot-die method an ink is supplied to a slit in a fixed head; the ink passes through the slit and it is deposited in a moving substrate, creating a thin film. Blade-coating is the large-scale deposition technique with the highest number of publications, however, in almost all cases it is used in a batch sheet-to-sheet (S2S) model since there is no constant supply of ink. On the other hand, the constant ink supply of the slot-die coating technique makes it more advantageous in an industrialization point of view since it allows the continuous deposition in a roll-to-roll (R2R) process. Inkjet consists on propelling droplets of ink onto a substrate, allows for an arbitrary design deposition at very low material consumption, and can be adapted to work in a continuous R2R process. It is a non-contact, fast, adaptable and very promising technique, which is already used in the industrial pilot line of SAULE Technologies.^{22, 99} Illustrations of these methods are represented in Figure 11, and the most promising works reporting PSC deposited by these deposition methods are presented in Table 1.

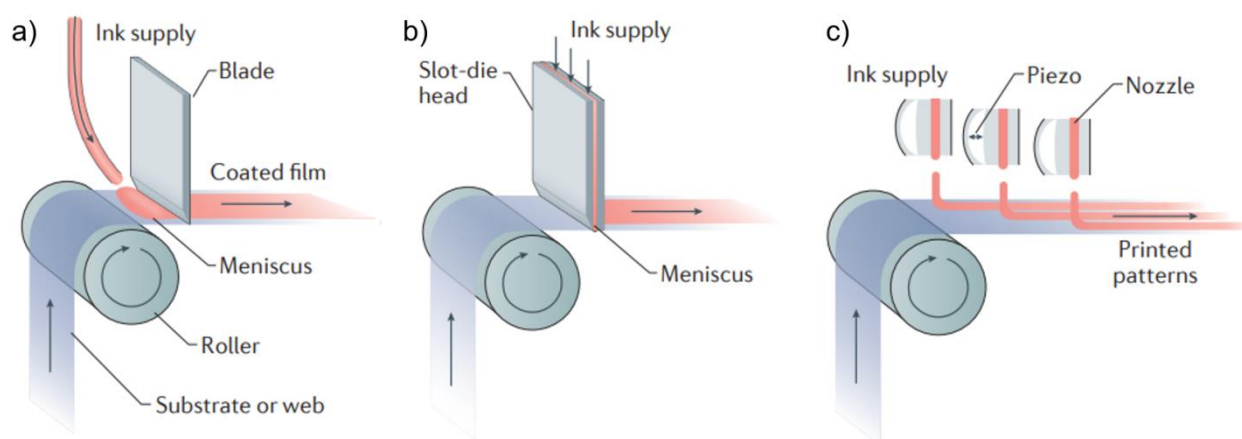


Figure 11 - Illustrations of the most promising perovskite deposition methods: a) blade coating, b) slot-die coating, and c) inkjet printing.¹⁰⁰

Table 1 - List of most promising papers reporting PSC with the perovskite layer deposited by blade coating, slot-die coating and inkjet printing, and respective perovskite composition, atmosphere of deposition, structure of PSC, PCE (lab cell) and year of publication.

Method	Perovskite composition	Atm.	Structure	PCE [%]	Year	Ref
Blade coating	MAPbI ₃	air	?	20.0	2023	101
	?	air	p-i-n	20.7	2023	102
	MAPbI ₃	air	n-i-p	20.3	2023	103
	FA _{0.75} Cs _{0.25} PbI _{2.7} Br _{0.3}	N ₂	?	20.2	2022	104
	MAPbI ₃	N ₂	n-i-p	20.7	2022	105
	FACsPbI ₃ + MACl	air	p-i-n	19.5	2022	106
	MAPbI ₃	N ₂	n-i-p	21.1	2022	107
	FA _{0.92} Cs _{0.08} PbI ₃	air	p-i-n	22.2	2021	108
	FAPbI ₃	N ₂	p-i-n	22.0	2020	109
Slot-die coating	MAPbI ₃	N ₂	n-i-p	21.4	2023	110
	FAPbI ₃	N ₂	p-i-n	22.3	2023	21
	Cs _{0.15} FA _{0.85} Pb(I _{0.83} Br _{0.17}) ₃	N ₂	n-i-p	18.9	2022	111
	FA _{0.91} Cs _{0.09} PbI ₃	N ₂	n-i-p	17.0 (15 on PET)	2022	112
	MAPbI ₃	N ₂	p-i-n	20.8	2021	64
	FA _{0.83} Cs _{0.17} PbI ₃ + PbCl ₂	N ₂	n-i-p	20.4	2021	113
Inkjet	Cs _x FA _{1-x} Pb(I _y Br _{1-y}) ₃	N ₂	n-i-p	18.3	2022	114
	MAPbI ₃	N ₂	p-i-n	16.8 on PET)	2021	115
	Cs _{0.10} FA _{0.75} MA _{0.15} Pb(Br _{0.15} I _{0.85}) ₃	N ₂	p-i-n	21.6	2020	99
	Cs _{0.05} FA _{0.81} MA _{0.14} PbI _{2.55} Br _{0.45}	air	n-i-p	19.6	2020	116

The best performing PSC with a perovskite layer deposited by blade coating was reported by Deng et al. in 2021. The FACsPbI₃ mixed perovskite with slightly excessive AX was dissolved in a mixture of 2-methoxyethanol, acetonitrile and DMSO and deposited at $\sim 6 \text{ m min}^{-1}$, at room temperature and in an ambient atmosphere. The PSC with blade coated PTAA and perovskite, and evaporated C60, BCP and Cu, presented a 22.2 % PCE (8 mm² active area).¹⁰⁸ By using the same active layers (PTAA, BCP, C60, Cu) and same active area, Wu et al. achieved a PCE of 22.0 % by using a doped Cs_{0.05}FA_{0.70}MA_{0.25}PbI₃ perovskite dissolved in DMF and deposited in a pre-heated substrate at 0.45 min^{-1} .¹⁰⁹

Considering slot-die coating technique, a max PCE of 22.3 % was attained by Li et al. by using the same a p-i-n configuration but with spin coated MeO-2PACz as HTM (10.5 mm² active area). Perovskite FAPbI₃ was also dissolved in a mixture of 2-methoxyethanol and acetonitrile, with N-methyl-2-pyrrolidone (NMP) as additive, but was deposited at a slower rate: 0.2 m min^{-1} , and inside a nitrogen glove-box.²¹ High PCEs are also achieved by using the n-i-p configuration: 21.4 % for a PSC with a MAPbI₃ perovskite layer (modified with the artificial peptide sulfonyl- γ -AApeptide) slot-die coated under a humidity up to 40 %.¹¹⁰

The PCEs obtained by inkjet-printed perovskite devices are usually lower since it is more challenging to grow a defect-free perovskite layer using the inkjet printing process. Still, Eggers et al. were able to grow a high-quality micrometer-thick perovskite layer using inkjet method under ambient atmosphere. Cs_{0.10}FA_{0.75}MA_{0.15}Pb(Br_{0.15}I_{0.85})₃ was dissolved in a mixture of γ -butyrolactone (GBL), DMF, and DMSO and printed onto evaporated NiOx. The final p-i-n device with evaporated C60/BCP/Au presented a PCE of 21.6 % (4 mm² active area).⁹⁹

1.4.4. Environmental impact

Any technology before being commercialized must obligatorily be assessed in terms of its potential environmental impact through a life-cycle assessment. This holistic assessment analyses all the energy and material inputs and environmental releases of each step of the technology life, since the raw-materials extraction/synthesis until the technology end-of-life treatment. Usually, cradle-to-grave assessment is divided into five stages: (1) raw material extraction, (2) synthesis of starting products, (3) fabrication, (4) use and (5) decommissioning – Figure 12. In this subchapter, stages (1) and (2) are not analysed, because most of the materials needed for PSC production are already used on an industrial scale for other applications, and thus their environmental impact was already minimized. Regarding stages (3), (4) and (5), a rough outlook is done to perceive which are the most critical environmental aspects of the PSC technology and which solutions were already purposed.¹¹⁷



Figure 12 - Stages of the life-cycle assessment.

Fabrication stage

Fabrication of a perovskite solar device is a complex process. It includes the deposition of several sequential high quality thin films that may require a controlled atmosphere and a pre- and post-treatment steps. Some parameters that may affect the environment, directly or indirectly, are the material waste and energy consumed during the deposition processes (requirement for vacuum, high temperature or controlled atmosphere), the toxicity of the materials and solvents and safety measures to apply during assembling. Starting with the deposition methods, they can be divided in physical and chemical techniques. The physical coatings used in PSCs consist mainly in evaporation and sputtering, where a target is stressed by high temperature or by energetic electrons or ions, respectively, under high or medium vacuum. In spite of producing films with great quality, they are highly energetic and thus increase the environmental impact.

Chemical deposition techniques used in PSC include: spin-coating, dip-coating, screen-printing, slot-die, blade coating, inkjet printing, electrochemical deposition, spray pyrolysis, chemical vapor deposition (CVD), plasma enhanced CVD and atomic layer deposition (ALD). While spin-coating process wastes ~90 % of the precursor material,^{118, 119} spray pyrolysis, CVD, plasma enhanced CVD and ALD are highly energetic due to the amount of gas expended or/and the high temperature required. The remaining 6 methods are certainly less energetic and eco-friendlier. Also, the high annealing temperature required for some inorganic selective layer (TiO_2 , SnO_2 , NiO_x , Al_2O_3) and maintaining a N_2 environment for the deposition of some layer, increases the environmental impact and should both be avoided.¹²⁰

Chemicals toxicity is also a very important aspect for the environmental evaluation. Particularly, lead content in the perovskite absorbing layer is a major concern: inside the human organism, lead ions mimic essential elements such as Ca, Zn, and Fe, which impair the functionality of enzymes and receptors from the liver, kidney and nervous tissue, causing serious damages. Despite the three common intake modes, gastrointestinal, respiratory and dermal uptake, lead from PSCs

leaked and absorbed by the soils can enter plants and consequently the food cycle ten times more efficiently than other lead contaminants resultant from human activities. Furthermore, lead salts are highly soluble in water and thus can be transported by the groundwater causing a serious impact on public health.^{24, 121} However, it represents a colossal challenge to fabricate an efficient and stable PSC without lead. The best candidate to replace lead is tin (Sn), given their similarities. The bandgap of MASnI_3 , FASnI_3 , and CsSnI_3 are 1.20, 1.41, and 1.3 eV, respectively, which is very close to the optimal range (1.3-1.4 eV). These narrow bandgaps result in high current densities similar to Pb-based devices, however, the potential at open-circuit is about 0.5 V, resulting in PCEs lower than 10 %. Furthermore, tin is also considered harmful, is more expensive and exhibits greater terrestrial ecotoxicity than lead.¹²² Stability is also significantly worse. Germanium and bismuth can also replace lead, however its performance is even poorer than Sn-based devices.¹²³ Overall, it has not been yet proposed a successful lead replacer. Nevertheless, the amount of lead in a PSC per area is not that high comparing to other already commercialized technologies, such automotive-type lead-acid batteries: ~60 wt. %.²³

By our rough calculations, it was estimated that a 300 nm thick MAPbI_3 film with one square meter area has ~400 mg of lead. Regarding legislation about this topic, Europe defined in 2011 and consolidated in 2020 that the maximum lead concentration tolerated in electrical and electronic equipment is 0.1 wt. %.¹²⁴ However, this directive also includes about 20 exceptions (directed to applications related to medical devices and monitoring and control instruments) that were exempt from this regulation. Moreover, in Article 2(4.i) it is mentioned that “*This Directive does not apply to: PV panels intended to be used in a system that is designed, assembled and installed by professionals for permanent use at a defined location to produce energy from solar light for public, commercial, industrial and residential applications*”, which includes the perovskite solar devices.¹²⁴ Furthermore, a study published in 2017 estimated the toxicity impacts in humans and in the environment caused by lead iodide present in perovskite-

based tandem solar cells. They also estimated the same impacts but caused by the non-renewables that would otherwise have been used to power the electricity grid. The conclusion was that the environmental burdens caused by the perovskite-based solar cells are still lower than the one caused by using non-renewable energy sources instead. The calculations were based on a lead iodide mass balance, and in case of uncertain data, the maximum amount of lead was considered, so as to obtain the worst-case scenario. Regarding PSCs, it was taken into account the lead emitted to the atmosphere by reaction with polar solvents and leaks to the surroundings of industrial soil during PV panels manufacturing; lead leaked to surface freshwater at the panels dismantling, and lead emitted by its final incineration or washed at the landfill.¹²⁵ So, instead of removing lead, other alternatives are: minimize the lead emissions and waste at its manufacturing; minimize its leakage risk at the panel life by an exceptionally resilient encapsulation; and develop an efficient method to recycled lead and, if possible, reuse TCO substrates. These topics belong to the following stages and will be discussed further ahead.

Other toxic components used in the fabrication stage (but are not in the final device) are certain solvents like DMF, GBL, NMP, hexamethylphosphoramide (HMPA), chlorobenzene and toluene. The perovskite solvents (the first 4) are the most worrying because their high solubility in water enhances the bioavailability and the risk of absorption either by oral ingestion or dermal contact. DMF is particularly toxic: it is readily absorbed either through the skin, inhaled or ingested, is a potent liver toxin and may cause other symptoms such headache, dizziness, nausea and vomiting.¹²⁶ Whenever possible, these solvents must be replaced by greener ones. Anyway, rigorous safety measures have to be imposed, in this stage as well as in the following, to avoid leakages and contaminations either by hazardous solvents or heavy metal compounds in the solid, liquid or vapour form.¹¹⁷

Use stage

Passing to the following stage – use – the main concern is the risk of break (in case of glass substrates) due to certain mechanical stress like hail impact or during an earthquake, and consequent leakage of lead (dissolved in rainwater) for the surrounding environment.¹¹⁷ The lead dissolved in the rainwater is strongly absorbed by the soil and immobilized in the first few centimetres.¹²⁷ However, if this contaminant reaches the water underground, it can be taken to other locations, increasing the hazard for public health. The challenge here is to prevent lead leakage from a broken panel. Jiang et al. proposed the use of a self-healing epoxy resin as thin-film sealant that would resist to mechanical impacts and thus reduce the lead exposure to atmospheric conditions – Figure 13.²⁶ If the thermocrosslinking epoxy resin suffers a cut, it has the capacity to fix the slit in case it is subjected to a temperature higher than its glass transition temperature (~45°C) – a microstructured resin is formed, filling the slit. This heating can easily be provoked by the sunlight rays. Instead of containing the lead inside a broken panel, a lead-absorbing material could be somehow incorporated in the device to further minimize the risk of leakage. Devices with this material coated on both glass covers retained more than 96 % of the lead leaked due to a severe damage.²⁵

Another possible danger is fire. This would cause the emission of pollutants and toxic fumes that would be easily spread and absorbed by the human organism via inhalation, but mitigate or even eliminate this danger is a difficult task. Babayigit et al. exposed tandem Si/perovskite modules to fire (temperature around 760 °C) and concluded that the high temperature caused the formation of PbI_2 . Afterwards, part of it was evaporated and the other part was converted into lead oxides that were totally absorbed by the encapsulation glass. Therefore, the solution proposed was to additivate glass covers to elevate their melting point.¹²⁸

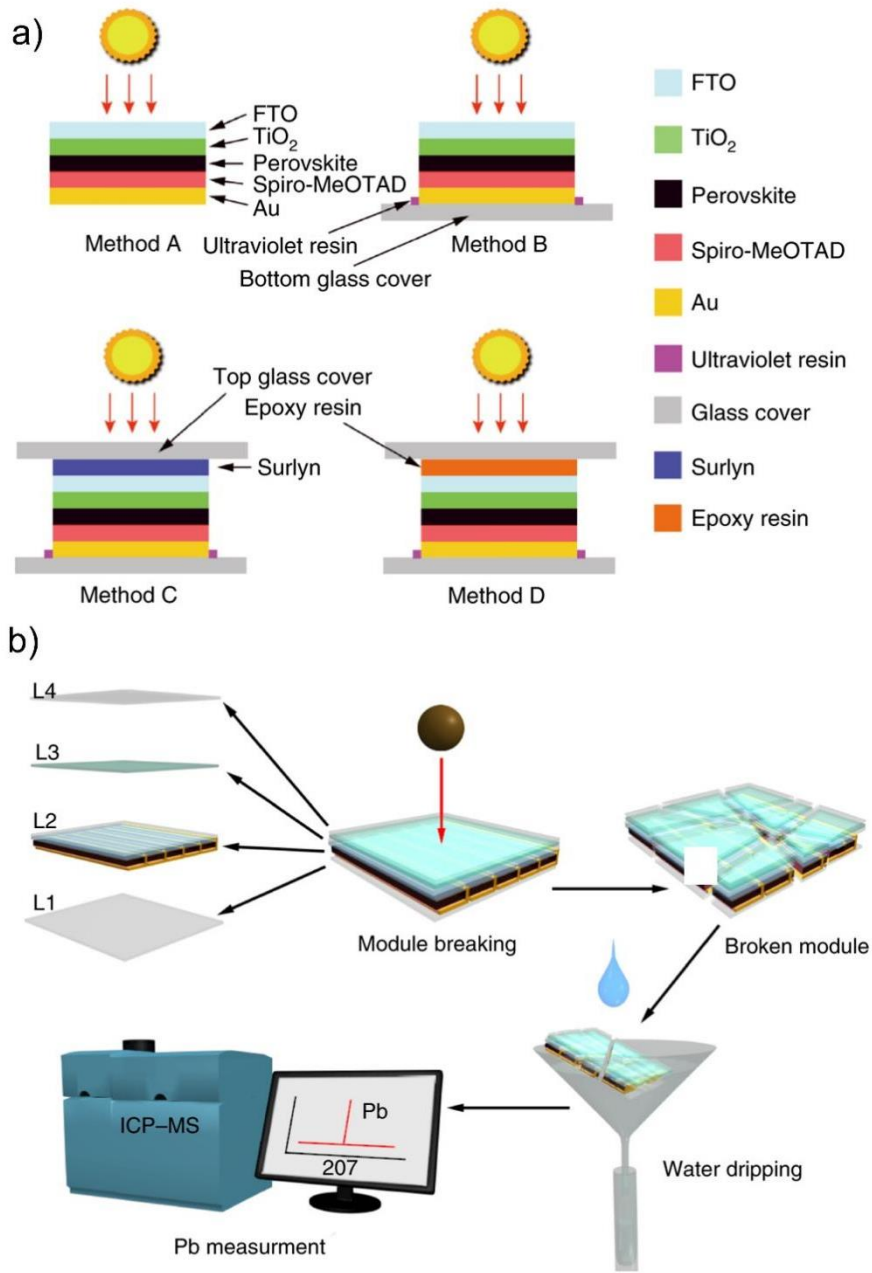


Figure 13 - a) Scheme of the four studied designs and b) scheme of test to assess the Pb leakage after a mechanical impact and rain.²⁶

Decommissioning stage

An ideal decommissioning would involve the safe removal of the panel from its working place, then the lead and the TCO substrates recycling and finally their reuse to manufacture new perovskite solar panels. Other than being a greener option, it is important to recycle lead and TCO because of its high toxicity and price, respectively. Fortunately, there are already procedures for recycling lead and TCO through simple solvent treatments followed by purification. Certainly, these procedures would have to be adapted according to device design and encapsulation method, but still this stage is probably the least environmentally problematic. A very simple method is proposed by Augustine et al.: by submerging a n-i-p conventional device in a potassium hydroxide (KOH) solution, all layers are removed within 5 min. The TCO substrate suffers no damage and can be reused for fabricating new cells.²⁸ The challenge then would be to separate the compounds from the KOH solution for proper neutralization or recovery of valuable or toxic compounds. Alternatively, Binek *et al.* designed a procedure to remove each layer separately, so as to ease the recovery and reuse of each compound.¹²⁹

1.5. Applications

Perovskite Solar Cells, unlike other PV technologies, have a unique combination of properties that make them highly customizable and attractive for different solar energy applications. First, the perovskite composition can be tailored to maximize the absorbance of light according to the intended application. In fact, PSC performed very well at any lighting conditions: from space irradiation to indoor low light. Additionally, the low-temperature requirements for fabricating a PSC enables the use of light-weight and practical flexible substrates; its color and transparency can be tuned by adjusting the perovskite layer composition and the BC material; and the final design and shape can be customized since the PSC can be fabricated entirely with solution processes.¹³⁰

1.5.1. Space applications

Regarding the lighting conditions, PSCs are very attractive for space applications due to their superior resistance to gamma-ray radiation, high power-to-weight ratio (specific power), and also because the most significant causes of degradation – moisture and oxygen present in Earth’s atmosphere – are not present in space. Furthermore, perovskite can also be used in a tandem configuration with another light absorbing semiconductor, or even with another perovskite that has a complementary band-gap. Tandem devices are highly effective at absorbing the full spectrum of incoming light, maximizing the electricity generation capabilities per unit of area. This makes them particularly appealing for powering satellites and other space equipment, where the available area for implementing PV is limited.¹³⁰ In fact, the most common PV used for space applications are powered by III–V multijunction solar cells.

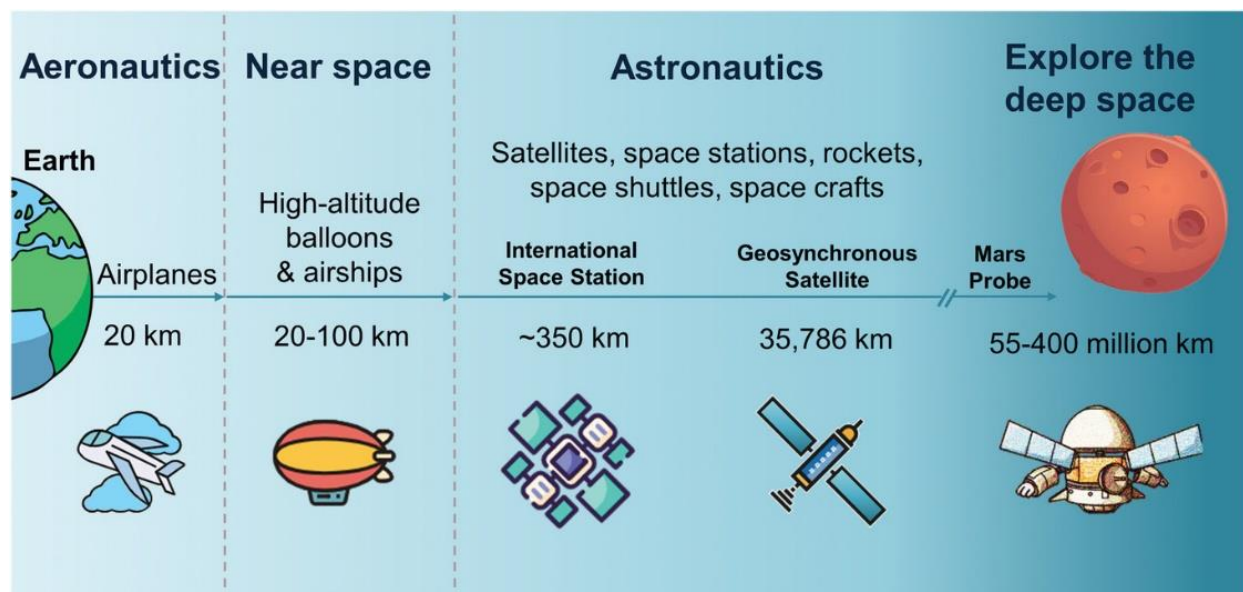


Figure 14 - Different possible applications for PSC in space, according to their distance from earth. © 2021 Wiley-VCH GmbH ¹³¹

1.5.2. Outdoors applications

Since most solar panels are installed on roof tops (urban areas) or solar farms (rural areas) on the Earth's surface, the development of PV technologies is more commonly focused on maximizing the PV performance under 1 sun irradiance. Indeed, PSC PV performance under 1 sun experienced an ultrafast increase in the last years, and in 2023 it reached the PCE of the mature silicon technology – 26.1 %^{5, 18} If considering highly populated urban areas, incorporating solar panels into the buildings' windows, skylights, and exterior walls is a possible way of generating clean energy without consuming much land area. PSCs are particularly attractive for these building-integrated PVs applications due to their color and transparency tunability and ability to be fabricated on lightweight, thin and non-brittle flexible substrates.¹³⁰

1.5.3. Indoor applications

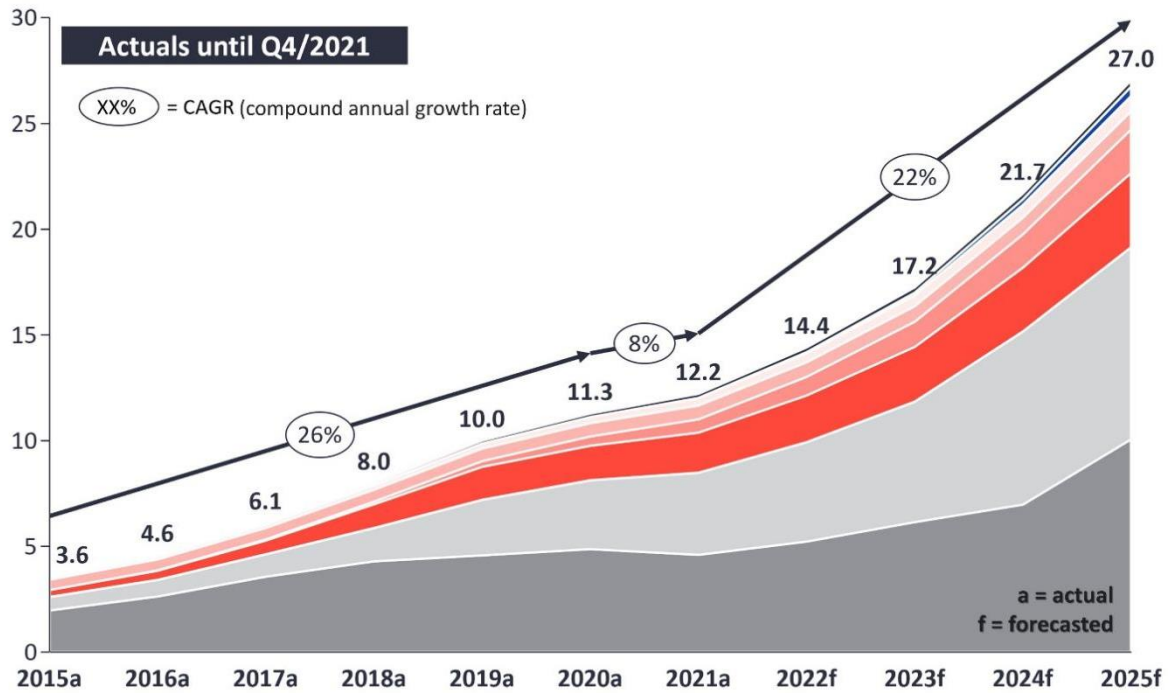
In case of indoor conditions, the most common PV technology is the amorphous silicon, which has been around since late 1970s, and currently holds a maximum PCE of 15.7 % (under 1.1 mW cm⁻² LED light).^{132, 133} However, perovskite technology is also very promising due to the adjustable bandgap (by modification of composition and/or dimensionality), high absorption coefficient, long carrier lifetime, and low recombination rate, which results in a high performance under low-light conditions.⁶

The first publication regarding PSC for indoor environments was presented in 2015 by Chen et al., which obtained an impressive PCE of 27.4 % (83.4 μW cm⁻², 1000 lux, fluorescent).¹³⁴ Since then, many other studies have been published aiming optimizing the low-light performance of PSCs exposed to artificial light sources. Very recently, Xilai et al. achieved a record PCE of 40.1 % (120.9 μW cm⁻², 824 lux, 2700K warm LED), by using a holistic passivation strategy in a micrometer thick perovskite film.¹³⁵ Cheng et al. also reported an

impressive PCE of 36.1 % ($99.7 \mu\text{W cm}^{-2}$, 1000 lux, 2700K fluorescent), by using triple-anion perovskite film.¹³⁶ Regarding flexible PSCs, very recently Chen et al. published a record efficient PSC using the same configuration as the one used in this research article on a PEN substrate: n-i-p architecture with SnO_2 as ETM, spiroOMeTAD as HTM and an evaporated electrode as back-contact. In this work, a full-dimensional stress release of the grain boundaries was accomplished by a 3D crosslinking strategy, which allowed to achieve a PCE of 31.85 %.¹³⁷

Overall, perovskite is a great potential market disruptor for low-light applications since it has twice the PV performance of the well-established technology of amorphous silicon. Besides outperforming efficiency, perovskite devices can also be fabricated using only non-expensive and low-temperature solution processes, like inkjet printing, which gives the possibility of customizing the devices' shape and design at a lower cost. Furthermore, PSCs are a highly suitable option for powering consumer electronics, particularly in Internet of Things (IoT) systems. IoT systems are networks of physical devices and objects that contain sensors, software, and connectivity for exchanging data over the internet. They facilitate communication between various devices, leading to improved automation, control, and decision-making capabilities; and their production is growing exponentially, representing a huge market opportunity for PSCs – by the end of 2020, there was an estimated 11.3 billion IoT connected devices in use around the world, and statistics foresee that this number is expected to grow up to 27.1 billion in 2025 – Figure 15.¹³⁸ An overview of the IoT market segments is presented in Table 2.¹³⁹ A significant portion of these devices are wireless and located indoors, making them the ideal final application for the PSCs developed within this thesis.

Number of global active IoT Connections (installed base) in Bn



CONNECTIVITY TYPE	CAGR 20-21	CAGR 21-25
Wireless Neighborhood Area Networks (WNAN)	17%	11%
5G IoT	-	159%
Other	22%	20%
Wired IoT	4%	7%
LPWA	42%	34%
Legacy Cellular (2G/3G/4G)	16%	17%
Wireless Local Area Networks (WLAN)	19%	24%
Wireless Personal Area Networks (WPAN)	-6%	22%

Figure 15 - Global IoT market forecast [in billion connected IoT devices].¹³⁸

Table 2 - Overview of IoT Market Segments.¹³⁹

location	sector	topic	device	market size [bn \$]	year
indoor	home	home automation	remote controllers	1.42	2020
		security	smart locks	1.64	2021
			(fire) alarm sensors	29.75	2021
			Access control	10.31	2019
		energy efficiency	Temperature/humidity/motion sensors	6.1	2020
	retail	signage	electronic shelf labels	1.8	2020
	office	signage	occupancy sensors/displays	1.9	2021
		peripherals	wireless mouse and keyboards	5.1	2020
mixed used	lifestyle	portable electronic	portable speakers	1.21	2018
			portable ear/headphones	18.2	2021
	health	fitness	smart watches	20.6	2019
		diagnostics	remote patient monitoring	1.9	2021
outdoor	energy	distribution	vibration sensors	3.8	2020
	mobility	asset tracking	GPS tracking	2.2	2021
	cities	traffic optimization	smart parking	6.1	2019
	environment	quality monitoring	gas sensors	2.5	2021
	agriculture	yield monitoring	smart farming sensors	14.4	2021

1.6. Scope of the thesis

PCE of PSCs has already exceeded 26 %, a milestone that typically takes decades to reach, putting PSCs in the forefront PV research priorities. Apart from efficiency, effective progress was made regarding the solar cell's stability, upscaling, and environmental impact, which places this technology in a very high technology readiness level. The work developed in this thesis aims to contribute to the transition of this technology from lab to fab. In order to achieve this goal, a stepwise work plan was meticulously defined, starting from the standard solar cells deposited on glass by a small scale technique (spin coating), high energy-demanding annealing steps and with metallic back-contact, and ending in a low-cost flexible solar cell, deposited by large scale technique (slot-die and blade coating) in ambient atmosphere using only low-energy demanding steps and a carbon-based back-contact. This work will be presented in 5 chapters.

Chapter 1 covers various aspects of the lab to fab transition of PSCs and provides a comprehensive understanding of the current state of PSC commercialization challenges. These include the motivation behind the transition, the working principles and operation of PSCs, promising applications and the latest advancements related to PSC's stability, costs, scalability, and environmental impact. Chapter 2 explores the use of a graphitic-based material - carbon paper - to replace the evaporated gold BC in a standard mesoporous n-i-p PSC fabricated on glass. The performance of three different carbon papers with and without a charge extraction enhancer interlayer was studied, and a maximum PCE of 13.9 % was obtained for the best performing carbon paper, which corresponds to 92 % of the PCE obtained with a gold electrode. This work was developed at LEPABE, in the University of Porto.

In chapter 3, the focus of PSC development was narrowed to indoor applications: maximizing PCE under low-lighting conditions (1000 lux and 200 lux). Also, the substrate was changed for a flexible polymer-based material and the mesoporous ETM layer was removed. Three structures were presented: evaporated gold

electrode, blade coated carbon electrode and HTM, and HTM-free carbon electrode. A maximum PCE under 1000 lux of 30.9 %, 25.4 %, and 23.1 % was obtained, respectively. The opto-electrochemical properties of the perovskite layer and complete solar cell PSC were studied through different methods and stability was assessed. This work was developed at SAULE Technologies (Poland), in collaboration with Fraunhofer ISE (Germany), CHOSE (Italy), and LEPABE (Portugal).

Chapter 4 presents the development of a manufacturing process for PSCs compatible with mass production using the slot-die coating technique. It was designed a 4-layered n-i planar device with metal oxide electron transport material, mixed-halide 3D perovskite, 2D perovskite passivation layer, and carbon-based electrode. The selection of materials and solvent systems was aimed at minimizing the number of fabrication steps, energy consumption, and maximizing device stability without significantly compromising PCE. The optimized manufacturing process produced a PSC with a maximum PCE of 18.6 % under 1000 lx and the 3D perovskite PSC keeps 92 % of its initial efficiency after 550 h under maximum power point tracking. This work was developed at SAULE Technologies (Poland). Finally, general conclusions and possible future work are presented in chapter 5.

References

1. Weber, D., *Z. Naturforsch* **1978**, 33b, 862-865.
2. Weber, D., *Z. Naturforsch* **1978**, 33b, 1443-1445.
3. Kojima, A.; Teshima, K.; Miyasaka, T.; Shirai, Y., Novel photoelectrochemical cell with mesoscopic electrodes sensitized by lead-halide compounds. In *Proceedings of 210th ECS Meeting (ECS, 2006)*, Cancun, Mexico, 2006.
4. Kojima, A.; Teshima, K.; Shirai, Y.; Miyasaka, T., Organometal Halide Perovskites as Visible-Light Sensitizers for Photovoltaic Cells. *Journal of the American Chemical Society* **2009**, 131 (17), 6050-6051.
5. Park, J.; Kim, J.; Yun, H.-S.; Paik, M. J.; Noh, E.; Mun, H. J.; Kim, M. G.; Shin, T. J.; Seok, S. I., Controlled growth of perovskite layers with volatile alkylammonium chlorides. *Nature* **2023**.
6. Wang, K.-L.; Zhou, Y.-H.; Lou, Y.-H.; Wang, Z.-K., Perovskite indoor photovoltaics: opportunity and challenges. *Chemical Science* **2021**, 12 (36), 11936-11954.
7. Liang, X.; Ge, C.; Fang, Q.; Deng, W.; Dey, S.; Lin, H.; Zhang, Y.; Zhang, X.; Zhu, Q.; Hu, H., Flexible Perovskite Solar Cells: Progress and Prospects. *Frontiers in Materials* **2021**, 8.
8. Fraunhofer Institute for Solar Energy Systems, I. *Photovoltaic report*; 2023.
9. Chapin, D. M.; Fuller, C. S.; Pearson, G. L., A New Silicon p-n Junction Photocell for Converting Solar Radiation into Electrical Power. *Journal of Applied Physics* **1954**, 25 (5), 676-677.
10. Swanson, R. M., A vision for crystalline silicon photovoltaics. *Progress in Photovoltaics: Research and Applications* **2006**, 14 (5), 443-453.
11. Garside, M. Silicon - Statistics & Facts. <https://www.statista.com/topics/1959/silicon/>.
12. Saint, C.; Saint, J. L. Fabricating ICs - Making a base wafer. <https://www.britannica.com/technology/integrated-circuit/Fabricating-ICs#ref837156>.
13. Bhandari, K. P.; Collier, J. M.; Ellingson, R. J.; Apul, D. S., Energy payback time (EPBT) and energy return on energy invested (EROI) of solar photovoltaic systems: A systematic review and meta-analysis. *Renewable and Sustainable Energy Reviews* **2015**, 47, 133-141.
14. Qi, L.; Zhang, Y., Effects of solar photovoltaic technology on the environment in China. *Environmental Science and Pollution Research* **2017**, 24 (28), 22133-22142.
15. Hussain, S.; Mehmood, H.; Khizar, M.; Turan, R., Design and analysis of an ultra-thin crystalline silicon heterostructure solar cell featuring SiGe absorber layer. *IET Circuits, Devices & Systems* **2018**, 12 (4), 309-314.
16. Mofteq, M.; Thabit, N., The Impact of employed Solar Systems in Architectural Projects Facades. **2019**, 31.
17. Nayak, P. K.; Mahesh, S.; Snaith, H. J.; Cahen, D., Photovoltaic solar cell technologies: analysing the state of the art. *Nature Reviews Materials* **2019**, 4 (4), 269-285.
18. NREL, N. R. E. L.-. Best Research-cell Efficiencies. 2020.

19. Burgess, D. Thin-film solar cell. <https://www.britannica.com/technology/thin-film-solar-cell>.
20. Ye, H.; Liu, Z.; Liu, X.; Sun, B.; Tan, X.; Tu, Y.; Shi, T.; Tang, Z.; Liao, G., 17.78% efficient low-temperature carbon-based planar perovskite solar cells using Zn-doped SnO₂ electron transport layer. *Applied Surface Science* **2019**, *478*, 417-425.
21. Li, J.; Dagar, J.; Shargaieva, O.; Maus, O.; Remec, M.; Emery, Q.; Khenkin, M.; Ulbrich, C.; Akhundova, F.; Márquez, J. A.; Unold, T.; Fenske, M.; Schultz, C.; Stegemann, B.; Al-Ashouri, A.; Albrecht, S.; Esteves, A. T.; Korte, L.; Köbler, H.; Abate, A.; Többsen, D. M.; Zizak, I.; List-Kratochvil, E. J. W.; Schlatmann, R.; Unger, E., Ink Design Enabling Slot-Die Coated Perovskite Solar Cells with >22% Power Conversion Efficiency, Micro-Modules, and 1 Year of Outdoor Performance Evaluation. *Advanced Energy Materials* **2023**, *n/a* (n/a), 2203898.
22. Technologies, S., The World Premiere of Sun Breaker Installation With Perovskite Solar Modules. 2021.
23. David Linden, T. R., *Handbook of batteries*. 3 ed.; New York : McGraw-Hill: 2002.
24. Li, J.; Cao, H. L.; Jiao, W. B.; Wang, Q.; Wei, M.; Cantone, I.; Lu, J.; Abate, A., Biological impact of lead from halide perovskites reveals the risk of introducing a safe threshold. *Nat Commun* **2020**, *11* (1), 310.
25. Li, X.; Zhang, F.; He, H.; Berry, J. J.; Zhu, K.; Xu, T., On-device lead sequestration for perovskite solar cells. *Nature* **2020**, *578* (7796), 555-558.
26. Jiang, Y.; Qiu, L.; Juarez-Perez, E. J.; Ono, L. K.; Hu, Z.; Liu, Z.; Wu, Z.; Meng, L.; Wang, Q.; Qi, Y., Reduction of lead leakage from damaged lead halide perovskite solar modules using self-healing polymer-based encapsulation. *Nature Energy* **2019**, *4* (7), 585-593.
27. Kadro, J. M.; Hagfeldt, A., The End-of-Life of Perovskite PV. *Joule* **2017**, *1* (1), 29-46.
28. Augustine, B.; Remes, K.; Lorite, G. S.; Varghese, J.; Fabritius, T., Recycling perovskite solar cells through inexpensive quality recovery and reuse of patterned indium tin oxide and substrates from expired devices by single solvent treatment. *Solar Energy Materials and Solar Cells* **2019**, *194*, 74-82.
29. Ossila Perovskites and Perovskite Solar Cells: An Introduction. <https://www.ossila.com/pages/perovskites-and-perovskite-solar-cells-an-introduction>.
30. Green, M. A.; Ho-Baillie, A., Perovskite Solar Cells: The Birth of a New Era in Photovoltaics. *ACS Energy Letters* **2017**, *2* (4), 822-830.
31. Park, N.-G., Perovskite solar cells: an emerging photovoltaic technology. *Materials Today* **2015**, *18* (2), 65-72.
32. Liu, Y.; Yang, Z.; Liu, S., Recent Progress in Single-Crystalline Perovskite Research Including Crystal Preparation, Property Evaluation, and Applications. *Advanced Science* **2018**, *5* (1), 1700471.
33. Rini, M.; Tobey, R. a.; Dean, N.; Itatani, J.; Tomioka, Y.; Tokura, Y.; Schoenlein, R. W.; Cavalleri, A., Control of the electronic phase of a manganite by mode-selective vibrational excitation. *Nature* **2007**, *449*, 72.
34. Edri, E.; Kirmayer, S.; Mukhopadhyay, S.; Gartsman, K.; Hodes, G.; Cahen, D., Elucidating the charge carrier separation and working mechanism of CH₃NH₃PbI₃-xCl_x perovskite solar cells. *Nature Communications* **2014**, *5*, 3461.

35. Mesquita, I.; Andrade, L.; Mendes, A., Perovskite solar cells: Materials, configurations and stability. *Renewable and Sustainable Energy Reviews* **2018**, *82*, 2471-2489.
36. Solar Cells: A Guide to Theory and Measurement. <https://www.ossila.com/pages/solar-cells-theory>.
37. Honsberg, C.; Bowden, S., Solar Cell Operation - IV curve. 2023.
38. Gonzalez-Pedro, V.; Juarez-Perez, E. J.; Arsyad, W.-S.; Barea, E. M.; Fabregat-Santiago, F.; Mora-Sero, I.; Bisquert, J., General Working Principles of CH₃NH₃PbX₃ Perovskite Solar Cells. *Nano Letters* **2014**, *14* (2), 888-893.
39. Wu, X.; Xie, L.; Lin, K.; Lu, J.; Wang, K.; Feng, W.; Fan, B.; Yin, P.; Wei, Z., Efficient and stable carbon-based perovskite solar cells enabled by the inorganic interface of CuSCN and carbon nanotubes. *Journal of Materials Chemistry A* **2019**, *7* (19), 12236-12243.
40. Behrouznejad, F.; Shahbazi, S.; Taghavinia, N.; Wu, H.-P.; Wei-Guang Diao, E., A study on utilizing different metals as the back contact of CH₃NH₃PbI₃ perovskite solar cells. *Journal of Materials Chemistry A* **2016**, *4* (35), 13488-13498.
41. De Bastiani, M.; Larini, V.; Montecucco, R.; Grancini, G., The levelized cost of electricity from perovskite photovoltaics. *Energy & Environmental Science* **2023**, *16* (2), 421-429.
42. Kajal, P.; Verma, B.; Vadaga, S. G. R.; Powar, S., Costing Analysis of Scalable Carbon-Based Perovskite Modules Using Bottom Up Technique. *Global Challenges* **2022**, *6* (2), 2100070.
43. Min, H.; Kim, M.; Lee, S.-U.; Kim, H.; Kim, G.; Choi, K.; Lee, J. H.; Seok, S. I., Efficient, stable solar cells by using inherent bandgap of α -phase formamidinium lead iodide. *Science* **2019**, *366* (6466), 749-753.
44. Li, G.; Su, Z.; Canil, L.; Hughes, D.; Aldamasy, M. H.; Dagar, J.; Trofimov, S.; Wang, L.; Zuo, W.; Jerónimo-Rendon, J. J.; Byranvand, M. M.; Wang, C.; Zhu, R.; Zhang, Z.; Yang, F.; Nasti, G.; Naydenov, B.; Tsoi, W. C.; Li, Z.; Gao, X.; Wang, Z.; Jia, Y.; Unger, E.; Saliba, M.; Li, M.; Abate, A., Highly efficient p-i-n perovskite solar cells that endure temperature variations. *Science* **2023**, *379* (6630), 399-403.
45. Li, Q.; Zhao, Y.; Zhou, W.; Han, Z.; Fu, R.; Lin, F.; Yu, D.; Zhao, Q., Halogen Engineering for Operationally Stable Perovskite Solar Cells via Sequential Deposition. *Advanced Energy Materials* **2019**, *9* (46), 1902239.
46. Hu, W.; Zhou, W.; Lei, X.; Zhou, P.; Zhang, M.; Chen, T.; Zeng, H.; Zhu, J.; Dai, S.; Yang, S.; Yang, S., Low-Temperature In Situ Amino Functionalization of TiO₂ Nanoparticles Sharpens Electron Management Achieving over 21% Efficient Planar Perovskite Solar Cells. *Advanced Materials* **2019**, *31* (8), 1806095.
47. Dagar, J.; Castro-Hermosa, S.; Lucarelli, G.; Zampetti, A.; Cacialli, F.; Brown, T. M., Low-Temperature Solution-Processed Thin SnO₂/Al₂O₃ Double Electron Transport Layers Toward 20% Efficient Perovskite Solar Cells. *IEEE Journal of Photovoltaics* **2019**, *9* (5), 1309-1315.
48. Chen, J.; Zhao, X.; Kim, S.-G.; Park, N.-G., Multifunctional Chemical Linker Imidazoleacetic Acid Hydrochloride for 21% Efficient and Stable Planar Perovskite Solar Cells. *Advanced Materials* **2019**, *31* (39), 1902902.
49. Huang, C.; Lin, P.; Fu, N.; Liu, C.; Xu, B.; Sun, K.; Wang, D.; Zeng, X.; Ke, S., Facile fabrication of highly efficient ETL-free perovskite solar cells with 20%

- efficiency by defect passivation and interface engineering. *Chemical Communications* **2019**, 55 (19), 2777-2780.
50. Dong, X.; Chen, D.; Zhou, J.; Zheng, Y.-Z.; Tao, X., High crystallization of a multiple cation perovskite absorber for low-temperature stable ZnO solar cells with high-efficiency of over 20%. *Nanoscale* **2018**, 10 (15), 7218-7227.
 51. You, Y.; Tian, W.; Min, L.; Cao, F.; Deng, K.; Li, L., TiO₂/WO₃ Bilayer as Electron Transport Layer for Efficient Planar Perovskite Solar Cell with Efficiency Exceeding 20%. *Advanced Materials Interfaces* **2020**, 7 (1), 1901406.
 52. Zhao, X.; Liu, S.; Zhang, H.; Chang, S.-Y.; Huang, W.; Zhu, B.; Shen, Y.; Shen, C.; Wang, D.; Yang, Y.; Wang, M., 20% Efficient Perovskite Solar Cells with 2D Electron Transporting Layer. *Advanced Functional Materials* **2019**, 29 (4), 1805168.
 53. Michael Saliba, J.-P. C.-B., Christian M. Wolff, Martin Stollerfoht, Nga Phung, Steve Albrecht, Dieter Neher, and Antonio Abate, How to Make over 20% Efficient Perovskite Solar Cells in Regular (n-i-p) and Inverted (p-i-n) Architectures. *Chem. Mater.*, **2018**.
 54. Jung, S.-K.; Heo, J. H.; Lee, D. W.; Lee, S.-C.; Lee, S.-H.; Yoon, W.; Yun, H.; Im, S. H.; Kim, J. H.; Kwon, O.-P., Nonfullerene Electron Transporting Material Based on Naphthalene Diimide Small Molecule for Highly Stable Perovskite Solar Cells with Efficiency Exceeding 20%. *Advanced Functional Materials* **2018**, 28 (20), 1800346.
 55. Wu, F.; Gao, W.; Yu, H.; Zhu, L.; Li, L.; Yang, C., Efficient small-molecule non-fullerene electron transporting materials for high-performance inverted perovskite solar cells. *Journal of Materials Chemistry A* **2018**, 6 (10), 4443-4448.
 56. Arora, N.; Dar, M. I.; Hinderhofer, A.; Pellet, N.; Schreiber, F.; Zakeeruddin, S. M.; Grätzel, M., Perovskite solar cells with CuSCN hole extraction layers yield stabilized efficiencies greater than 20%. *Science* **2017**, 358 (6364), 768.
 57. Duong, T.; Peng, J.; Walter, D.; Xiang, J.; Shen, H.; Chugh, D.; Lockrey, M.; Zhong, D.; Li, J.; Weber, K.; White, T. P.; Catchpole, K. R., Perovskite Solar Cells Employing Copper Phthalocyanine Hole-Transport Material with an Efficiency over 20% and Excellent Thermal Stability. *ACS Energy Letters* **2018**, 3 (10), 2441-2448.
 58. Ding, X.; Chen, C.; Sun, L.; Li, H.; Chen, H.; Su, J.; Li, H.; Li, H.; Xu, L.; Cheng, M., Highly efficient phenothiazine 5,5-dioxide-based hole transport materials for planar perovskite solar cells with a PCE exceeding 20%. *Journal of Materials Chemistry A* **2019**, 7 (16), 9510-9516.
 59. Elseman, A. M.; Sharmoukh, W.; Sajid, S.; Cui, P.; Ji, J.; Dou, S.; Wei, D.; Huang, H.; Xi, W.; Chu, L.; Li, Y.; Jiang, B.; Li, M., Superior Stability and Efficiency Over 20% Perovskite Solar Cells Achieved by a Novel Molecularly Engineered Rutin-AgNPs/Thiophene Copolymer. *Advanced Science* **2018**, 5 (11), 1800568.
 60. Ren, M.; Wang, J.; Xie, X.; Zhang, J.; Wang, P., Double-Helicene-Based Hole-Transporter for Perovskite Solar Cells with 22% Efficiency and Operation Durability. *ACS Energy Letters* **2019**, 4 (11), 2683-2688.
 61. Ge, Q.-Q.; Shao, J.-Y.; Ding, J.; Deng, L.-Y.; Zhou, W.-K.; Chen, Y.-X.; Ma, J.-Y.; Wan, L.-J.; Yao, J.; Hu, J.-S.; Zhong, Y.-W., A Two-Dimensional Hole-Transporting Material for High-Performance Perovskite Solar Cells with 20 % Average Efficiency. *Angewandte Chemie International Edition* **2018**, 57 (34), 10959-10965.

62. Yin, X.; Zhou, J.; Song, Z.; Dong, Z.; Bao, Q.; Shrestha, N.; Bista, S. S.; Ellingson, R. J.; Yan, Y.; Tang, W., Dithieno[3,2-b:2',3'-d]pyrrol-Cored Hole Transport Material Enabling Over 21% Efficiency Dopant-Free Perovskite Solar Cells. *Advanced Functional Materials* **2019**, *29* (38), 1904300.
63. Zhou, J.; Yin, X.; Dong, Z.; Ali, A.; Song, Z.; Shrestha, N.; Bista, S. S.; Bao, Q.; Ellingson, R. J.; Yan, Y.; Tang, W., Dithieno[3,2-b:2',3'-d]pyrrole Cored p-Type Semiconductors Enabling 20 % Efficiency Dopant-Free Perovskite Solar Cells. *Angewandte Chemie International Edition* **2019**, *58* (39), 13717-13721.
64. Li, J.; Dagar, J.; Shargaieva, O.; Flatken, M. A.; Köbler, H.; Fenske, M.; Schultz, C.; Stegemann, B.; Just, J.; Többens, D. M.; Abate, A.; Munir, R.; Unger, E., 20.8% Slot-Die Coated MAPbI₃ Perovskite Solar Cells by Optimal DMSO-Content and Age of 2-ME Based Precursor Inks. *Advanced Energy Materials* **2021**, *11* (10), 2003460.
65. Li, S.; He, B.; Xu, J.; Lu, H.; Jiang, J.; Zhu, J.; Kan, Z.; Zhu, L.; Wu, F., Highly efficient inverted perovskite solar cells incorporating P3CT-Rb as a hole transport layer to achieve a large open circuit voltage of 1.144 V. *Nanoscale* **2020**, *12* (6), 3686-3691.
66. Chen, W.; Liu, F.-Z.; Feng, X.-Y.; Djurišić, A. B.; Chan, W. K.; He, Z.-B., Cesium Doped NiOx as an Efficient Hole Extraction Layer for Inverted Planar Perovskite Solar Cells. *Advanced Energy Materials* **2017**, *7* (19), 1700722.
67. Zhang, J.; Mao, W.; Hou, X.; Duan, J.; Zhou, J.; Huang, S.; Ou-Yang, W.; Zhang, X.; Sun, Z.; Chen, X., Solution-processed Sr-doped NiOx as hole transport layer for efficient and stable perovskite solar cells. *Solar Energy* **2018**, *174*, 1133-1141.
68. Yang, D.; Zhang, X.; Wang, K.; Wu, C.; Yang, R.; Hou, Y.; Jiang, Y.; Liu, S.; Priya, S., Stable Efficiency Exceeding 20.6% for Inverted Perovskite Solar Cells through Polymer-Optimized PCBM Electron-Transport Layers. *Nano Letters* **2019**, *19* (5), 3313-3320.
69. Cao, Y.; Li, Y.; Morrissey, T.; Lam, B.; Patrick, B. O.; Dvorak, D. J.; Xia, Z.; Kelly, T. L.; Berlinguette, C. P., Dopant-free molecular hole transport material that mediates a 20% power conversion efficiency in a perovskite solar cell. *Energy & Environmental Science* **2019**, *12* (12), 3502-3507.
70. Yang, D.; Sano, T.; Yaguchi, Y.; Sun, H.; Sasabe, H.; Kido, J., Achieving 20% Efficiency for Low-Temperature-Processed Inverted Perovskite Solar Cells. *Advanced Functional Materials* **2019**, *29* (12), 1807556.
71. Wang, Y.; Chen, W.; Wang, L.; Tu, B.; Chen, T.; Liu, B.; Yang, K.; Koh, C. W.; Zhang, X.; Sun, H.; Chen, G.; Feng, X.; Woo, H. Y.; Djurišić, A. B.; He, Z.; Guo, X., Dopant-Free Small-Molecule Hole-Transporting Material for Inverted Perovskite Solar Cells with Efficiency Exceeding 21%. *Advanced Materials* **2019**, *31* (35), 1902781.
72. Heo, J. H.; Choi, Y. K.; Koh, C. W.; Woo, H. Y.; Im, S. H., Semitransparent FAPbI₃-xBr_x Perovskite Solar Cells Stable under Simultaneous Damp Heat (85 °C/85%) and 1 Sun Light Soaking. *Advanced Materials Technologies* **2019**, *4* (3), 1800390.
73. Prasanna, R.; Leijtens, T.; Dunfield, S. P.; Raiford, J. A.; Wolf, E. J.; Swifter, S. A.; Werner, J.; Eperon, G. E.; de Paula, C.; Palmstrom, A. F.; Boyd, C. C.; van Hest, M. F. A. M.; Bent, S. F.; Teeter, G.; Berry, J. J.; McGehee, M. D., Design of low bandgap tin-lead halide perovskite solar cells to achieve thermal, atmospheric and operational stability. *Nature Energy* **2019**, *4* (11), 939-947.

74. Yu Cai, L. L., Peng Gao, Promise of Commercialization: Carbon Materials for Low-Cost Perovskite Solar Cells. *Chinese Physics B* **2017**.
75. Zhang, H.; Xiao, J.; Shi, J.; Su, H.; Luo, Y.; Li, D.; Wu, H.; Cheng, Y.-B.; Meng, Q., Self-Adhesive Macroporous Carbon Electrodes for Efficient and Stable Perovskite Solar Cells. *Advanced Functional Materials* **2018**, 28 (39), 1802985.
76. Zhang, C.; Wang, S.; Zhang, H.; Feng, Y.; Tian, W.; Yan, Y.; Bian, J.; Wang, Y.; Jin, S.; Zakeeruddin, S. M.; Grätzel, M.; Shi, Y., Efficient stable graphene-based perovskite solar cells with high flexibility in device assembling via modular architecture design. *Energy & Environmental Science* **2019**, 12 (12), 3585-3594.
77. Zheng, X.; Hou, Y.; Bao, C.; Yin, J.; Yuan, F.; Huang, Z.; Song, K.; Liu, J.; Troughton, J.; Gasparini, N.; Zhou, C.; Lin, Y.; Xue, D.-J.; Chen, B.; Johnston, A. K.; Wei, N.; Hedhili, M. N.; Wei, M.; Alsalloum, A. Y.; Maity, P.; Turedi, B.; Yang, C.; Baran, D.; Anthopoulos, T. D.; Han, Y.; Lu, Z.-H.; Mohammed, O. F.; Gao, F.; Sargent, E. H.; Bakr, O. M., Managing grains and interfaces via ligand anchoring enables 22.3%-efficiency inverted perovskite solar cells. *Nature Energy* **2020**, 5 (2), 131-140.
78. Wali, Q.; Iftikhar, F. J.; Khan, M. E.; Ullah, A.; Iqbal, Y.; Jose, R., Advances in stability of perovskite solar cells. *Organic Electronics* **2020**, 78, 105590.
79. He, S.; Qiu, L.; Ono, L. K.; Qi, Y., How far are we from attaining 10-year lifetime for metal halide perovskite solar cells? *Materials Science and Engineering: R: Reports* **2020**, 140, 100545.
80. Saliba, M.; Stolterfoht, M.; Wolff, C. M.; Neher, D.; Abate, A., Measuring Aging Stability of Perovskite Solar Cells. *Joule* **2018**, 2 (6), 1019-1024.
81. Rakocevic, L.; Ernst, F.; Yimga, N. T.; Vashishtha, S.; Aernouts, T.; Heumueller, T.; Brabec, C. J.; Gehlhaar, R.; Poortmans, J., Reliable Performance Comparison of Perovskite Solar Cells Using Optimized Maximum Power Point Tracking. *Solar RRL* **2019**, 3 (2), 1800287.
82. Commission, I. E., IEC 61215-1:2016 - Terrestrial photovoltaic (PV) modules – Design qualification and type approval 2016.
83. Luo, L.; Zeng, H.; Wang, Z.; Li, M.; You, S.; Chen, B.; Maxwell, A.; An, Q.; Cui, L.; Luo, D.; Hu, J.; Li, S.; Cai, X.; Li, W.; Li, L.; Guo, R.; Huang, R.; Liang, W.; Lu, Z.-H.; Mai, L.; Rong, Y.; Sargent, E. H.; Li, X., Stabilization of 3D/2D perovskite heterostructures via inhibition of ion diffusion by cross-linked polymers for solar cells with improved performance. *Nature Energy* **2023**, 8 (3), 294-303.
84. Gostishchev, P.; Saranin, D.; Luchnikov, L.; Muratov, D.; Ishteev, A.; Voronova, M.; Gets, D.; Argunov, E.; Le, T. S.; Didenko, S.; Di Carlo, A., Cl-Anion Engineering for Halide Perovskite Solar Cells and Modules with Enhanced Photostability. *Solar RRL* **2023**, 7 (4), 2200941.
85. Li, H.; Tan, L.; Jiang, C.; Li, M.; Zhou, J.; Ye, Y.; Liu, Y.; Yi, C., Molten Salt Strategy for Reproducible Evaporation of Efficient Perovskite Solar Cells. *Advanced Functional Materials* **2023**, 33 (10), 2211232.
86. Min, H.; Hu, J.; Xu, Z.; Liu, T.; Khan, S.-U.-Z.; Roh, K.; Loo, Y.-L.; Rand, B. P., Hot-Casting-Assisted Liquid Additive Engineering for Efficient and Stable Perovskite Solar Cells. *Advanced Materials* **2022**, 34 (36), 2205309.
87. Liu, T.; Zhao, X.; Zhong, X.; Burlingame, Q. C.; Kahn, A.; Loo, Y.-L., Improved Absorber Phase Stability, Performance, and Lifetime in Inorganic Perovskite Solar

- Cells with Alkyltrimethoxysilane Strain-Release Layers at the Perovskite/TiO₂ Interface. *ACS Energy Letters* **2022**, *7* (10), 3531-3538.
88. Cao, Q.; Li, Y.; Zhang, Y.; Zhao, J.; Wang, T.; Yang, B.; Pu, X.; Yang, J.; Chen, H.; Chen, X.; Li, X.; Ghasemi, S.; Salari, H.; Hagfeldt, A.; Li, X., N-Type Conductive Small Molecule Assisted 23.5% Efficient Inverted Perovskite Solar Cells. *Advanced Energy Materials* **2022**, *12* (34), 2201435.
 89. Babu, V.; Fuentes Pineda, R.; Ahmad, T.; Alvarez, A. O.; Castriotta, L. A.; Di Carlo, A.; Fabregat-Santiago, F.; Wojciechowski, K., Improved Stability of Inverted and Flexible Perovskite Solar Cells with Carbon Electrode. *ACS Applied Energy Materials* **2020**, *3* (6), 5126-5134.
 90. Dasgupta, S.; Żuraw, W.; Ahmad, T.; Castriotta, L. A.; Radicchi, E.; Mróz, W.; Ścigaj, M.; Pawlaczyk, Ł.; Tamulewicz-Szwajkowska, M.; Trzeciński, M.; Serafińczuk, J.; Mosconi, E.; Di Carlo, A.; De Angelis, F.; Dudkowiak, A.; Wojciechowski, K., Modification of a Buried Interface with Bulky Organic Cations for Highly Stable Flexible Perovskite Solar Cells. *ACS Applied Energy Materials* **2022**, *5* (12), 15114-15124.
 91. Razza, S.; Di Giacomo, F.; Matteocci, F.; Cinà, L.; Palma, A. L.; Casaluci, S.; Cameron, P.; D'Epifanio, A.; Licocchia, S.; Reale, A.; Brown, T. M.; Di Carlo, A., Perovskite solar cells and large area modules (100 cm²) based on an air flow-assisted PbI₂ blade coating deposition process. *Journal of Power Sources* **2015**, *277*, 286-291.
 92. Matteocci, F.; Razza, S.; Di Giacomo, F.; Casaluci, S.; Mincuzzi, G.; Brown, T. M.; D'Epifanio, A.; Licocchia, S.; Di Carlo, A., Solid-state solar modules based on mesoscopic organometal halide perovskite: a route towards the up-scaling process. *Physical Chemistry Chemical Physics* **2014**, *16* (9), 3918-3923.
 93. Ye, F.; Chen, H.; Xie, F.; Tang, W.; Yin, M.; He, J.; Bi, E.; Wang, Y.; Yang, X.; Han, L., Soft-cover deposition of scaling-up uniform perovskite thin films for high cost-performance solar cells. *Energy & Environmental Science* **2016**, *9* (7), 2295-2301.
 94. Yang, M.; Li, Z.; Reese, M. O.; Reid, O. G.; Kim, D. H.; Siol, S.; Klein, T. R.; Yan, Y.; Berry, J. J.; van Hest, M. F. A. M.; Zhu, K., Perovskite ink with wide processing window for scalable high-efficiency solar cells. *Nature Energy* **2017**, *2*, 17038.
 95. Tang, S.; Deng, Y.; Zheng, X.; Bai, Y.; Fang, Y.; Dong, Q.; Wei, H.; Huang, J., Composition Engineering in Doctor-Blading of Perovskite Solar Cells. *Advanced Energy Materials* **2017**, *7* (18), 1700302.
 96. Mei, A.; Li, X.; Liu, L.; Ku, Z.; Liu, T.; Rong, Y.; Xu, M.; Hu, M.; Chen, J.; Yang, Y.; Grätzel, M.; Han, H., A hole-conductor-free, fully printable mesoscopic perovskite solar cell with high stability. *Science* **2014**, *345* (6194), 295-298.
 97. Duarte, V. C. M.; Ivanou, D.; Bernardo, G.; Andrade, L.; Mendes, A., Embedded current collectors for efficient large area perovskite solar cells. *International Journal of Energy Research* **2022**, *46* (4), 5288-5295.
 98. Park, N.-G.; Zhu, K., Scalable fabrication and coating methods for perovskite solar cells and solar modules. *Nature Reviews Materials* **2020**, *5* (5), 333-350.
 99. Eggers, H.; Schackmar, F.; Abzieher, T.; Sun, Q.; Lemmer, U.; Vaynzof, Y.; Richards, B. S.; Hernandez-Sosa, G.; Paetzold, U. W., Inkjet-Printed Micrometer-

- Thick Perovskite Solar Cells with Large Columnar Grains. *Advanced Energy Materials* **2020**, 10 (6), 1903184.
100. Li, Z.; Klein, T. R.; Kim, D. H.; Yang, M.; Berry, J. J.; van Hest, M. F. A. M.; Zhu, K., Scalable fabrication of perovskite solar cells. *Nature Reviews Materials* **2018**, 3 (4), 18017.
 101. Baral, P.; Zhang, X.; Garden, K.; Chakraborty, N.; Shen, L.; Cao, Z.; Gong, X.; Whittaker-Brooks, L.; Wang, H., Efficient and stable perovskite solar cells based on blade-coated CH₃NH₃PbI₃ thin films fabricated using “green” solvents under ambient conditions. *Organic Electronics* **2023**, 116, 106763.
 102. Zhang, X.; Baral, P.; Chakraborty, N.; Garden, K.; Shen, L.; Vijayaraghavan, S. N.; Cao, Z.; Yan, F.; Gong, X.; Whittaker-Brooks, L.; Wang, H., Blade Coating Inverted Perovskite Solar Cells with Vacuum-Assisted Nucleation Based on Bottom Quasi-2D Passivation. *Solar RRL* **2023**, 7 (5), 2200900.
 103. Li, H.; Feng, X.; Huang, K.; Lu, S.; Wang, X.; Feng, E.; Chang, J.; Long, C.; Gao, Y.; Chen, Z.; Yi, C.; He, J.; Yang, J., Constructing Additives Synergy Strategy to Doctor-Blade Efficient CH₃NH₃PbI₃ Perovskite Solar Cells under a Wide Range of Humidity from 45% to 82%. *Small* **2023**, n/a (n/a), 2300374.
 104. Zheng, Y.; Xu, X.; Liu, S.; Xu, G.; Bi, Z.; Zhu, Y.; Wang, K.; Liu, S.; Guerrero, A.; Xing, G., Blade Coating High-Quality Formamidinium–Cesium Lead Halide Perovskites with Green Solvent for Efficient and Stable Solar Cells. *Solar RRL* **2022**, 6 (12), 2200737.
 105. Bi, Z.; Xu, X.; Chen, X.; Zhu, Y.; Liu, C.; Yu, H.; Zheng, Y.; Troshin, P. A.; Guerrero, A.; Xu, G., High-performance large-area blade-coated perovskite solar cells with low ohmic loss for low lighting indoor applications. *Chemical Engineering Journal* **2022**, 446, 137164.
 106. Zhang, X.; Shen, L.; Baral, P.; Vijayaraghavan, S. N.; Yan, F.; Gong, X.; Wang, H., Blade-coated inverted perovskite solar cells in an ambient environment. *Solar Energy Materials and Solar Cells* **2022**, 246, 111894.
 107. Lee, K.-M.; Chiu, W.-H.; Tsai, Y.-H.; Wang, C.-S.; Tao, Y.-T.; Lin, Y.-D., High-performance perovskite solar cells based on dopant-free hole-transporting material fabricated by a thermal-assisted blade-coating method with efficiency exceeding 21%. *Chemical Engineering Journal* **2022**, 427, 131609.
 108. Deng, Y.; Xu, S.; Chen, S.; Xiao, X.; Zhao, J.; Huang, J., Defect compensation in formamidinium–caesium perovskites for highly efficient solar mini-modules with improved photostability. *Nature Energy* **2021**, 6 (6), 633-641.
 109. Wu, W.-Q.; Rudd, P. N.; Wang, Q.; Yang, Z.; Huang, J., Blading Phase-Pure Formamidinium-Alloyed Perovskites for High-Efficiency Solar Cells with Low Photovoltage Deficit and Improved Stability. *Advanced Materials* **2020**, 32 (28), 2000995.
 110. Abate, S. Y.; Yang, Z.; Jha, S.; Ma, G.; Ouyang, Z.; Zhang, H.; Muhammad, S.; Pradhan, N.; Gu, X.; Patton, D.; Wang, K.; Li, D.; Cai, J.; Dai, Q., Room temperature slot-die coated perovskite layer modified with sulfonyl- γ -AApeptide for high performance perovskite solar devices. *Chemical Engineering Journal* **2023**, 457, 141199.
 111. Rana, P. J. S.; Febriansyah, B.; Koh, T. M.; Muhammad, B. T.; Salim, T.; Hooper, T. J. N.; Kanwat, A.; Ghosh, B.; Kajal, P.; Lew, J. H.; Aw, Y. C.; Yantara, N.; Bruno, A.; Pullarkat, S. A.; Ager, J. W.; Leong, W. L.; Mhaisalkar, S. G.; Mathews,

- N., Alkali Additives Enable Efficient Large Area (>55 cm²) Slot-Die Coated Perovskite Solar Modules. *Advanced Functional Materials* **2022**, 32 (22), 2113026.
112. Benitez-Rodriguez, J. F.; Chen, D.; Scully, A. D.; Easton, C. D.; Vak, D.; Li, H.; Shaw, P. E.; Burn, P. L.; Caruso, R. A.; Gao, M., Slot-die coating of a formamidinium-cesium mixed-cation perovskite for roll-to-roll fabrication of perovskite solar cells under ambient laboratory conditions. *Solar Energy Materials and Solar Cells* **2022**, 246, 111884.
113. Bu, T.; Li, J.; Li, H.; Tian, C.; Su, J.; Tong, G.; Ono, L. K.; Wang, C.; Lin, Z.; Chai, N.; Zhang, X.-L.; Chang, J.; Lu, J.; Zhong, J.; Huang, W.; Qi, Y.; Cheng, Y.-B.; Huang, F., Lead halide-templated crystallization of methylamine-free perovskite for efficient photovoltaic modules. *Science* **2021**, 372 (6548), 1327-1332.
114. Yang, H.; Wang, J.; Yu, X.; Feng, Y.; Chen, X.; Long, F.; Ku, Z.; Huang, F.; Cheng, Y.; Peng, Y., Solvent engineering in inkjet-printed perovskite solar cells. *Chemical Physics Letters* **2022**, 807, 140084.
115. Gao, B.; Meng, J., Flexible CH₃NH₃PbI₃ perovskite solar cells with high stability based on all inkjet printing. *Solar Energy* **2021**, 230, 598-604.
116. Li, Z.; Li, P.; Chen, G.; Cheng, Y.; Pi, X.; Yu, X.; Yang, D.; Han, L.; Zhang, Y.; Song, Y., Ink Engineering of Inkjet Printing Perovskite. *ACS Applied Materials & Interfaces* **2020**, 12 (35), 39082-39091.
117. Babayigit, A.; Ethirajan, A.; Muller, M.; Conings, B., Toxicity of organometal halide perovskite solar cells. *Nature Materials* **2016**, 15 (3), 247-251.
118. Remeika, M.; Qi, Y., Scalable solution coating of the absorber for perovskite solar cells. *Journal of Energy Chemistry* **2018**, 27 (4), 1101-1110.
119. Huang, F.; Li, M.; Siffalovic, P.; Cao, G.; Tian, J., From scalable solution fabrication of perovskite films towards commercialization of solar cells. *Energy & Environmental Science* **2019**, 12 (2), 518-549.
120. Carneiro, A. L.; Martins, A. A.; Duarte, V. C. M.; Mata, T. M.; Andrade, L., Energy consumption and carbon footprint of perovskite solar cells. *Energy Reports* **2022**, 8, 475-481.
121. Laurence L. Brunton, R. H.-D., Björn C. Knollmann, *Goodman & Gilman's: The Pharmacological Basis of Therapeutics*. 13th ed.; McGraw-Hill Education: 2017.
122. Van der Voet, E. S., R.; Eckelman, M.; Mudd, G.; Norgate, T.; Hirschier, R. *Environmental Risks and Challenges and Anthropogenic Metals Flows and Cycles*; UNEP: 2013.
123. Ke, W.; Kanatzidis, M. G., Prospects for low-toxicity lead-free perovskite solar cells. *Nature Communications* **2019**, 10 (1), 965.
124. Directive 2011/65/EU of the European Parliament and of the Council of 8 June 2011 on the restriction of the use of certain hazardous substances in electrical and electronic equipment Union, T. E. P. a. t. C. o. t. E., Ed. 2011.
125. Hauck, M.; Lighthart, T.; Schaap, M.; Boukris, E.; Brouwer, D., Environmental benefits of reduced electricity use exceed impacts from lead use for perovskite based tandem solar cell. *Renewable Energy* **2017**, 111, 906-913.
126. National Institute for Occupational Safety and Health, Preventing Adverse Health Effects from Exposure to: Dimethylformamide (DMF). *Centers for Disease Control and Prevention* **2014**.
127. Hailegnaw, B.; Kirmayer, S.; Edri, E.; Hodes, G.; Cahen, D., Rain on Methylammonium Lead Iodide Based Perovskites: Possible Environmental Effects

- of Perovskite Solar Cells. *The Journal of Physical Chemistry Letters* **2015**, 6 (9), 1543-1547.
128. Conings, B.; Babayigit, A.; Boyen, H.-G., Fire Safety of Lead Halide Perovskite Photovoltaics. *ACS Energy Letters* **2019**, 4 (4), 873-878.
129. Binek, A.; Petrus, M. L.; Huber, N.; Bristow, H.; Hu, Y.; Bein, T.; Docampo, P., Recycling Perovskite Solar Cells To Avoid Lead Waste. *ACS Applied Materials & Interfaces* **2016**, 8 (20), 12881-12886.
130. Bati, A. S. R.; Zhong, Y. L.; Burn, P. L.; Nazeeruddin, M. K.; Shaw, P. E.; Batmunkh, M., Next-generation applications for integrated perovskite solar cells. *Communications Materials* **2023**, 4 (1), 2.
131. Tu, Y.; Wu, J.; Xu, G.; Yang, X.; Cai, R.; Gong, Q.; Zhu, R.; Huang, W., Perovskite Solar Cells for Space Applications: Progress and Challenges. *Advanced Materials* **2021**, 33 (21), 2006545.
132. Hin Lee, H. K.; Barbé, J.; Tsoi, W. C., Chapter Ten - Organic and perovskite photovoltaics for indoor applications. In *Solar Cells and Light Management*, Enrichi, F.; Righini, G. C., Eds. Elsevier: 2020; pp 355-388.
133. Yang, P. C.; Chan, I. M.; Lin, C. H.; Chang, Y. L. In *Thin film solar cells for indoor use*, 2011 37th IEEE Photovoltaic Specialists Conference, 19-24 June 2011; 2011; pp 000696-000698.
134. Chen, C.-Y.; Chang, J.-H.; Chiang, K.-M.; Lin, H.-L.; Hsiao, S.-Y.; Lin, H.-W., Perovskite Photovoltaics for Dim-Light Applications. *Advanced Functional Materials* **2015**, 25 (45), 7064-7070.
135. He, X.; Chen, J.; Ren, X.; Zhang, L.; Liu, Y.; Feng, J.; Fang, J.; Zhao, K.; Liu, S., 40.1% Record Low-Light Solar-Cell Efficiency by Holistic Trap-Passivation using Micrometer-Thick Perovskite Film. *Advanced Materials* **2021**, 33 (27), 2100770.
136. Cheng, R.; Chung, C.-C.; Zhang, H.; Liu, F.; Wang, W.-T.; Zhou, Z.; Wang, S.; Djurišić, A. B.; Feng, S.-P., Tailoring Triple-Anion Perovskite Material for Indoor Light Harvesting with Restrained Halide Segregation and Record High Efficiency Beyond 36%. *Advanced Energy Materials* **2019**, 9 (38), 1901980.
137. Chen, C.-H.; Su, Z.-H.; Lou, Y.-H.; Yu, Y.-J.; Wang, K.-L.; Liu, G.-L.; Shi, Y.-R.; Chen, J.; Cao, J.-J.; Zhang, L.; Gao, X.-Y.; Wang, Z.-K., Full-Dimensional Grain Boundary Stress Release for Flexible Perovskite Indoor Photovoltaics. *Advanced Materials* **2022**, 34 (16), 2200320.
138. Hasan, M. State of IoT 2022: Number of connected IoT devices growing 18% to 14.4 billion globally *IoT Analytics* [Online], 2022. <https://iot-analytics.com/number-connected-iot-devices/>.
139. Wojciechowski, K.; Forgács, D., Commercial Applications of Indoor Photovoltaics Based on Flexible Perovskite Solar Cells. *ACS Energy Letters* **2022**, 7 (10), 3729-3733.

CHAPTER 2

CARBON-BASED ELECTRODE FOR RIGID PEROVSKITE SOLAR CELLS

Adapted from the peer-reviewed short-communication and article:

Novel carbon-based material for perovskite solar cells back-contact

Cristina Teixeira, Luísa Andrade, Adélio Mendes; International Journal of Energy Research **43** (2019) p:7541-7546

Easy processing carbon paper electrode for highly efficient perovskite solar cells

Cristina Teixeira, Luísa Andrade, Adélio Mendes; Journal of Power Sources **479** (2020) p:229071

CARBON-BASED ELECTRODE FOR RIGID PEROVSKITE SOLAR CELLS

2.1. Introduction

The standard most mature architecture for a perovskite solar cell (PSC) consists in a mesoporous n-i-p configuration, with spiroOMeTAD as hole transport material (HTM), an evaporated gold electrode, and a glass substrate. Since there is a solid know-how about this structure, it is a good starting point for the development of a fabrication protocol compatible with large-scale production. The procedure to fabricate mesoporous n-i-p PSCs was already optimized in the host laboratory based on commercial materials, and a maximum power conversion efficiency of 18 % was obtained. Still, the list of industrial incompatibilities that need to be solved was long, therefore each layer was assessed separately for a more effective optimization. In a quick overview, the evaporated gold electrode is easily identified as one of the most critical issues, not only because of the high costs, but also due to its low energy for ion migration into the perovskite inner layers and high energy-demanding deposition.¹ Graphitic-based materials have been proposed as back contact (BC) since they have a high electronic conductivity, high oxidation stability, tunable work function and low cost.²

There are fundamentally two types of n-i-p carbon-based PSCs, conventional and mesoscopic architectures. In the mesoscopic architecture, devices are fabricated by infiltrating the perovskite precursor through a 3-layered porous stack of an

electron transport material (ETM), an insulating material and a graphitic-based material. In the conventional architecture each layer is deposited sequentially: blocking layer, scaffold, perovskite layer, HTM and BC. Mesoscopic architecture is less efficient than the conventional due to the difficulty in obtaining a high quality perovskite through infiltration.³ The first conventional architecture with a carbon-based BC was published in 2014 by Licheng Sun' group and had a power conversion efficiency (PCE) of 6.64 %.⁴ In 2019, Qian-Qian et al.⁵ achieved a PCE of 18.1 % by applying graphene as interfacial electrical charge enhancer between P3HT HTM and the carbon paste BC layer.⁵ The same PCE of 18.1 % was achieved by Grätzel's group, with a graphitic carbon paste electrode applied over a HTM of CuSCN.⁶ Presently, the maximum PCE of a carbon-based PSC is 19.2 %.⁷ In this study, Zhang et al. used a solvent exchange method to provide adhesive properties to the macroporous carbon material in order to improve the contact at the carbon/spiroOMeTAD HTM interface. As shown, the PCE improvement in the n-i-p conventional PSCs using graphitic-based BC consists basically in the enhancement of the electrical and physical contact between the carbon electrode and the underlying HTM layer.⁸

Usually, low-cost carbon BCs are obtained by blade-coating or screen-printing a commercial carbon paste. Other carbon materials like carbon-nanotubes and graphene can also be used, but they are less common due to high cost, complexity of deposition, and lower efficiency at extracting the photogenerated charge carriers at the BC.³ For instance, PCEs of 17.6 %⁹, 17.6 %¹⁰ and 12.4 %¹¹ were obtained by using a BC based on multiwalled carbon nanotubes, single-walled carbon nanotubes and double-layer graphene, respectively. In a previous work,¹² C. Teixeira reported the use of a novel carbon material for a BC - carbon paper, that consists in a structure of intertwined graphite fibers (diameter of $\sim 7\mu\text{m}$) coated with a $\sim 40\mu\text{m}$ thick microporous layer made of graphite and carbon black. The network of carbon fibers serves as a highway for electrical charge extraction, while the microporous layer ensures a better interfacial contact with the HTM. To the best of our knowledge, this material was never used before as BC in PSCs. The

closest material used for this purpose was reported by Gholipour et al. and consisted of a carbon cloth embedded in a carbon paste. Despite the moderate PCE of 14.2 %, this BC was fabricated through a complex process that included a higher temperature step and a final drop cast of spiroOMeTAD. Carbon paper application method is much simpler - it is used as received and just laminated above the HTM - which makes it appealing for industrialization.¹³

In this chapter, three different carbon papers were selected and their performance as BC in mesoporous n-i-p PSCs made on a glass substrate was studied. The selected carbon papers were: a non-PTFE treated carbon paper - CP1, a highly flexible and thin carbon paper - CP2, and the previously used carbon paper - CP3. With no other additional layer, a maximum PCE (relative PCE) of 12.93 % (89 %), 11.96 % (85 %) and 7.76 % (54 %) is obtained for CP1, CP2 and CP3, respectively. Relative PCE stands for the ratio between the PCE obtained with the gold electrode and the PCE obtained with the carbon paper in the same cell (the gold layer is removed after the measurement, the carbon papers are assembled and the photovoltaic performance of the cell is measured again). To further decrease the interfacial resistance between the CP and the HTM, an ultra-thin gold layer (5 nm) was added at this interface, resulting in a PCE (relative PCE) increase for 13.87 % (92 %), 13.00 % (90 %), and 11.70 % (81 %), for CP1, CP2 and CP3, for respectively.

2.2. Experimental Section

2.2.1. Materials and rigid PSC fabrication

A fluorine-doped tin-oxide conductive glass (from Solaronix) was used as glass substrate for PSC devices - Figure 2. Several glass pieces with dimensions of 9.6×4.8 cm² were cut – Figure 1a) - and a laser scribing – Figure 1b) - was made to electrically separate the photoelectrode and the counter-electrode sides. The

glass pieces were cleaned according to a standard procedure that includes several steps. First, they were washed with a Hellmanex solution and then with water. After drying with compressed air, the glasses were submerged subsequently in a KOH (Sigma-Aldrich, $\geq 85\%$) and ethanol solutions (Valente e Ribeiro, Lda) and subjected to ultra-sounds for 5 minutes - Figure 1c). Next, they were washed with deionized water, dried with compressed air and subjected again to ultra-sounds for 5 more minutes. After drying with compressed air, the transparent conductive oxide (TCO) side of the substrate was exposed to ultraviolet light for 20 min – Figure 1d).

The first layer being deposited in preparing the complete devices is the blocking layer, made of compact TiO_2 - Figure 2. For that, a solution of 7 mL of anhydrous isopropanol 99.8 % (Sigma-Aldrich, 99.7 %) with 0.4 mL of acetylacetone $< 99.5\%$ (Sigma-Aldrich) and 0.6 mL of titanium diisopropoxide bis(acetylacetonate) 75 %wt (Sigma-Aldrich) was prepared inside a glove box (GB) - Figure 1e). This solution was then brought out of the GB and sprayed - Figure 1h) - uniformly throughout the surface of the substrates placed on a heating plate at $450\text{ }^\circ\text{C}$ - Figure 1i). After 45 min, the set point of the heating plate was changed to $25\text{ }^\circ\text{C}$. This technique is called spray pyrolysis. The glass pieces were then cut into single cells of $1.2 \times 2.4\text{ cm}^2$ and placed again inside the GB for the deposition of the other active layers.

For the mesoporous layer deposition - Figure 2, scotch tape was glued onto the counter-electrode side, working as a mask to prevent short circuits in the final device. 1 g of TiO_2 paste (DSL 30NR-D from DyeSol) was dissolved in 6 g of ethanol; 50 μL of this solution were spin-coated on each device - Figure 1f). After the deposition, the cells were placed on a heating plate at $100\text{ }^\circ\text{C}$ for 1 min and then sintered at $500\text{ }^\circ\text{C}$ for 2 h in an oven - Figure 1g).

After allowing the mesoporous layer to cool down to room temperature, follows the perovskite deposition inside the GB - Figure 2. The components chosen for the perovskite's monovalent cations were a mixture of FA, MA and inorganic Cs, because the resulting triple cation perovskite composition is thermally more stable,

contains less phase impurities and is less sensitive to processing conditions.¹⁴ For the inorganic cation and halogen, lead and a mixture of iodine and bromine were used, respectively. Thus, the triple cation perovskite solution ($\text{CsI}_{0.05}(\text{FAPbI}_3)_{0.83}(\text{MAPbBr}_3)_{0.17}$)_{0.95} is prepared as follows: 0.50711 g of PbI_2 (1.1 M) (Sigma-Aldrich, 99 %), 0.073402 g of PbBr_2 (0.2 M) (Sigma-Aldrich, 99.99 %), 0.022394 g of MABr (0.2 M) (Greatcell solar) and 0.17197 g of FAI (1 M) (Greatcell solar) were first weighed and mixed. Then 0.8 mL of DMF (dimethylformamide) (Sigma-Aldrich, 99.8 %) and 0.2 mL of DMSO (dimethyl sulfoxide) (Sigma-Aldrich) were added. Finally, 0.95 mL of this stock solution were added to 0.05 mL of a cesium iodide solution (Sigma-Aldrich); 50 μL of this solution were spin-coated on top of the TiO_2 mesoporous layer. The method selected for the perovskite deposition was the one-step deposition via anti-solvent and thereby 100 μL of chlorobenzene (Sigma-Aldrich, 99.8 %) were dripped onto the cell during the spinning. Its function was to delay the perovskite crystallization and enable the formation of a dense and more uniform surface. The cells were then placed on a heating plate at 100 °C for 40 min and left to cool down to room temperature.

Follows the deposition of the HTM layer, which was spiroOMeTAD - Figure 2. First, 0.102 g of this compound (Chemborun, 99.57 %) was weighted and dissolved in a solution made of 1116 μL of chlorobenzene, 40 μL of 4-tert-butylpyridine (TBP) (Sigma-Aldrich), 23 μL of lithium bis(trifluoromethanesulfonyl)imide (LiTFSi) (Sigma-Aldrich) and 10 μL of cobalt (III) TFSI salt from Greatcell solar (FK209). Then, 50 μL of this stock solution was spin-coated on each cell, inside the GB, and left to dry at ambient temperature. The last step of the PSC assembly was the deposition of 60 nm of gold - Figure 2 - by a thermal evaporation process under high vacuum (3 nbar), at a rate of 0.4-1.25 \AA s^{-1} - Figure 1j).

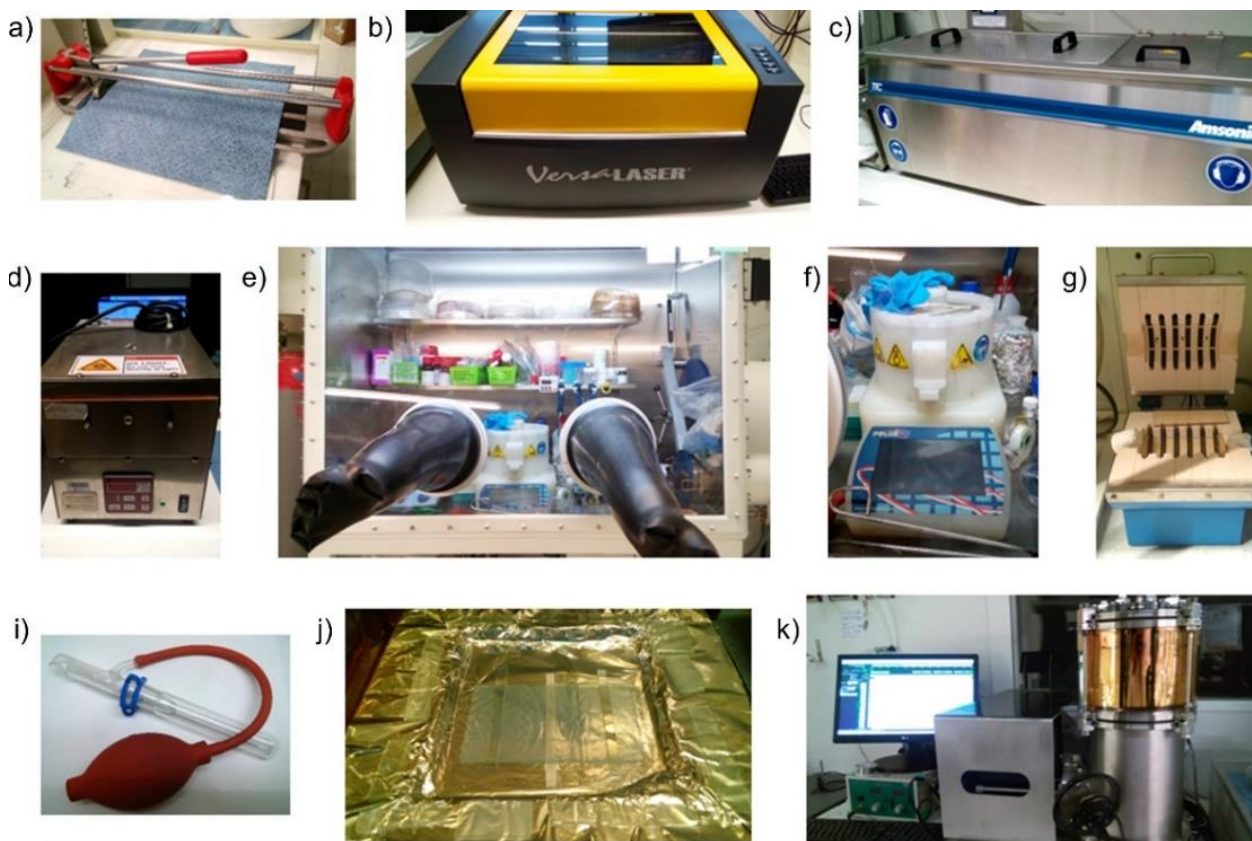


Figure 1 – Pictures of the different equipment required for the PSC fabrication: a) glass cutter, b) laser system (VersaLaser), c) ultrasonic cleaning (Amsonic), d) UV-rays system (Jelight), e) glove box (MBRAUN LABstar), f) spincoater (SPS-Europe, POLOS), g) oven (Thermolab), h) spray instrument, i) spray pyrolysis setup, and j) thermal evaporator (Oxford vacuum science).

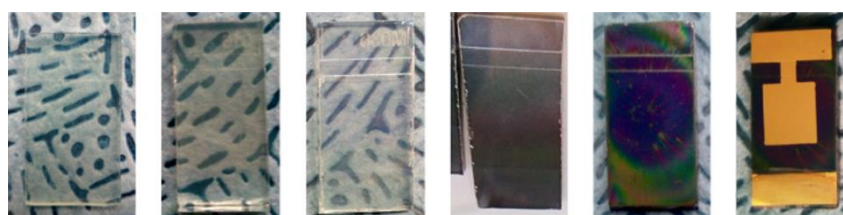


Figure 2 – Top view pictures of the PSC's layers (from left to right): glass substrate, compact TiO_2 , mesoporous TiO_2 , Perovskite, spiroOMeTAD and gold BC.

Regarding the carbon papers, two different types were acquired from Freudenberg group, H24C5 and H14C10, named here as CP1 and CP2; and a third carbon paper was acquired from SIGRACET[®], 28BC, named here as CP3. The PSCs

were first characterized using a gold layer BC. Then, the gold layer was totally peeled off with scotch tape and the carbon paper was applied above the HTM layer; a copper tape (for the connection with the external circuit), a ~2 mm thick film of polydimethylsiloxane (PDMS), and a glass substrate were then applied on the top. Finally, the stack was fixed with binder clips. Batches of 8 cells were prepared for each experimental condition, to assess reproducibility. For the PSC devices with a gold interlayer at the HTM/carbon paper, the layer of 5 nm of gold was deposited by thermal evaporation under high vacuum, following the same settings of the 60 nm layer.

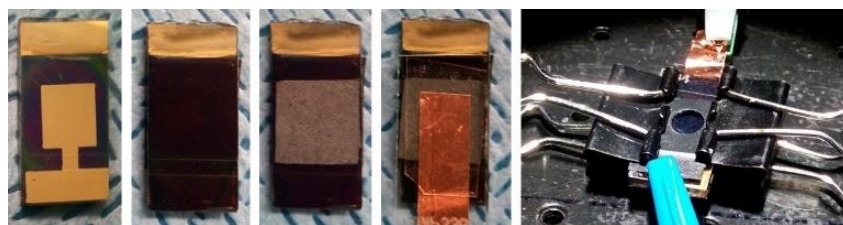


Figure 3 – Top view pictures of the steps of assembling the carbon papers on the PSCs: removing the gold BC, placing the carbon paper on top of the HTM, followed by the copper tape, PDMS film and glass piece, fix the structure with binder clips.

2.2.1. Characterization methods

The solar cell performance was evaluated using a photocurrent-voltage (J - V) characteristic curve, which was measured by a ZENNIUM workstation (Zahner Elektrik, Germany) controlled by Thales software package (Thales Z 2.0). The measurements were performed at 25 °C, under a set point simulated sunlight intensity of 1 sun (100 mW cm^{-2}), produced by a solar simulator with light-emitting diode lamp (ORIEL LSH-7320 ABA LED) calibrated with a c-Si photodiode. A characteristic curve was obtained for each cell by applying an external potential bias (V) to the cell, from negative values to positive (at a scan of 10 mV s^{-1}), and measuring the generated current (I). The measured I values were then corrected for the sample area that was effectively illuminated by the simulator for obtaining the current density (J). Through the J - V curve, it was possible to determine the

open-circuit voltage V_{OC} (potential value when no current is flowing), short-circuit current J_{SC} (current value when voltage is zero), current density, voltage and power at maximum power point (J_{MMP} , V_{MMP} and P_{MMP} , respectively), FF (ratio between the maximum power value and the maximum theoretical power value) and the power conversion efficiency (PCE) of each cell (ratio between the power generated and the power of the incident light I_s).

Electrochemical impedance spectra were obtained with a potentiostat (Gamry instruments Interface 5000E). The work-function (WF) of the carbon papers and gold was determined with an ultra-high vacuum Kelvin Probe (KPTechnology, Series 10) at ambient pressure. Contact Angle System OCA from Dataphysics was used for the contact angle measurements. Atomic force microscopy was performed by a Veeco Metrology Multimode Nanoscope IVA. Profilometer used for analyzing carbon papers' surface was Dektak XT, Bruker. Scanning electron microscopy images were obtained with the microscope FEI Quanta 400 FEG ESEM, EDAX Pegasus X4M.

2.3. Results and discussion

A 60 nm gold layer was used as reference BC and all cells will be measured with both BCs (gold and carbon paper), so as the difference in PCE in both measurements is only caused by the different BC and not attributed to the other layers of the device. As previously mentioned, the relative PCE will give a more accurate measure of the performance losses caused by the carbon paper BC. Figure 4 shows box charts of the photovoltaic performance of 18 cells with carbon papers CP1, CP2 and CP3, and the J - V curves for each configuration. Each cell was first characterized with a gold BC, followed by the three carbon papers, applied randomly. It was achieved a maximum PCE of 12.93 % (average 11.47 %) for CP1, 11.96 % (average 10.83 %) for CP2 and 7.76 % (average 6.86 %) for CP3; and a maximum relative PCE of 89 % (average 82 %) for CP1, 85 %

(average 75 %) for CP2 and 54 % (average 47 %) for CP3. CP1 is the best performing carbon BC while the previously reported CP3 is the worst.

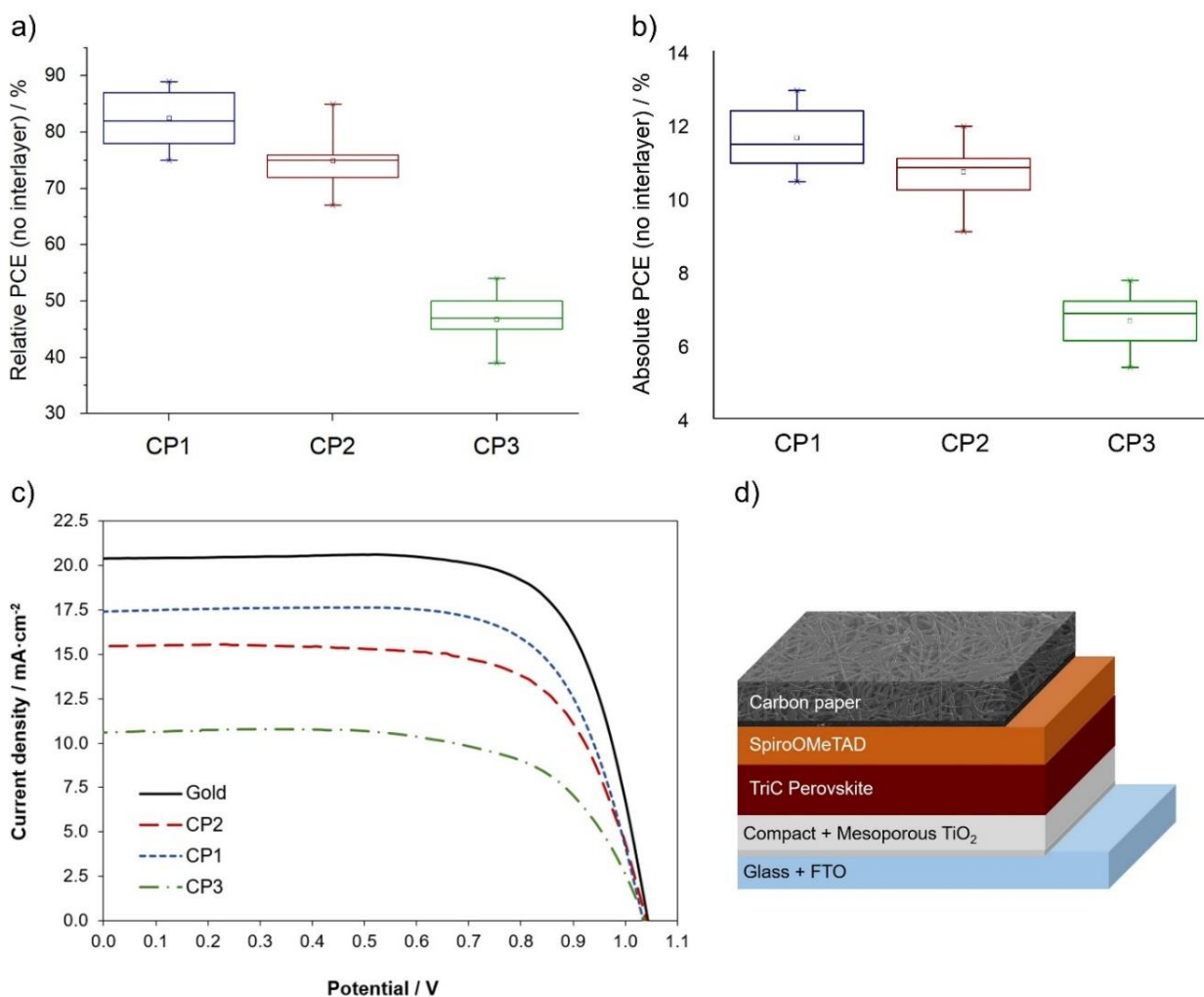


Figure 4 - Box charts of the a) relative and b) absolute PCE of 18 cells with CP1, CP2 and CP3 BCs. c) *J-V* curves (reverse scan, scan rate of 10 mV s⁻¹) of the same cell tested with 4 different BCs: 60 nm of gold, CP1, CP2 and CP3, under 1 sun irradiation. d) Illustration of the structure of the devices with a CP BC.

Carbon papers CP1 and CP2 are among the most electrically conductive carbon papers (with microporous layer coating) in the market. The measured sheet resistances are 0.53 Ω sq⁻¹ for CP1, 0.58 Ω sq⁻¹ for CP2, and 1.10 Ω sq⁻¹ for CP3. CP1 and CP2 have about half of the sheet resistance of the previously reported CP3, possibly due to the much greater density of carbon fibers, as shown in the

scanning electron microscope (SEM) images - Figure 5. Moreover, CP3 uses a graphitic paste to hold the carbon fibers together, whereas CP1 and CP2 are entirely composed by highly conductive graphite fibers. Actually, CP1's sheet resistance is very close to the sheet resistance of the 60 nm thick gold layer: $0.5 \pm 0.1 \Omega \text{ sq}^{-1}$, and it is ~ 30 times less resistive than the typical carbon layers obtained with a commercial carbon paste made of graphite and carbon black: $\sim 15 \Omega \text{ sq}^{-1}$.¹⁵ Besides the sheet resistance in the BC's bulk, the ohmic resistance at the HTM/BC interface also has a strong impact on the charge extraction efficiency. Concerning gold, since it is deposited by thermal evaporation under high vacuum, the gold atoms are deposited with high level of uniformity directly over the HTM surface, ensuring a high-quality physical contact. On the other hand, the carbon papers' interfacial resistance is defined by the surface topography and laminating force (carbon papers are flexible).

The SEM images - Figure 5 - reveal very different surface topographies of each studied carbon paper. CP1 surface shows a granular topography; CP2 has also a compact surface but with craters (up to 4 μm diameter) spread uniformly; and CP3 has a surface similar to dry mud, very smooth but with some deep cracks. The profilometer data - Figure 6a,b,c) - show that CP3 presents the roughest surface, with large peaks and valleys; CP1 is smoother and CP2 presents the smoothest surface. The measured roughness (root mean square height) was 5.0 μm for CP1, 3.9 μm for CP2 and 7.4 μm for CP3, which might indicate a better electrical charge extraction for CP2 - a rougher surface may create insulating voids that force electrical charges to be transported through a longer distance through the HTM before crossing to the BC.¹⁶ On the other hand, some roughness may create anchoring points that hold better the two surfaces. In that case, CP1 would be the best charge extractor, given the higher density of peaks and also their higher extension - distance between the bottom (purple) and upper (red) value of heights is 37.5 μm , while for CP2 is 14.1 μm and for CP3 is 25.2 μm - Figure 6.

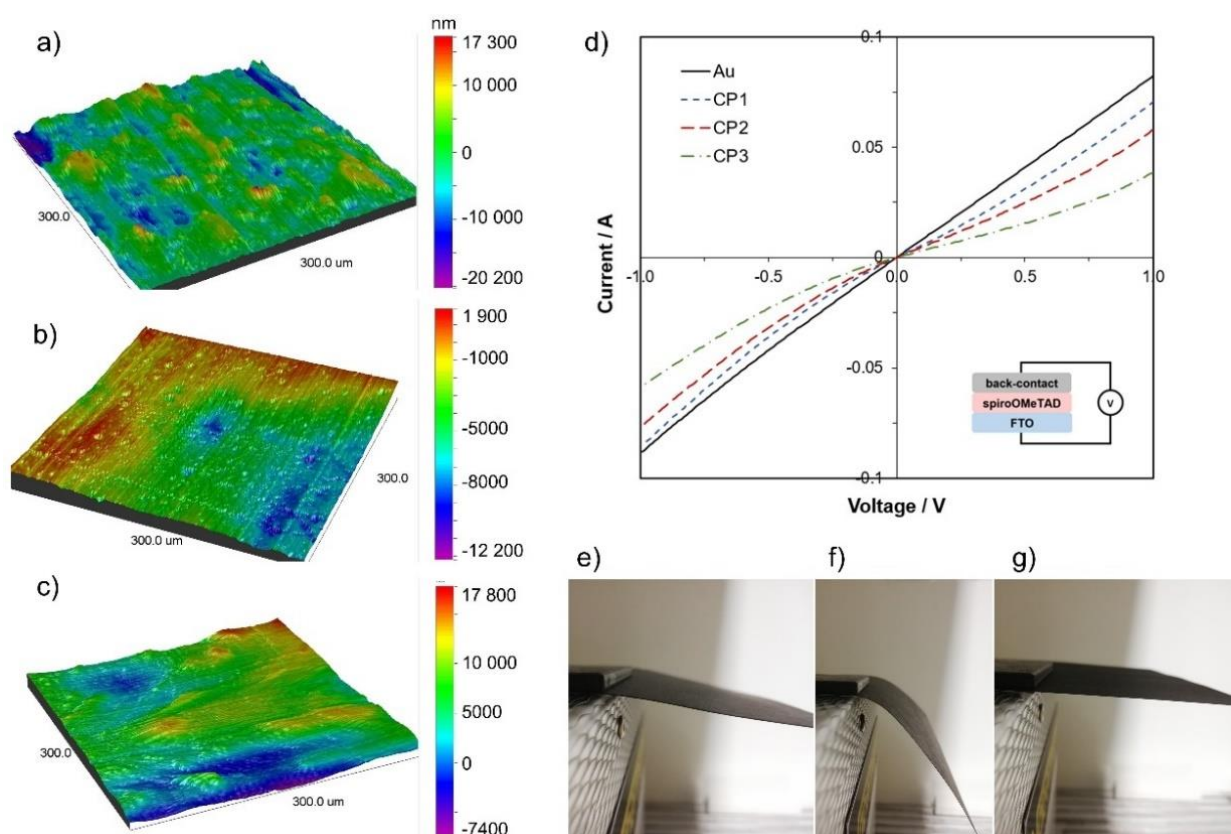


Figure 6 - Topography of the surface coated with the microporous layer of a) CP1, b) CP2 and c) CP3 obtained by profilometry. c) I-V curves of linear sweep voltammetry done in a device of FTO substrate / spiroOMeTAD / BC. Inset corresponds to the tested device. Picture demonstrating the flexibility e) CP1, f) CP2, and g) CP3.

Apart from the surface morphology, the carbon paper's flexibility also influences the effective contact area for charge extraction between the carbon paper and the HTM. CP1 and CP2 are nonwoven carbon papers with large physical comprehensibility and high resistance to crack and tear. The particular fabrication process of CP2 and its lower thickness makes it more flexible and malleable - Figure 6e,f,g). The thickness of CP1, CP2, and CP3 is 270 μm , 170 μm , and 235 μm , respectively. Consequently, when compressed against the HTM, CP2 fits better to the surface, minimizing insulating voids and maximizing charge transport. Furthermore, the difference between the work function of spiroOMeTAD and the carbon papers (-4.75 eV for CP1, -4.68 eV for CP2, -4.79 eV for CP3, -5.01 eV for gold and -5.2 eV for spiroOMeTAD) might originate a Schottky junction, and

therefore a high potential energy barrier for charge carriers' injection. In this event, the V_{OC} of the device would be smaller compared with gold.^{10, 17, 18} However, Figure 4 shows that PSCs with gold BC and carbon papers (CP1, CP2 and CP3) display approximately the same V_{OC} . To have a better understanding on the energetic nature of this interface, current-voltage (IV) characteristic curves were performed on dummy cells made of FTO coated glass / spiroOMeTAD / BC - Figure 6d). Gold device displayed a linear IV curve between -1 V and +1 V, meaning that the whole stack, including interfaces, work as an ohmic material. On the other hand, carbon papers display slightly rectifying characteristics (slightly curved line), as a result of charge accumulation at the interface spiroOMeTAD / carbon paper. Among all carbon papers, CP1 shows the lowest resistance (higher slope), actually its IV curve is almost linear - it displays an almost-ohmic behavior, and carrier charges flows with few constraints at the interface.

Most graphitic materials are hydrophobic due to the nonpolar nature of sp^2 carbon.¹⁹ However, since most carbon papers are designed to be used as a gas diffusion layer in proton-exchange membrane fuel cells, their hydrophobicity is adjusted - by polytetrafluoroethylene (PTFE) treatment - in order to obtain the specific hydrophobicity value needed for the fuel cell operation. Indeed, all the tested carbon papers present PTFE as bonding agent in the microporous layer, and since it is an insulating material, it might compromise the electric contact with the HTM.²⁰ Indeed, the carbon paper without PTFE in the carbon fibers network - CP1 - is the one with the lowest sheet resistance. X-ray photoelectron spectroscopy (XPS) measurements were performed in order to quantify the content of this insulating material in each carbon paper: Table 1 indicates the relative atomic concentration of Carbon, Oxygen and Fluorine and the graphitic fraction of the carbon at microporous layer, and Figure 7 shows the regions of interest (ROI) of the corresponding XPS spectrum. Carbon is present in the carbon fibers and carbon nanoparticles of the carbon papers but also in the PTFE layer (insulating). The graphitic fraction is only present in the carbon materials (conductive). CP3 is the carbon paper with the highest concentration of PTFE

(22.1 %), which means it has less area available for the extraction of electrical charges. CP1 presents the lowest content of PTFE at the microporous layer (16.2 %), followed closely by CP2 (17.2 %), which indicates a potentially higher conductivity at the ~40 nm thick microporous layer surface.

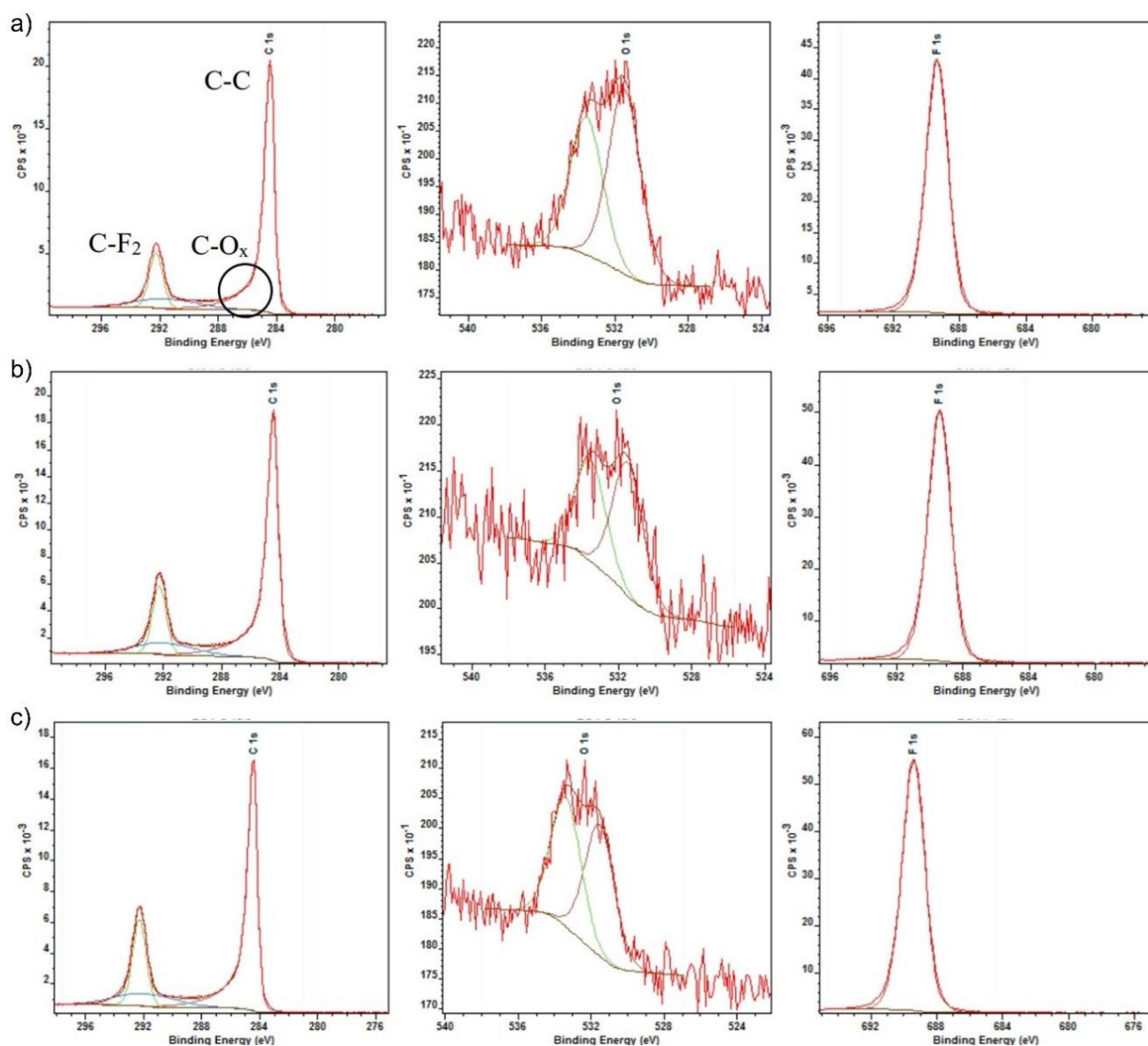


Figure 7 - Images of the XPS spectra's regions of interest – carbon, oxygen, and fluorine - of the microporous layer of a) CP1, b) CP2, and c) CP3.

Table 1 - ROI-based weight analysis (100 % normalized) of each carbon papers and carbon atomic fraction bound to PTFE and graphitic.

Element	At _{CP1} / %	At _{CP2} / %	At _{CP3} / %
Carbon	64.8	63.0	57.1
Oxygen	0.8	0.3	0.5
Fluorine	34.3	36.7	42.4
C graphitic	83.8	82.9	77.9
C PTFE	16.2	17.1	22.1

As previously mentioned, when using a carbon-based BC, the lower performance (when compared to a metallic BC) is mainly caused by a deficient contact with the underlying layer. Therefore, the charge extraction at this interface should be optimized in order to effectively increase the performance of carbon-based PSCs. A previous work employed PEDOT:PSS between spiroOMeTAD and CP3, resulting in a relative PCE increased from an average of 48 % to 54 %.¹² However, this highly conductive polymer had no effect when the BC was CP1 or CP2. Here, another strategy was adopted: deposit highly-conductive metal atoms on top of the spiroOMeTAD surface through evaporation. This ultra-thin layer, named here as interlayer, must have high chemical stability and display an aligned work function. Behrouznejad *et al.*¹ assessed different metals as BC in n-i-p PSCs and identified gold as the most suitable metal. Therefore, a 5 nm thick gold layer was evaporated onto the spiroOMeTAD layer, before assembling the carbon papers. Figure 8 shows box charts of the results of 18 cells characterized with CP1, CP2 and CP3 BC with 5 nm gold interlayer; and J-V curves of a representative cell with each configuration.

A maximum PCE of 13.87 % (average 12.97 %) for CP1, 13.00 % (average 11.80 %) for CP2 and 11.70 % (average 8.25 %) for CP3; and a maximum relative PCE of 92 % (average 87 %) for CP1, 90 % (average 80 %) for CP2 and 81 % (average 55 %) for CP3 was achieved with the addition of the gold interlayer. The higher photovoltaic performance resulted mainly from a large increase in the

current density. This behavior was expected since the enhancement of the electrical contact due to the ultra-thin gold layer results in an increase of the charge carrier's extraction efficiency at the interface between the HTM and carbon paper. Moreover, the gold thin interlayer also improved the reproducibility for CP1 and CP2. CP1 is again the most promising carbon paper, with a PCE close to the one obtained with gold BC. Gold interlayer was observed by atomic force microscopy (AFM) to disclose its morphology - Figure 9a). Gold atoms deposited on spiroOMeTAD layer present a surface full of sharp peaks, which creates points of lower electrical resistance.

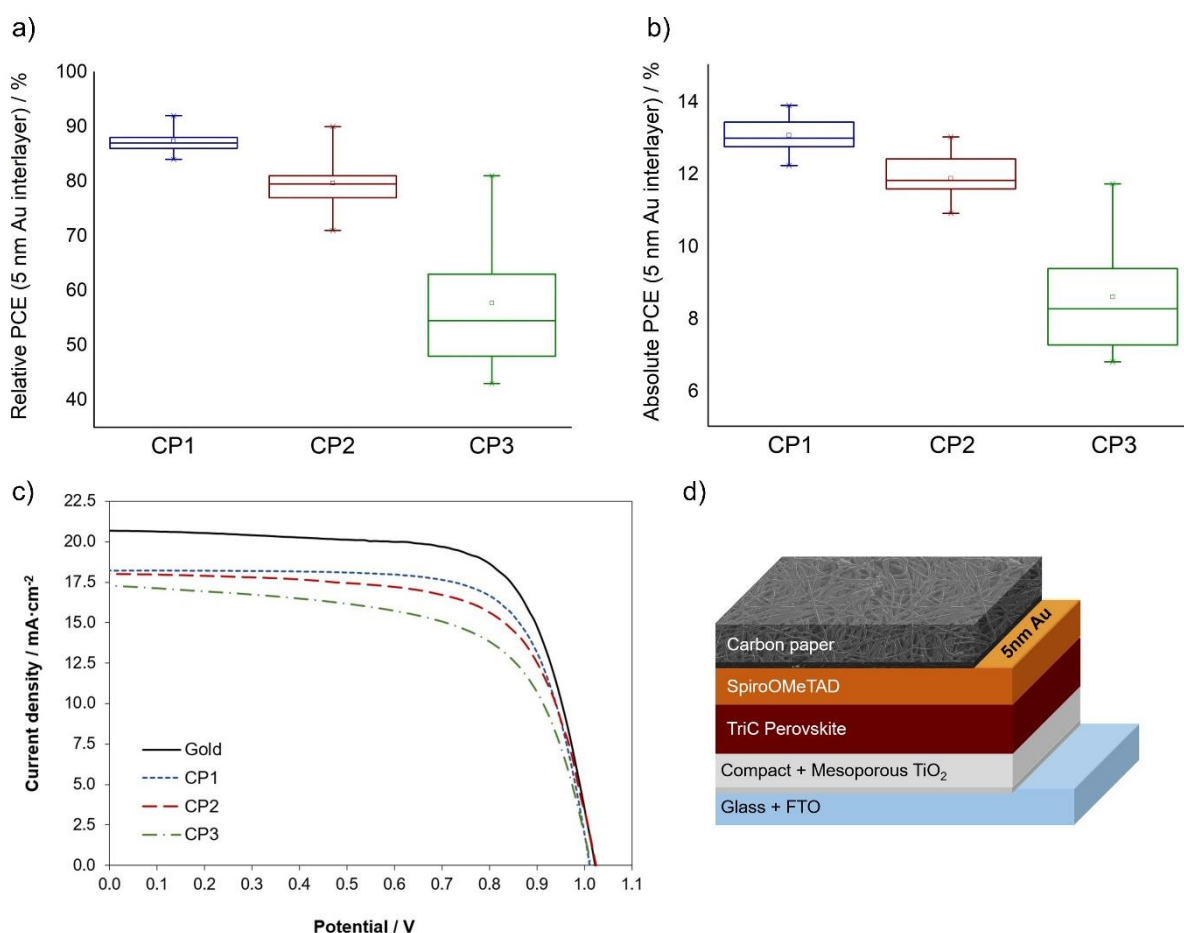


Figure 8 - Box charts of the a) relative and b) absolute PCE of 18 cells with 5 nm of gold as interlayer, tested with CP1, CP2 and CP3 BCs. c) *J-V* curves (reverse scan, scan rate of 10 mV s⁻¹) of representative cell tested with CP1, CP2 and CP3 as BC, with 5 nm of gold as interlayer and under 1 sun radiation. d) illustration of the structure of the devices with a CP BC.

To evaluate the charge transfer kinetics at this new interface, electrochemical impedance spectroscopy (EIS) measurements were performed for PSCs assembled with the different BCs, applying a potential difference near the open circuit voltage. The interfacial charge transfer and bulk transport resistance at the BC in the high frequency region (10^4 to 10^6 Hz) were modelled by a parallel combination of a constant phase element (CPE) and a resistor element. The Nyquist plots and the resistance and constant phase element values obtained by fitting results in the assumed model for each configuration are presented in Figure 9b,c) and in. CP1 presents the lower interfacial resistance, followed by CP2 and CP3. As expected, the gold interlayer decreases the resistance in about 50 % for CP1 and 13 % for CP2 and 10 % for CP3.

Table 2 - Resistance and constant phase element values obtained by fitting results in the assumed model, for each carbon paper with and without interlayer.

Carbon paper	R [Ω]	CPE [F]	n
CP1 + Au interlayer	138	1.61×10^{-7}	0.93
CP1	259	1.79×10^{-7}	0.93
CP2 + Au interlayer	1083	1.67×10^{-7}	0.93
CP2	1247	1.24×10^{-7}	0.94
CP3 + Au interlayer	2842	2.37×10^{-7}	0.87
CP3	3170	1.13×10^{-7}	0.91

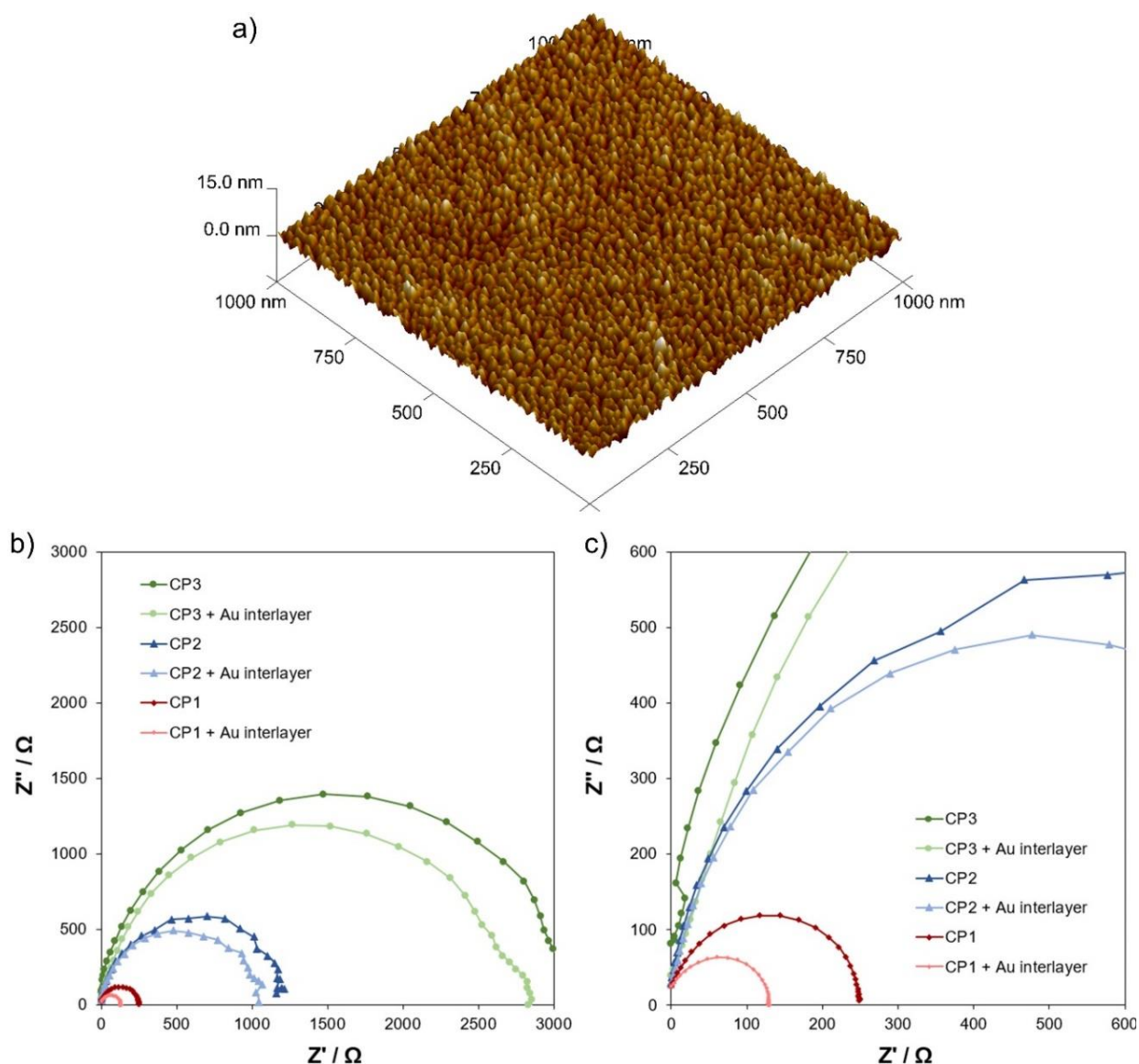


Figure 9 - a) AFM image of 5 nm of gold deposited by thermal evaporation under high vacuum. b) Nyquist plots for PSCs with six different BCs: CP1, CP2 and CP3 with and without 5 nm of gold as interlayer. b) Zoom at the CP1 nyquist plot.

In terms of stability, carbon materials are known to be highly stable and they are expected to outstand extreme conditions such as moisture, pressure and temperature for long periods of time, contrary to the usual metals used as BC in PSCs. Moreover, their high hydrophobic (contact angle higher than 150° - Figure 10) is also beneficial for the cells stability, since the perovskite layer is highly sensitive to moisture.²¹ Domanskit et al. reported that gold diffuse into the

perovskite inner layers when the device is subjected to temperatures higher than 70 °C.²² This fact raises stability issues related with the 5 nm gold interlayer employed in this work. However, a previous work in our lab demonstrated that when the cell is subjected to 80 °C, the loss of performance is caused by the degradation of spiroOMeTAD and not by gold diffusion. Actually, XPS analysis revealed no gold in the cell's inner layers.²³

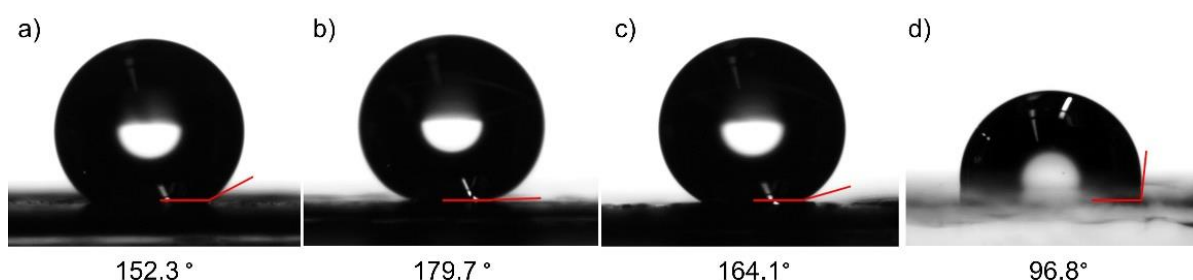


Figure 10 - Contact angle test of (a) CP1, (b) CP2, (c) CP3 and (d) of a thin gold layer.

Overall, carbon papers proved to be a promising material for back-contact, having a good performance at extracting the photogenerated charge carriers, and a potential long-term stability. Furthermore, the assembling method (lamination) is straightforward, simple, and widely used in industry. However, the high thickness of the papers and their poor adhesion to the underlying layer might raise some engineering issues related with the device patterning on module level.

2.4. Conclusion

In conclusion, three different highly conductive carbon papers made of carbon fibers and a microporous coating of carbon black and graphite were used as back contact (BC) in PSCs. The carbon paper attachment was obtained by pressing it against the HTM of the device. Each cell was tested with the four BCs: gold and carbon papers CP1, CP2 and CP3. This procedure is not often reported but allows a better assessment of the BC performance. The carbon paper presenting the best

photovoltaic performance was CP1: maximum PCE of 12.93 %, corresponding to 89 % of the PCE obtained with the typical gold BC - relative PCE. Indeed, this carbon paper presented the lower sheet resistance, and its microporous layer presented a proper surface morphology (moderate roughness but high density of peaks that create anchoring points with the HTM), and the lowest PTFE content (directly related with a higher conductivity). These features resulted in a nearly ohmic contact at the HTM/carbon paper interface, resulting in no V_{oc} loss relatively to PSC with gold BC. The highly flexible CP2 also presented a high PCE of 11.96 %, and relative PCE of 85 %. The photovoltaic performance was further improved by applying an interlayer of 5 nm of gold between the carbon paper and HTM. With this interlayer, a maximum PCE of 13.87 % (13.00 %) and an impressive relative PCE 92 % (90 %) was obtained for CP1 (CP2).

Acknowledgements

Cristina O. Teixeira acknowledges project SolarPerovskite - NORTE-01-0145-FEDER-028966 funded by FEDER funds through NORTE 2020 - Programa Operacional Regional do NORTE – and by national funds (PIDDAC) through FCT/MCTES for funding; L. Andrade acknowledges FCT for funding (IF/01331/2015). The authors also acknowledge European Union's Horizon 2020 Programme, through a FET Open research and innovation action under grant agreement No 687008 (GOTSolar project). This work was also partially supported by Project WinPSC (POCI-01-0247-FEDER-017796) co-funded by the European Regional Development Fund (ERDF), through the Operational Programme for Competitiveness and Internationalisation (COMPETE 2020), under PORTUGAL 2020 Partnership Agreement; POCI-01-0145-FEDER-006939 (LEPABE - UID/EQU/00511/2013), funded by the ERDF, through COMPETE 2020 and by national funds through FCT; and NORTE-01-0145-FEDER-000005 – LEPABE-2-ECO-INNOVATION, supported by North Portugal Regional Operational

Programme (Norte 2020), under the Portugal2020 Partnership Agreement, through the ERDF. The authors are also very thankful to CEMUP for AFM, SEM, profilometry and XPS analysis, to ARCP for contact angle determination, and to Mafalda Pereira for Kelvin Probe measurements.

References

1. Behrouznejad, F.; Shahbazi, S.; Taghavinia, N.; Wu, H.-P.; Wei-Guang Diao, E., A study on utilizing different metals as the back contact of CH₃NH₃PbI₃ perovskite solar cells. *Journal of Materials Chemistry A* **2016**, *4* (35), 13488-13498.
2. Ferguson, V.; Silva, S. R. P.; Zhang, W., Carbon Materials in Perovskite Solar Cells: Prospects and Future Challenges. *ENERGY & ENVIRONMENTAL MATERIALS* **2019**, *2* (2), 107-118.
3. Yu Cai, L. L., Peng Gao, Promise of Commercialization: Carbon Materials for Low-Cost Perovskite Solar Cells. **2017**.
4. Zhang, F.; Yang, X.; Wang, H.; Cheng, M.; Zhao, J.; Sun, L., Structure Engineering of Hole-Conductor Free Perovskite-Based Solar Cells with Low-Temperature-Processed Commercial Carbon Paste As Cathode. *ACS Applied Materials & Interfaces* **2014**, *6* (18), 16140-16146.
5. Chu, Q.-Q.; Ding, B.; Peng, J.; Shen, H.; Li, X.; Liu, Y.; Li, C.-X.; Li, C.-J.; Yang, G.-J.; White, T. P.; Catchpole, K. R., Highly stable carbon-based perovskite solar cell with a record efficiency of over 18% via hole transport engineering. *Journal of Materials Science & Technology* **2019**.
6. Arora, N.; Dar, M. I.; Akin, S.; Uchida, R.; Baumeler, T.; Liu, Y.; Zakeeruddin, S. M.; Grätzel, M., Low-Cost and Highly Efficient Carbon-Based Perovskite Solar Cells Exhibiting Excellent Long-Term Operational and UV Stability. *Small* **2019**, *15* (49), 1904746.
7. Zhang, H.; Xiao, J.; Shi, J.; Su, H.; Luo, Y.; Li, D.; Wu, H.; Cheng, Y.-B.; Meng, Q., Self-Adhesive Macroporous Carbon Electrodes for Efficient and Stable Perovskite Solar Cells. *Advanced Functional Materials* **2018**, *28* (39), 1802985.
8. Meng, F.; Liu, A.; Gao, L.; Cao, J.; Yan, Y.; Wang, N.; Fan, M.; Wei, G.; Ma, T., Current progress in interfacial engineering of carbon-based perovskite solar cells. *Journal of Materials Chemistry A* **2019**, *7* (15), 8690-8699.
9. Wu, X.; Xie, L.; Lin, K.; Lu, J.; Wang, K.; Feng, W.; Fan, B.; Yin, P.; Wei, Z., Efficient and stable carbon-based perovskite solar cells enabled by the inorganic interface of CuSCN and carbon nanotubes. *Journal of Materials Chemistry A* **2019**, *7* (19), 12236-12243.
10. Lee, J.-W.; Jeon, I.; Lin, H.-S.; Seo, S.; Han, T.-H.; Anisimov, A.; Kauppinen, E. I.; Matsuo, Y.; Maruyama, S.; Yang, Y., Vapor-Assisted Ex-Situ Doping of Carbon Nanotube toward Efficient and Stable Perovskite Solar Cells. *Nano Letters* **2019**, *19* (4), 2223-2230.

11. You P, L. Z., Tai Q, Liu S, Yan F, Efficient Semitransparent Perovskite Solar Cells with Graphene Electrodes. *Advanced materials* **2015**, 27 (24), 3632-8.
12. Teixeira, C. O.; Andrade, L.; Mendes, A., Novel carbon-based material for perovskite solar cells back-contact. *International Journal of Energy Research* **2019**, 43 (13), 7541-7546.
13. Gholipour, S.; Correa-Baena, J.-P.; Domanski, K.; Matsui, T.; Steier, L.; Giordano, F.; Tajabadi, F.; Tress, W.; Saliba, M.; Abate, A.; Morteza Ali, A.; Taghavinia, N.; Grätzel, M.; Hagfeldt, A., Highly Efficient and Stable Perovskite Solar Cells based on a Low-Cost Carbon Cloth. *Advanced Energy Materials* **2016**, 6 (20), 1601116.
14. Michael Saliba, T. M., Ji-Youn Seo, Konrad Domanski, Juan-Pablo Correa-Baena, Mohammad Khaja Nazeeruddin, Shaik M. Zakeeruddin, Wolfgang Tress, Antonio Abate, Anders Hagfeldt and Michael Gratzel, Cesium-containing triple cation perovskite solar cells: improved stability, reproducibility and high efficiency. *Energy & Environmental Science* **2016**, 9.
15. Solaronix Elcocarb B/SP - Graphite/carbon-black paste for the deposition of active highly conductive carbon layers by screen-printing in photovoltaic applications. <https://shop.solaronix.com/conductive-pastes/carbon-pastes/elcocarb-b-sp.html>.
16. Yang, Y.; Xiao, J.; Wei, H.; Zhu, L.; Li, D.; Luo, Y.; Wu, H.; Meng, Q., An all-carbon counter electrode for highly efficient hole-conductor-free organo-metal perovskite solar cells. *RSC Advances* **2014**, 4 (95), 52825-52830.
17. Wang, L.; Li, G.-R.; Zhao, Q.; Gao, X.-P., Non-precious transition metals as counter electrode of perovskite solar cells. *Energy Storage Materials* **2017**, 7, 40-47.
18. Caprioglio, P.; Stolterfoht, M.; Wolff, C. M.; Unold, T.; Rech, B.; Albrecht, S.; Neher, D., On the Relation between the Open-Circuit Voltage and Quasi-Fermi Level Splitting in Efficient Perovskite Solar Cells. *Advanced Energy Materials* **2019**, 9 (33), 1901631.
19. Kozbial, A.; Zhou, F.; Li, Z.; Liu, H.; Li, L., Are Graphitic Surfaces Hydrophobic? *Accounts of Chemical Research* **2016**, 49 (12), 2765-2773.
20. Rudiger Schwelss, C. M., Tanja Damjanovic, Ivano Gaibati, Nico Haak, SIGRACET® Gas Diffusion Layers for PEM Fuel Cells, Electrolyzers and Batteries. Company, S. G.-T. C., Ed. 2018.
21. Mesquita, I.; Andrade, L.; Mendes, A., Effect of relative humidity during the preparation of perovskite solar cells: Performance and stability. *Solar Energy* **2020**, 199, 474-483.
22. Domanski, K.; Correa-Baena, J.-P.; Mine, N.; Nazeeruddin, M. K.; Abate, A.; Saliba, M.; Tress, W.; Hagfeldt, A.; Grätzel, M., Not All That Glitters Is Gold: Metal-Migration-Induced Degradation in Perovskite Solar Cells. *ACS Nano* **2016**, 10 (6), 6306-6314.
23. Mesquita, I.; Andrade, L.; Mendes, A., Temperature Impact on Perovskite Solar Cells Under Operation. *ChemSusChem* **2019**, 12 (10), 2186-2194.

CHAPTER 3

OPTIMIZATION OF A HIGHLY EFFICIENT AND FLEXIBLE PEROVSKITE SOLAR CELL FOR INDOOR APPLICATIONS

Adapted from the peer-reviewed article:

Charge Extraction in Flexible Perovskite Solar Cell Architectures for Indoor Applications – with up to 31 % Efficiency

Cristina Teixeira, Pierpaolo Spinelli, Luigi Angelo Castriotta, David Müller, Senol Öz, Luísa Andrade, Adélio Mendes, Aldo Di Carlo, Uli Würfel, Konrad Wojciechowski, Dávid Forgács; *Advanced Functional Materials* **32** (2022) p:2206761.

OPTIMIZATION OF A HIGHLY EFFICIENT AND FLEXIBLE PEROVSKITE SOLAR CELL FOR INDOOR APPLICATIONS

3.1. Introduction

Eliminating the high energy-demanding process of thermal evaporation under high-vacuum is already a step closer towards achieving a device architecture compatible with industrial manufacturing processes - all layers are now deposited by solution-based methods (spray-pyrolysis and spin-coating), and lamination (for carbon). At this point, there are so many possible paths that can be taken to achieve the final goal that it is more effective to specifically define the PSC final application, for instance, to know at which lighting conditions the PSC will operate. Commonly, photovoltaic technologies are designed to maximize the conversion of sunlight into electricity. However, these technologies can also generate electricity under other lighting conditions, like in the space applications, in which the light intensity is much higher, or in indoor environments, in which the light source are the lamps with irradiances ~300 times lower than the sunlight.¹

As discussed in chapter 1, subchapter 5 (applications), PSC technology is a potential market disruptor for indoor PV applications given its very high efficiency under low light and the increasing market growth of indoor IoT industry.² Apart from the lighting conditions, the selection of substrate will also have a strong impact in the final cost, performance and application. The two most common types of substrates are soda-lime glass and polyester-based polymer, both coated with a thin layer of a highly conductive metal oxide. The coatings on glass substrates

are usually more conductive, smoother and can withstand much higher temperatures than the polymer substrates, which results in higher efficiencies (PCE record for 26.1 %³, while for polymer substrate is 22.4 %⁴). However, polymers are flexible, lighter, thinner, non-brittle, and can be used in a high-throughput R2R fabrication process, which is definitely a plus in the manufacturing perspective.⁵

As such, the focus of this research was then aimed at optimizing the fabrication process of PSC on a flexible polymer-based substrate, in order to achieve high efficiency under low indoor light. Since the maximum working temperature is 140 °C (for temperatures above this value, the polymer-based foil starts bending), the mesoporous TiO₂ layer has to be replaced by planar SnO₂, and the perovskite composition was tuned to better align its band gap with the spectrum of indoor lighting, without compromising stability. Also, in terms of R2R processing, it is preferable to use a solution deposition method for the carbon-based back-contact, instead of the laminated carbon paper. In this chapter, three flexible PSC architectures are presented for indoor applications: first a PSC with an evaporated gold electrode was developed, to maximize efficiency (reference device). Then the gold was replaced by a blade coated carbon electrode to make the fabrication process compatible with large scale production by a R2R process, and finally the hole transport material (HTM) was removed to maximize stability and simplify the fabrication process.

A maximum efficiency of 30.9 % at 1000 lux and 30.0 % at 200 lux was obtained for the metal electrode-based configuration, whereas the carbon-based electrode devices with and without poly(3-hexylthiophene-2,5-diyl) (P3HT) presented a maximum efficiency of 25.4 % and 23.1 % at 1000 lux and 24.7 % and 22.3 % at 200 lux, respectively. The lamp selected was a ~3270 K warm white LED, with an irradiance of 393.6 $\mu\text{W cm}^{-2}$ (76.4 $\mu\text{W cm}^{-2}$) at 1000 lux (200 lux). The perovskite composition was selected to better align its band gap with the spectrum of indoor lighting, while ensuring a highly stable and halide-segregation resistant formulation. Pseudo-current/voltage curves (suns-QFLS and suns-V_{OC}), external

quantum efficiency, ideality factor, transient-photocurrent decay, transient-photovoltage decay, impedance spectroscopy and four-point probe measurements were performed on the three configurations to have a better understanding on the charge carriers' extraction efficiency and recombination dynamics. Furthermore, maximum power point tracking (MPPT) at 0.6 suns and thermal test at 85 °C was performed in non-encapsulated devices to assess the operational and thermal stability. HTM-free carbon-based electrode devices presented an impressive stability, retaining about 84 % of their initial power density after 1000 h at MPPT and keeping virtually the same efficiency after 1000 h at 85 °C. On the other hand, HTM+carbon and HTM+gold configurations lost 41 % and 77 % of their initial power density after the 1000 h and 300 h at MPPT, respectively, and lost both about 15 % of their initial efficiency after 1000 h at 85°C.

3.2. Experimental Section

3.2.1. Materials and flexible PSC fabrication

The first step is the substrate preparation. The substrate consisted in a 210 µm thick PET substrate covered with a layer of IZO (~270 nm) with a sheet resistance of 15-20 Ω s⁻¹ and a transparency of 80 % (Eastman). The substrates were cut down to small cells of 1.8 x 1.2 cm² and were sonicated for 10 minutes in deionized water and then IPA. After drying with a N₂ gun, the IZO surface was treated with oxygen plasma for 20 seconds. SnO₂ dispersion was made by diluting the aqueous 15 % SnO₂ colloidal dispersion (Alfa Aesar) down to 3 %, and was spin coated right after the plasma treatment at 2500 rpm for 30 seconds (acceleration of 1250 rpm s⁻¹). After annealing at 100°C for 40 minutes in a hot plate, the cells were transferred to a N₂ filled glovebox. The perovskite precursors CsI (Sigma-Aldrich 99.99 %), FAI (dynamo 99.99 %), PbI₂ (TCI 99.99 %), and PbBr₂ (Sigma-Aldrich >98 %) were weighted according with the formula Cs_{0.17}FA_{0.83}Pb(I_{0.7}Br_{0.3})₃,

(keeping 10 % excess of PbI_2) and dissolved in mixed solvents DMF:DMSO = 4:1, with a molarity of 1.2M. The solution was stirred for 2 hours and used right away. The perovskite solution was spin-coated on top of SnO_2 layer (pre-treated with 10 min UV light) using a three-step spinning program: 1000 rpm for 2 seconds, 5000 rpm for 18 seconds and 6000 rpm for 20 seconds; 120 μL of ethyl acetate was dispensed on the sample 10 seconds before the end of the spinning program. After naturally drying for 4 minutes, the substrate was transferred to a hotplate at 100 °C and annealed for 30 minutes.

For the hole transporting material (HTM), a doped spiro-MeOTAD (Sigma-Aldrich, ≥ 99 % HPLC) solution was prepared: 72.3 mg mL^{-1} in chlorobenzene, plus 28.8 $\mu\text{L mL}^{-1}$ of tBP and 17.5 $\mu\text{L mL}^{-1}$ of a stock solution of Li-TFSI (Sigma-Aldrich, ≥ 99 %) - stock solution: 520 mg mL^{-1} Li-TFSI in acetonitrile. In case of P3HT (Xi'an Polymer Light Technology Corp.), a solution of 10 mg mL^{-1} in 1,2-Dichlorobenzene without dopants was prepared, and stirred for 2 hours at 75 °C. Both HTM solutions were spin-coated outside the glovebox at 3000 rpm for 30 seconds. All solvents were acquired from Sigma-Aldrich, are anhydrous and have a purity ≥ 99.8 %. In case of the metal-based devices, 50 nm of gold ($0.5 \Omega \text{ sq}^{-1}$) was thermally evaporated under high vacuum ($\sim 10^{-6}$ bar) following this procedure: 0.02 A s^{-1} until 5 nm; 0.05 A s^{-1} until 20 nm; 0.2 A s^{-1} until 50 nm. For the carbon-based electrode devices, carbon paste was blade-coated on top of the perovskite or the HTM layer with a glass rod and annealed inside an oven at 85 °C for 30 minutes (carbon thickness $\sim 15 \mu\text{m}$).

3.2.2. Characterization methods

Current density–voltage characterization and stabilized power output measurements were performed using a Keithley 2461 source measure unit under a warm white LED (CLU028-1201C4-303H7M5-F1, Citizen Electronics, ~ 3270 K); Illuminance was set to 200 lux and 1000 lux. The absolute spectrum at each illuminance value was determined with the spectrometer SEKONIC C-800

Spectromaster, and irradiance was calculated by integrating the area of the spectrum obtained.

For the measurements at simulated AM1.5G irradiation (100 mA cm^{-2}), an AAA-rated solar simulator (Abet Technologies, sun 2000) was used, calibrated against an RR-208-KG5 silicon reference cell (Abet Technologies). Solar cells were masked to 0.64 cm^2 . J-V measurements were performed in two scan directions, from forward bias to short-circuit and from short-circuit to forward bias. The scanning rate was set to 0.5 V s^{-1} . The stabilized power conversion efficiency (SPO) was measured at the maximum power point voltage for a duration of 30 seconds.

For the scanning electron microscopy cross-section images, a local section was first created with ion beam in the device stack, and then the microscope FEI Helios NanoLab™ 600i was used to obtain the images. The external quantum efficiency (EQE) was measured using Bentham PVE300 photovoltaic characterization system and the control software BenWin+. Optical simulations were performed by the Transfer Matrix method using a home written Python code. Both the Maximum Power Point Tracking and Bending Test were performed with equipment and software designed by the engineers at Saule S.A.

Absolute photoluminescence measurements were performed in a hyperspectral imaging microscope (Photon Etc). A green laser (wavelength: 532 nm) was used as excitation source. The laser was focused onto the surface of the perovskite layer using a 50x objective, resulting in a spot size with $380 \text{ }\mu\text{m}$ diameters. The photoluminescence from the perovskite layer was collected through the same objective and analyzed with the hyperspectral imager (IMA-VISTM, Photon Etc). The different illumination intensities were obtained by changing the laser power and using optical neutral density filters, and they were calibrated using an optical power meter. To analyze the perovskite of degraded devices after the MPPT, gold layer was removed with scotch tape, spirOMeTAD was removed by spin-coating chlorobenzene, and carbon and P3HT layers were removed by soaking the device in anisole.

The suns- V_{OC} plot was obtained by measuring the J-V curve at different light intensities and extracting the V_{OC} value obtained. The first measurement was at 1000 W m^{-2} , then the measurements were performed from the lower to the higher light intensity. The voltage obtained in the 1st and last measurement for all configurations differs in less than 1 %. The different light intensities were obtained by using neutral density filters with optical density between (OD) 0.5 and 4 (Thorlabs) in a AM1.5G sun simulator: 316.2 W m^{-2} (OD0.5), 100 W m^{-2} (OD1), 10 W m^{-2} (OD2), 1 W m^{-2} (OD3) and 0.1 W m^{-2} (OD4).

Transient photovoltage decay (TPV) and transient photocurrent decay (TPC) measurements were performed with an all-in-one platform (ARKEO - Cicci Research) composed by multichannel 4-wire source meters, 100 MS s^{-1} digitizer and Arbitrary function generators. A rigid metal opaque mask of 0.1 cm^2 was applied during the measurements. Devices were connected to a transimpedance amplifier and a differential voltage amplifier to monitor short-circuit current or open-circuit voltage. The measurements were executed with varied light intensities. TPV is performed in small perturbation regime: LED is always on at specified intensities and a small over current is sent to the LED just few percentages of power to create a voltage perturbation on the device in the range of 20 mV. The test is repeated at different light intensities. TPC is performed in high perturbation regime: cell is always in short circuit condition. Current decay is integrated after the light is switched off. The intensities were cycled at 6 different levels (304, 452, 600, 744, 892, and 1036 W m^{-2}), using the white LED. For each intensity level, 2000 traces were recorded. Measurements were performed at CHOSE, Italy.

Electrochemical impedance spectra (EIS) were obtained with a potentiostat (Gamry instruments Interface 5000E) over a frequency range of $1 \text{ Hz} - 1 \times 10^5 \text{ Hz}$ with AC amplitude of 10 mV in the dark. The measurements were carried out at room temperature after the open circuit voltage was stabilized. The EIS spectra were fitted to an appropriate electrical analogue by means of the ZView software (v4.0e, Scribner Associates Inc.). Measurements were performed at LEPABE, Portugal.

3.3. Results and discussion

3.3.1. Perovskite layer characterization

When designing the perovskite formulation for low-light applications, there are two particular factors that must be taken into account for maximizing the harvesting of this low-light and its conversion into electrical power, which are the bandgap of the perovskite and its defect density (that can be quantified in the shunt resistance).⁶ The bandgap value that maximizes the light absorption and power conversion efficiency at artificial low-light conditions lies between 1.7 and 2.0 V depending on the spectrum of the light source.⁷ These wide-bandgap perovskites are usually attained by increasing the bromide content. However, since high bromide content also results in a more significant photo-induced phase-segregation, typically cesium concentration is also increased since it has proven to hinder this degradation process.⁸ Thus, the perovskite formulation selected for this study was $\text{Cs}_{0.17}\text{FA}_{0.83}\text{Pb}(\text{I}_{0.7}\text{Br}_{0.3})_3$. As seen in Figure 1f,g), the photoluminescence (PL) peak of this composition both under 0.11 and 1.67 suns at different points of the perovskite surface locates at 720 nm, which corresponds to a bandgap of 1.72 eV. The energetic alignment of the selected layers is presented in Figure 1c). Absorbance measurements - Figure 1a) - were also performed and converted into a Tauc plot - Figure 1b). By this plot it was possible to extract the value of the bandgap, which corresponded to the one obtained by PL: 1.72 eV.

When photovoltaic cells are working at indoor low light the density of photo-generated charge carriers' is lower than that under outdoor lighting conditions. Consequently, a larger portion of these few charge carriers will be trapped by the defects and the decrease in the net generated current in low-light conditions will be more significant than in outdoors.⁶ The photoluminescence maps presented in Figure 1d,e) shows the high uniformity level of the obtained perovskite layer, corresponding to an average PL peak of 6.5×10^{13} photons $(\text{eV s cm}^2 \text{ sr})^{-1}$ at 110 W m^{-2} and 3.5×10^{15} photons $(\text{eV s cm}^2 \text{ sr})^{-1}$ at 1670 W m^{-2} . Furthermore, as

seen in the scanning electron microscope (SEM) images - Figure 2 - the perovskite layer has a thickness of about 500 nm and it is composed by large grains. Both these results demonstrate the high quality of the fabricated wide band-gap perovskite.

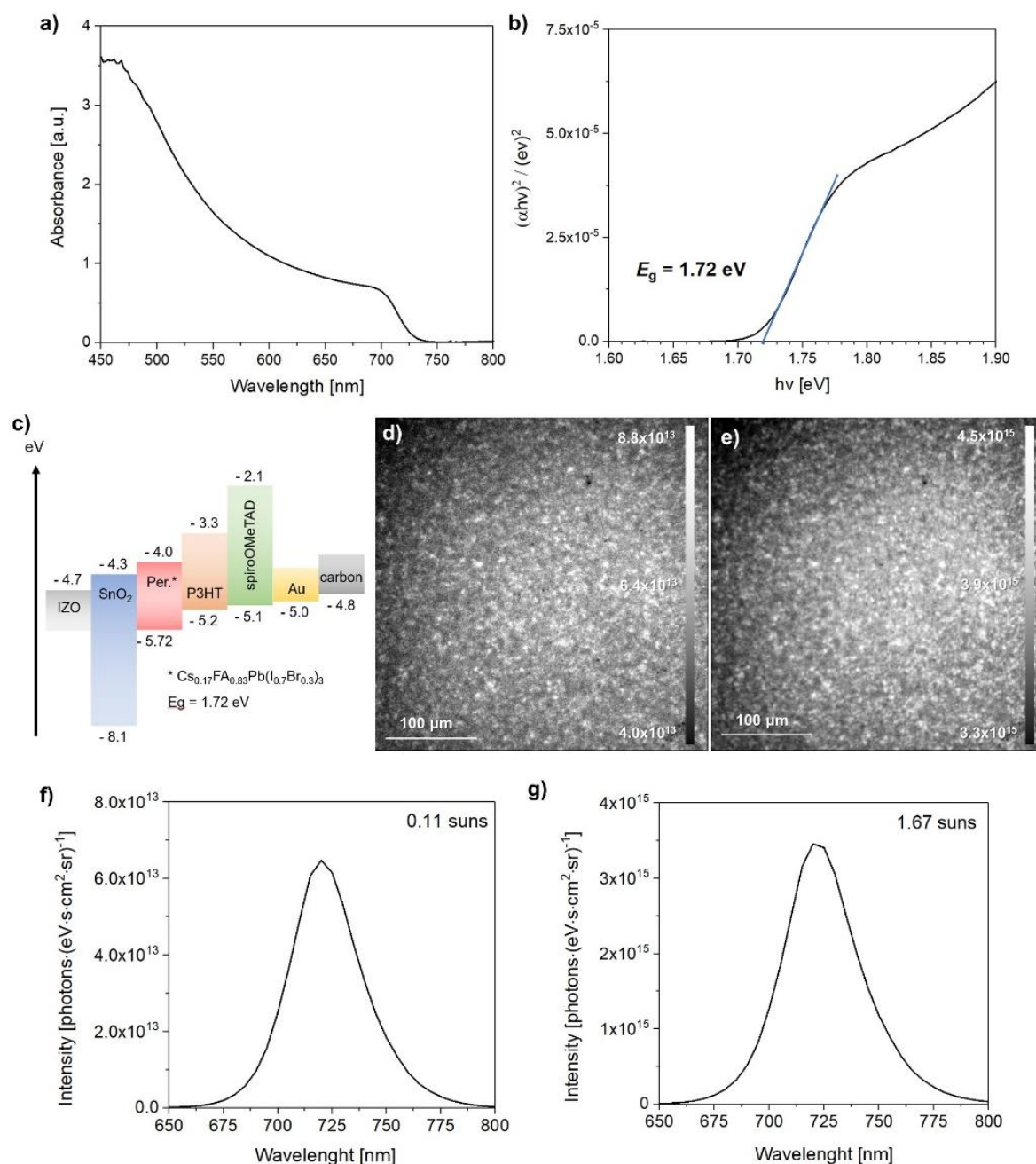


Figure 1 – a) Absorbance spectrum and b) tauc plot of the perovskite film. c) Energetic alignment of the selected layers for this study Photoluminescence calibrated maps⁹ and spectra obtained for the perovskite $\text{Cs}_{0.17}\text{FA}_{0.83}\text{Pb}(\text{I}_{0.7}\text{Br}_{0.3})_3$ deposited onto SnO_2 on a flexible substrate at d,f) 0.11 suns - 110 W m^{-2} and e,g) 1.67 suns - 1670 W m^{-2} .

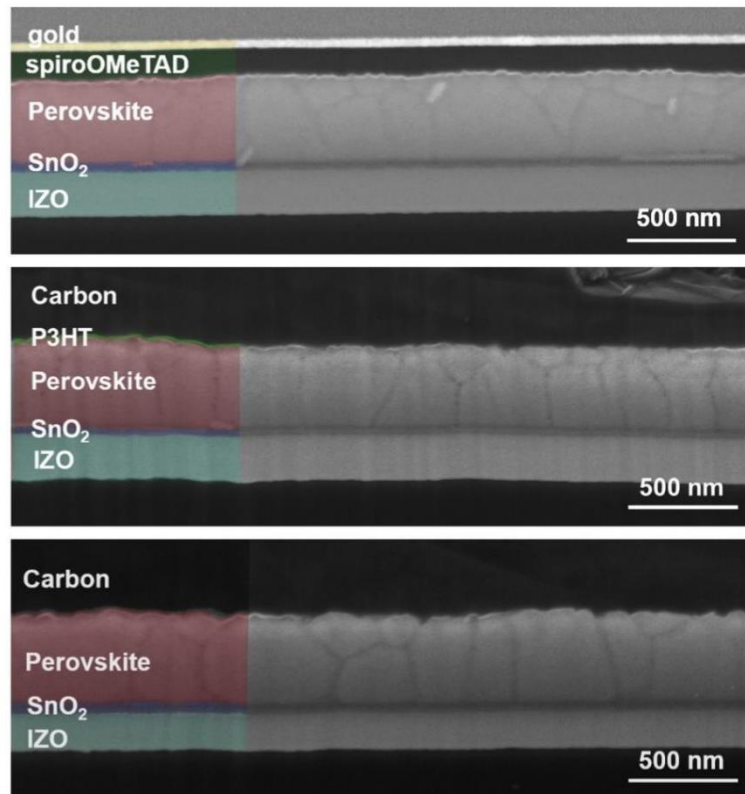


Figure 2 - SEM images of the cross-section of the three studied configurations: spiroOMeTAD+gold, P3HT+carbon and carbon.

The architecture chosen for obtaining a highly efficient and flexible low-light PSC was the following: Polyethylene terephthalate (PET) / Indium Zinc Oxide (IZO) / SnO₂ / perovskite / spiroOMeTAD / Gold. Since gold is rare and its deposition method - thermal evaporation under high vacuum - has a large energy and cost requirement, it is not attractive in terms of large-scale production. The current best alternative is using a carbon-based electrode, which is still highly conductive but cheaper and can be deposited by solution methods like blade coating and screen printing. Furthermore, devices with a carbon-based electrode still operate well without HTM, which simplifies the whole process and benefits mass production.¹⁰ Still, to maximize the oriented charge flow at this interface, a very thin layer (~8 nm) of a hole-extraction and electron-blocking material - P3HT - was introduced between the perovskite and the carbon layer. Figure 2 shows SEM cross-section images of these three configurations.

3.3.2. Photovoltaic performance

The current density-voltage (J-V) curves at reverse and forward scan, and the stabilized power output (SPO) of the best devices of each configuration are presented in Figure 3, along with the power conversion efficiency (PCE) at reverse scan of 30 devices at 1000 lux and 25 devices at 200 lux organized in box charts. The spectrum of the warm white LED (~3270 K) lamp used is presented in Figure 4. The photovoltaic parameters of the best devices of each variation are presented in Table 1. Complete box charts with the other photovoltaic parameters (voltage at open-circuit (V_{oc}), current density at short-circuit (J_{sc}), fill factor (FF) and power density) are presented in Figure 5. As expected, the metal electrode-based PSC is the most efficient, followed by the carbon-based electrode with an ultra-thin layer of P3HT, and the HTM-free carbon-based electrode PSC. Gold-based device presents a higher J_{sc} and FF , but interestingly slightly lower V_{oc} than carbon-based electrode devices. To understand the differences in the photovoltaic performance results and in the carrier recombination processes dominating the operation of each configuration, a thorough analysis was performed using a series of opto-electrochemical techniques. Since the substrate, ETM and perovskite layer were kept unchanged, the procedures were directed to the analysis of the interfaces and bulk of the HTM and back-contact.

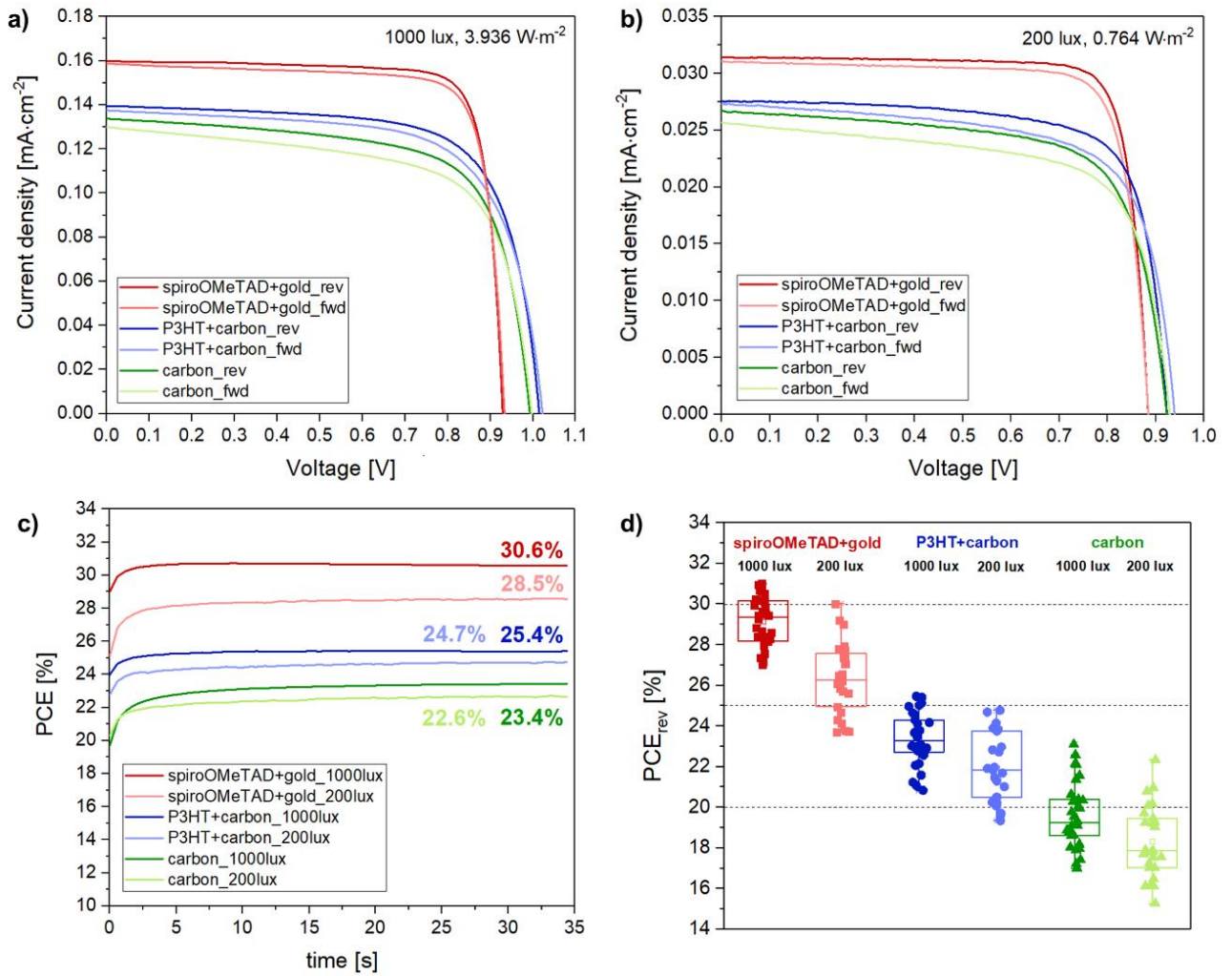


Figure 3 – a,b) *J-V* curves at reverse and forward scan, c) *SPO* and d) box charts of the PCE obtained at 1000 lux and 200 lux at reverse scan, for the three studied configurations: spiroOMeTAD+gold, P3HT+carbon and HTM-free carbon.

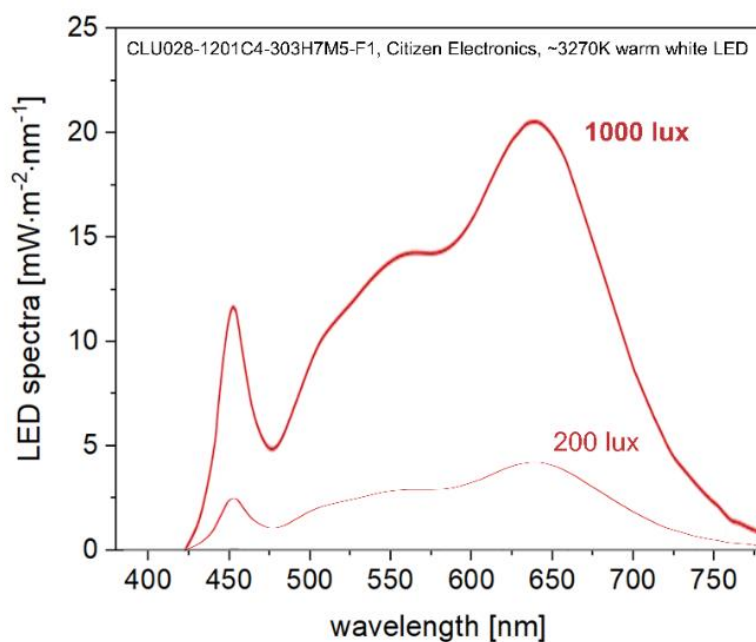


Figure 4 – Spectra at 1000 lux and 200 lux of the ~3270K warm white LED used for the photovoltaic performance measurements.

Table 1 – Photovoltaic parameters of the best devices at 1000 lux and 200 lux for the studied three configurations: spiroOMeTAD+gold, P3HT+carbon and HTM-free carbon.

	Max PCE [%]		SPO [%]	Power density [$\mu\text{W cm}^{-2}$]		FF [%]		V_{oc} [V]		J_{sc} [mA cm^{-2}]	
	rev	fwd		rev	fwd	rev	fwd	rev	fwd	rev	fwd
1000 lux											
spiroOMeTAD+gold	30.9	30.2	30.6	122	118.8	82.5	80.7	0.93	0.93	0.159	0.158
P3HT+carbon	25.4	24.3	25.4	100	95.6	70.9	68.2	1.01	1.02	0.140	0.138
carbon	23.1	21.8	23.4	91	85.7	68.8	66.1	0.99	1.00	0.134	0.130
200 lux											
spiroOMeTAD+gold	30.0	28.9	28.5	23	22.1	82.7	80.5	0.88	0.88	0.031	0.031
P3HT+carbon	24.7	23.0	24.7	19	17.6	74.5	68.8	0.92	0.93	0.028	0.027
carbon	22.3	21.1	22.6	17	16.1	69.5	67.6	0.92	0.93	0.026	0.026

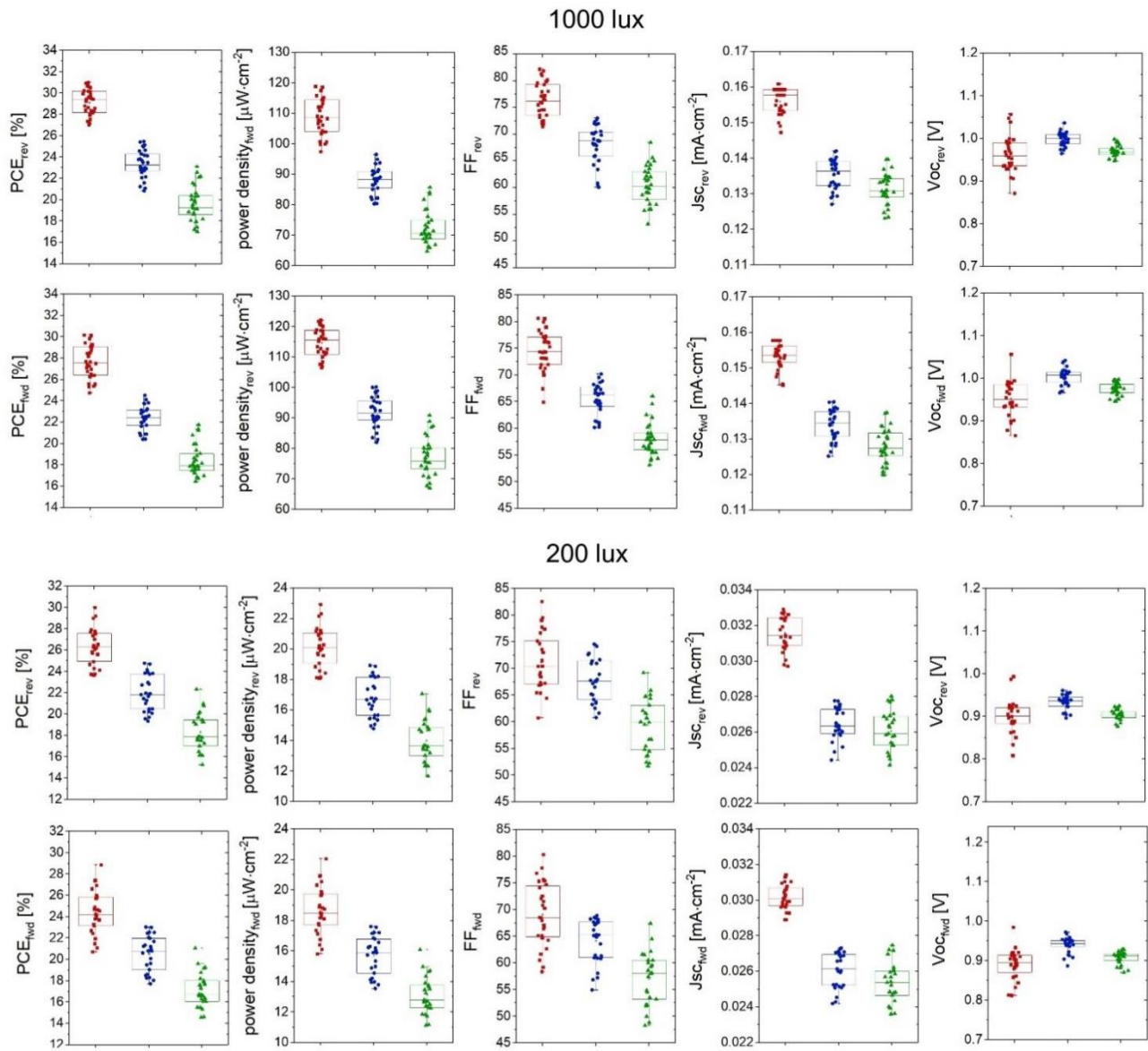


Figure 5 - Box charts of the photovoltaic parameters obtained at reverse and forward scan of the 30 devices at 1000 lux and 25 devices at 200 lux, for the three studied configurations: spiroOMeTAD+gold (red), P3HT+carbon (blue) and HTM-free carbon (green).

3.3.3. Device opto-electrochemical characterization

Quasi-fermi level splitting

To better understand the quality of the bulk and interfaces of the fabricated perovskite layer, a study based on the quasi-fermi level splitting and pseudo J - V measurements was made. Quasi-fermi level splitting (QFLS) represents the difference between the quasi-fermi level of electrons (in the conduction band) and the quasi-fermi level of holes (in the valence band) in a optical semiconductor under illumination. First, the absolute PL spectrum of the perovskite under different light intensities was measured. Then, this data was used to calculate the QFLS based on equation 1:¹¹

$$QFLS = V_{OC}^{rad} - kT \cdot \ln(PLQE) = V_{OC}^{rad} - kT \cdot \ln \left(\frac{\phi_{PL}}{\phi_{laser} \cdot A} \right) \quad (1)$$

where V_{OC}^{rad} is the radiative limit of V_{OC} , k is the Boltzman constant, T is the temperature, $PLQE$ is photoluminescence quantum efficiency, ϕ_{PL} is the absolute photon flux emitted by the perovskite by photoluminescence, ϕ_{laser} the absolute photon flux emitted by the laser, and A is the absorbance of the perovskite layer. QFLS values obtained at different light intensities – suns-QFLS (from 0.1 to 1000 $W\ m^{-2}$), together with the PLQE and V_{OC_rad} are presented in Table 2. While V_{OC}^{rad} indicates the maximum V_{OC} a solar cell with a 1.72 eV bandgap semiconductor would provide, the QFLS can be interpreted as the maximum V_{OC} a solar cell with the fabricated perovskite layer would provide (in case everything else is perfect). QFLS obtained for this perovskite varies between ~1.13 V at 10 $W\ m^{-2}$ and 1.34 V at 960 $W\ m^{-2}$, which corresponds to a loss on the radiative limit between 17 % and 7 %, respectively. The lower the light intensity, the larger the voltage drop, which was expected given the greater impact of the charge trap sites in the perovskite when a lower current is being generated. Still, at higher light intensities the voltage drop is reasonably small, demonstrating the low defect density and large efficiency potential of this perovskite absorber layer.

Table 2 – V_{OC_rad} , $PLQE$ and QFLS values obtained at different light intensities (suns-QFLS) for the fabricated perovskite $CS_{0.17}FA_{0.83}Pb(I_{0.7}Br_{0.3})_3$.

Light intensity [W m ⁻²]	V_{OC_rad} [V]	$PLQE$ [%]	QFLS [V]	Voltage drop [%]
10	1.320	0.06	1.128	17.0
17	1.333	0.13	1.161	14.8
60	1.366	0.35	1.221	11.9
120	1.384	0.60	1.253	10.5
280	1.406	0.99	1.288	9.2
480	1.420	1.45	1.311	8.3
780	1.432	2.13	1.333	7.4
960	1.438	2.46	1.343	7.1

Pseudo J-V curves

For the pseudo J-V analysis, the QFLS data is converted into a pseudo J-V curve according to the method described by Stolterfoht et al.¹² This method allows the calculation of the best J-V curve that the fabricated perovskite absorber layer can provide, *i.e.*, in case the bulk and surface recombination of the perovskite layer is the only limiting factor of the device. Similarly, the V_{OC} values for the three configurations were measured at different light intensities (suns- V_{OC}) and converted to a pseudo J-V curve. Since the suns- V_{OC} is performed under open circuit - no flow of charges - it excludes the charges transport losses (*i. e.*, the resistivity of electrodes and carrier charge mobility in the extraction layers), and thus represents the losses associated with non-radiative trap-assisted recombination happening mainly at the interfaces, similarly to the ideality factor. Figure 6a,b,c) shows the J-V and power curves measured at 1 sun, together with the pseudo J-V curves obtained with the suns- V_{OC} and suns-QFLS for each configuration. For each curve, the data was fitted with a diode equation to have a better estimate of the (pseudo-) FF.

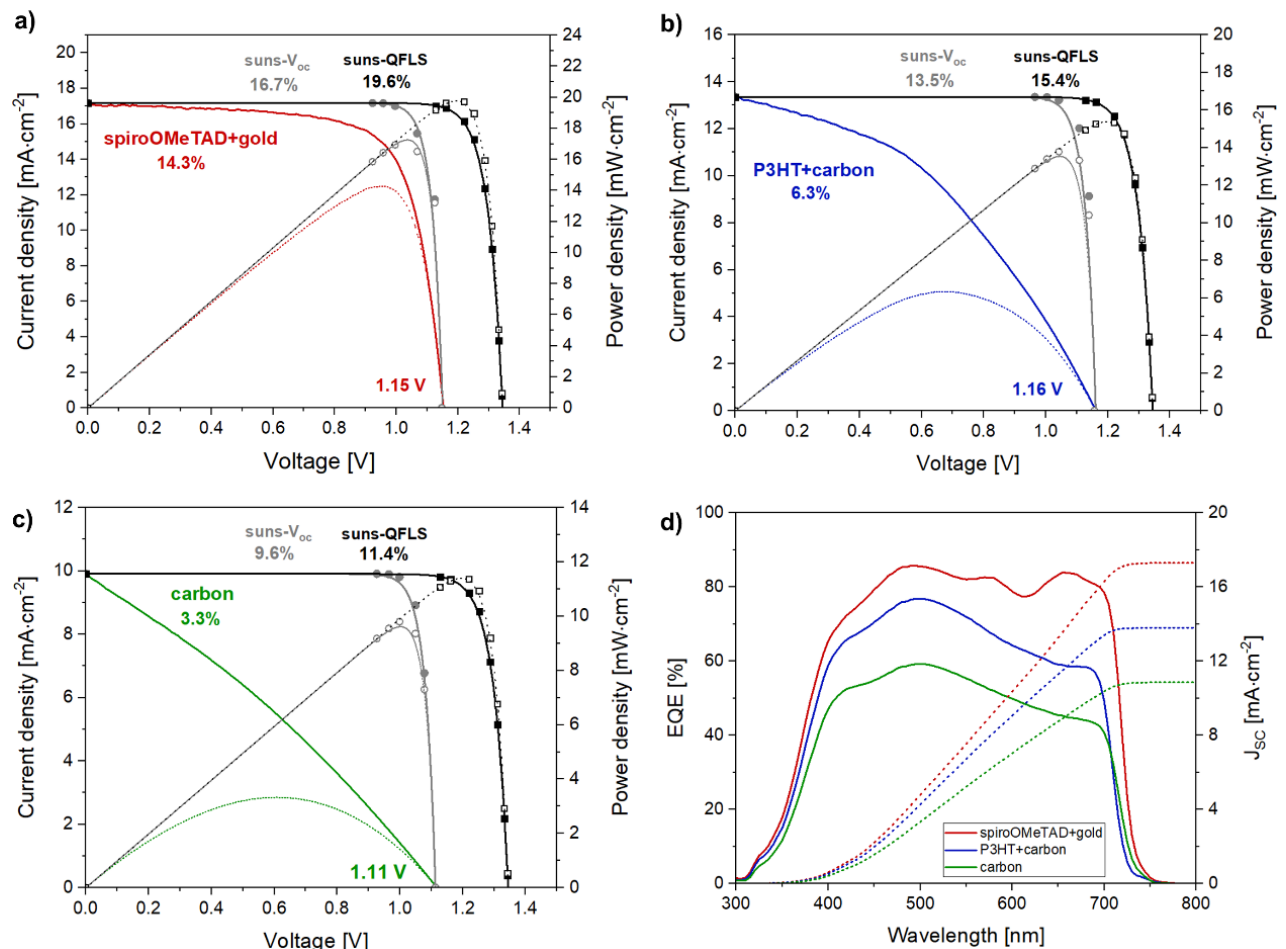


Figure 6. - Measured J-V curves at 1 sun and pseudo J-V based on Suns- V_{oc} and Suns-QFLS, for the three studied configurations: a) spiroOMeTAD+gold, b) P3HT+carbon and c) HTM-free carbon. d) EQE spectra and integrated JSC for four different configurations.

The pseudo-FF obtained by suns- V_{oc} is very high and virtually the same in every configuration (87 %), which suggests that the density of charge trap sites at the perovskite-HTM and HTM-electrode interfaces is not the dominant mechanism for efficiency loss in every configuration. On the other hand, there's a big voltage drop between the pseudo-JV curves: ~ 0.2 V for spiroOMeTAD+gold and P3HT+carbon device and ~ 0.25 V for carbon HTM-free device. A V_{oc} drop indicates either a high non-radiative defect density or energy mismatch. Given the high FF for the suns- V_{oc} pseudo-JV curve, this voltage drop is likely caused by an energy mismatch between the perovskite and the HTM or carbon layers. Indeed,

spiroOMeTAD and P3HT have a very close valence band maximum (*i.e.* highest occupied molecular orbital: -5.2 eV), and have similar voltage drops, and when no HTM is used (carbon HTM-free device), this voltage loss is higher. This energy mismatch (and voltage loss) could be reduced by engineering the extraction materials to either decrease the valence band maximum of the HTMs or increase the conduction band minimum (lowest unoccupied molecular orbital) of the ETM.

If considering the real JV curves, there is a major drop in the FF for the carbon-based electrode devices when compared with the pseudo-FF. This loss is likely caused by charge transport losses at the carbon bulk due to its lower conductivity (sheet resistance of the carbon layer is $15.9 \Omega \text{ sq}^{-1}$, while for the 50 nm of gold is $0.5 \Omega \text{ sq}^{-1}$), and at the perovskite-carbon interface due to the poor physical and electrochemical contact. This constrained charge extraction results in a charge accumulation at this interface, which will impact the charge flow in the whole device, affecting severely the FF and also compromising the net current produced by the device. By adding a layer of P3HT, the charge extraction efficacy at this interface is enhanced, resulting in an increased FF and J_{sc} . At low light the charge accumulation is less severe due to the lower density of photo-generated charge carriers flowing through the device, and the series resistances associated to the less conductive carbon layers has a much lower impact in the charge flow, which results in a smaller difference between the FF and J_{sc} of carbon and gold-based electrode devices - Figure 3. Actually, FF obtained at low-light, particularly for gold devices, is very high (>80 %), which demonstrates the very low density of trap sites (high shunt resistance) in the whole device.

Regarding the J_{sc} , the spiroOMeTAD+gold configuration presents the highest J_{sc} , followed by P3HT+carbon and finally HTM-free carbon. To study this behavior, external quantum efficiency (EQE) measurements were performed. EQE results - Figure 6d) - show clearly that the gold-based devices have higher absorption than the carbon-based electrode devices, specifically at higher wavelengths. This difference is caused by the better contact with the electrode, but is also partly caused by the mirroring effect of the gold layer. In short, the selected wide-band

gap perovskite absorbs better higher energy photons (with lower wavelengths), and, consequently, the lower energy photons will most likely not be so easily absorbed. However, if using an extremely smooth evaporated gold layer, these photons will be reflected, increasing the likelihood of absorption, which results in an increase in the generated current. An optical simulation of the fraction of light absorbed or reflected by a PSC with a carbon and metal back-contact was also performed, and the results agree with the EQE results - Figure 7.

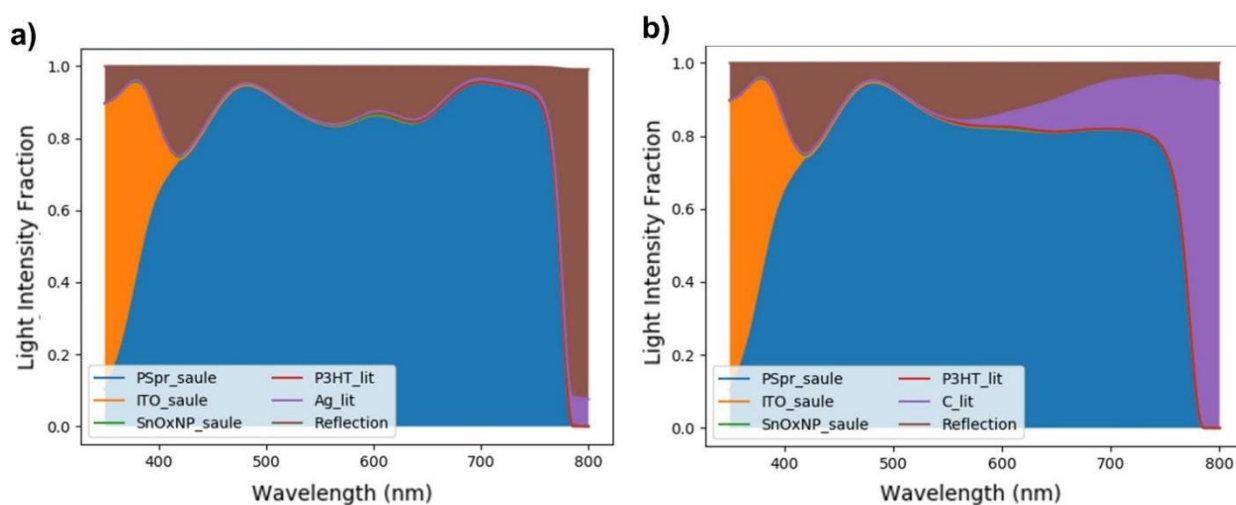


Figure 7 - Results of the simulation of the fraction of light absorbed or reflected obtained for a PSC with b) a metal and c) a carbon back-contact.

The J_{SC} values obtained by integrating the EQE spectra are also in agreement with the values obtained with the J-V-curves. The warm white LED lamp used for this study has one peak around 650 nm, which coincides with the peak of the reflected photons, which also explains the current density difference between gold and carbon-based electrode devices obtained at low-light - Figure 3.

In summary, perovskite layer presents a very high QFLS, indicating a high quality of its bulk and surface; all the perovskite interfaces (with SnO_2 , spiroOMeTAD, P3HT and carbon) are also very good, presenting a low number of charge trap sites (indicated by the high pseudo-FF extracted from suns- V_{OC}); the not-ideal energy alignment between the perovskite and extracting layers cause a voltage drop of ~ 0.2 V; the mirroring effect of the extremely smooth gold surface results in

a J_{SC} and FF increase both at 1 sun and low-light; the poor contact of the carbon-based electrode and its lower conductivity severely impacts the FF and J_{SC} at 1 sun; and adding a ultra-thin layer of P3HT enhances the charge extraction efficacy at the perovskite-carbon interface. If considering low-light conditions, the FF and J_{SC} drop caused by the charge accumulation at carbon-perovskite interface is significantly reduced.

Ideality factor

Ideality factor (n_{id}) is a parameter used to identify the type of recombination that limits the solar cell performance and its location within the device. This value is extrapolated from suns- V_{OC} plot, and it indicates how closely the diode follows the ideal diode equation. Additionally, this method is particularly interesting for low-light, since it permits the assessment of the PSC performance without the series resistance effect, i.e., only considers shunt resistances.¹³ The J-V-curves obtained at all light intensities for the three configurations are presented in Figure 8. The suns- V_{OC} plot is presented in Figure 9a) and was obtained by extracting the V_{OC} value of the obtained J-V curves at different light intensities.

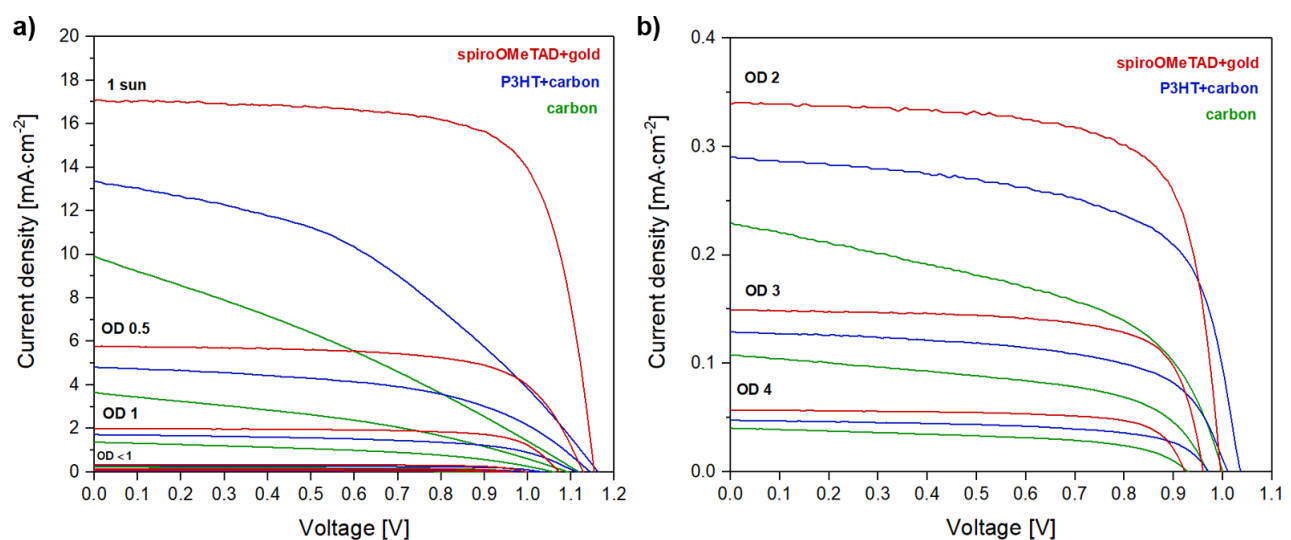


Figure 8 – J-V curves obtained at different light intensities (from 1000 to 0.1 W m⁻²) for the three studied configurations: spiroOMeTAD+gold, P3HT+carbon and HTM-free carbon.

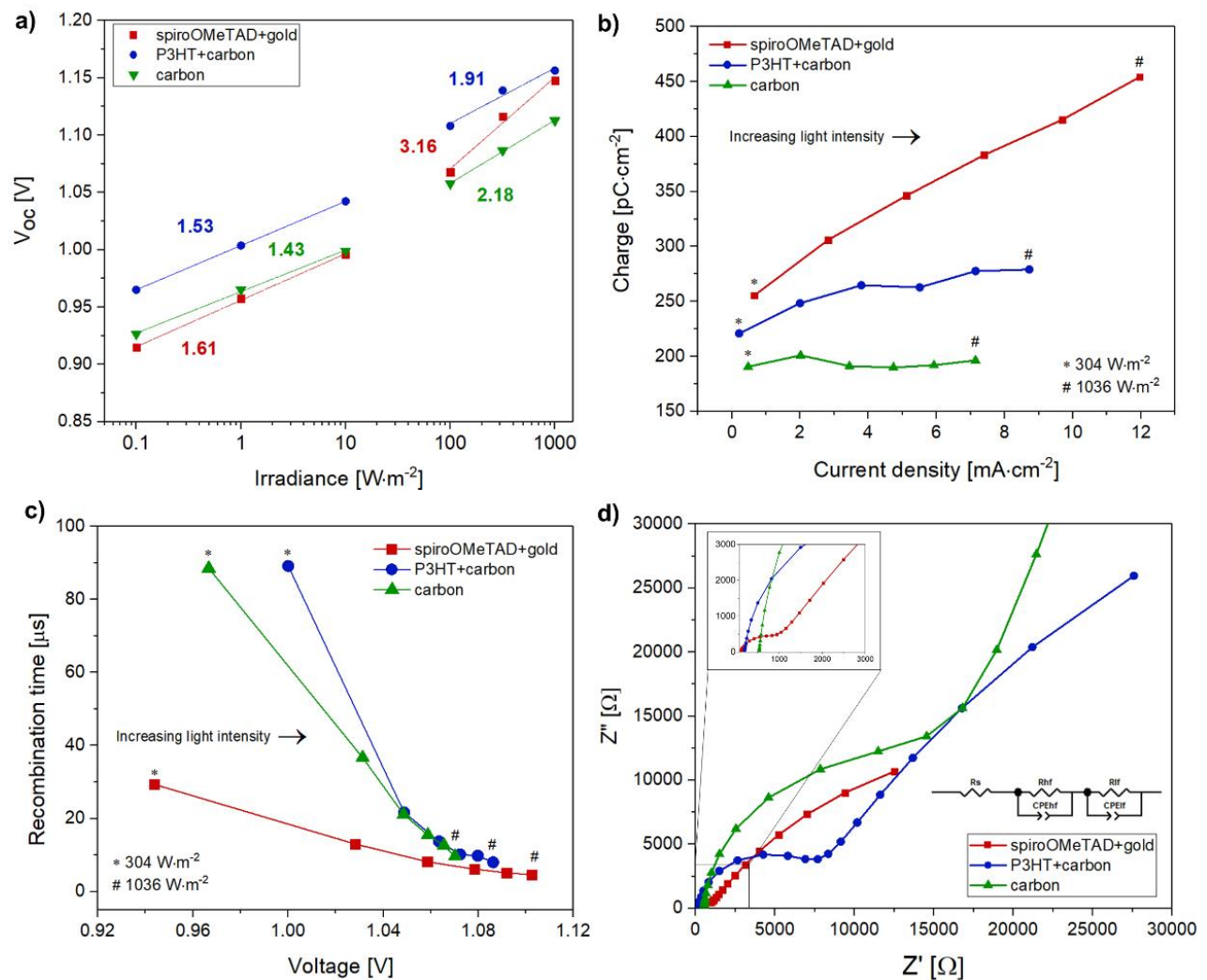


Figure 9 – a) suns- V_{oc} plot for light intensities from $0.1 W m^{-2}$ to $1000 W m^{-2}$, b) transient-photovoltage and c) photocurrent decay measurements for light intensities from $304 W m^{-2}$ to $1036 W m^{-2}$, and d) nyquist plots near V_{oc} in the dark for the three studied configurations: spiroOMeTAD+gold, P3HT+carbon, and HTM-free carbon.

The suns- V_{oc} method relies on the assumption that the photogenerated current density is proportional to the illumination intensity and the dominant recombination mechanism does not vary with illumination. In this case, measurements of the open-circuit voltage over a range of illumination intensities can be used to determine n_{id} via the equation

$$n_{id} = \frac{1}{V_T} \frac{d V_{oc}}{d \ln F_{ph}} = \frac{1}{kT/q} \frac{d V_{oc}}{d \ln F_{ph}} \quad (2)$$

where F_{ph} is the incident photon-flux density, V_T is the thermal voltage, and q is the elementary charge. Interestingly, all configurations present a trend for light intensities $\leq 10 \text{ W m}^{-2}$, and a different trend for light intensities $\geq 100 \text{ W m}^{-2}$, which is in disagreement with the assumption made for ideality factor analysis. Indeed, the high complexity level of the recombination mechanisms happening in a perovskite solar cell makes it difficult to use one single value to explain the phenomena of carrier charge extraction vs recombination, and imposes the adoption of a new analysis theory. Still, for lower light intensities, n_{id} for all configurations is around 1.5, but above 10 W m^{-2} , n_{id} increases for values close or even greater than 2. These observations demonstrate that there are different physical mechanisms controlling the behavior of PSCs under low- and high-intensity illumination.

At low-light intensities the first order non-radiative (monomolecular or Shockley–Read–Hall) recombination dominates the PSC operation, due to the reduced density of photo-generated charge carriers. In this type of recombination, a charge carrier is trapped in an energy level within the band gap of the material, mainly caused by defects in the crystal lattice, such as elemental vacancies, substitutions or interstitials at the perovskite bulk (mainly at grain boundaries), and dangling bonds (unbound electrons and holes) or impurities at the interfaces between the layers. However, since the perovskite and ETM layers are the same, the difference in n_{id} between the three configurations is correlated with first-order recombination happening mostly at the perovskite-HTM interface.¹⁴⁻¹⁶

Focusing only in the low-light range, spiroOMeTAD-gold configuration presents the highest n_{id} (1.6) followed by P3HT+carbon (1.5) and finally HTM-free carbon (1.4). Describing multiple parallel recombination processes occurring in a solar cell by a single parameter is a highly complex task, but it is often assumed that a n_{id} closer to 1 corresponds to a better performing device, dominated by bimolecular radiative recombination happening at the perovskite bulk (band-to-

band transition of an electron from the conduction band to the valence band resulting in an emission of a photon). However, according to Caprioglio *et al.*¹⁷, if using the same perovskite and ETM, a lower n_{id} (closer to 1) indicates a higher trap-assisted recombination at the perovskite-HTM interface, and correlates with a lower photovoltaic performance. Indeed, the HTM-free device presents the lowest n_{id} . This indicates that the spiroOMeTAD-perovskite interface is better than the P3HT-perovskite interface, resulting in a better charge extraction efficacy.

If considering high light-intensities, the n_{id} values obtained for carbon and spiroOMeTAD+gold configurations are out of the range predicted by the theory behind the classical Shockley diode equation. Actually, in literature values of n_{id} for PSC up to 5 can be found, which is correlated to the undesirable hysteresis effect often present in the J-V curves. This phenomenon makes the understanding of the fundamental physical mechanisms that control the behavior of PSCs difficult with classic theory and can mislead conclusions. Still, it is a fact that n_{id} varies due to a change in the dominant form of recombination, and an n_{id} increase indicates a strong second or even third order (non-radiative Auger) recombination.¹⁷ Indeed, both these types of recombination have a greater impact for higher light intensities (higher current density) given the higher probability of finding a hole and an electron at the same place.

Transient photocurrent decay

The better charge extraction efficiency of spiroOMeTAD+gold device was also validated by Transient Photocurrent Decay (TPC) measurements – Figure 9b). In this test, the PSC at short-circuit is excited by a short laser pulse, resulting in the generation of carriers that are extracted at the contacts. The density of photo-generated charges is then calculated by integrating the transient current over time. The gold-based device presents the highest current and charge extraction for a given light intensity (in accordance with the n_{id} and with the J_{SC} obtained from the J-V curves). Interestingly, the charge extraction of the devices with carbon-based electrode (particularly for the HTM-free device) keeps constant regardless the

increase in light intensity. As stated previously and in accordance with the FF obtained from the J-V curves at 1 sun, the poor carbon contact and its lower conductivity results in charge accumulation at this interface, limiting the charge extraction at this contact. Adding a P3HT layer enhances the carbon contact and the charge extraction efficiency.

Transient photovoltage decay

To have a better understanding on the recombination dynamics, the photogenerated charge lifetime of each configuration was also calculated using a similar technique - Transient Photovoltage Decay (TPV) measurements. In this case, a fast and small perturbation is applied to a solar cell, and since it is at open-circuit, the photo-generated carriers are forced to recombine, resulting in a voltage decay that can be used to calculate the carrier recombination time. Figure 9c) shows the time constant extracted from a single exponential fit of the voltage decay profiles calculated under different low-light intensities (from 304 W m^{-2} to 1036 W m^{-2}). Since the V_{OC} decay is proportional to the amount of carriers photo-generated by the laser pulse, the recombination time decreases with the increase in light intensity for all configurations.

Interestingly, for a given light intensity, spiroOMeTAD+gold configuration presented a smaller recombination time than the carbon-based electrode devices, specially at lower light intensities, which indicates a higher density of trap-sites located somewhere in the device. The results obtained by pseudo-FF, ideality factor, and TPC measurements indicated a superior perovskite-spiroOMeTAD interface; therefore, this higher capacitance might be caused by the presence of trap-sites on the spiroOMeTAD bulk, which could be originated from the presence of diffused gold atoms inside the spiroOMeTAD layer, by degraded dopants, or by the amorphous properties of spiroOMeTAD - the distance between molecules in the bulky tridimensional structure is large, resulting in a higher recombination rate.¹⁸ Since the band-gap of the perovskite remains unaltered for every configuration, the rate of the non-radiative recombination in the solar cell can be

directly related with the V_{OC} change. Thus, the lower V_{OC} of the spiroOMeTAD+gold device extracted from the J-V curves at low-light (1000 lux and 200 lux) - Figure 3 - was assigned to the higher recombination rate (lower recombination time) of the spiroOMeTAD+gold device.

Electrochemical Impedance spectroscopy

Another advanced optoelectronic technique relevant for this study is the Electrochemical Impedance spectroscopy (EIS) - it provides important information such as the transport rates, recombination losses, interfacial charge accumulation processes, characteristic geometric capacitances and ionic diffusion coefficients occurring in different time domains.¹⁹ Figure 9d) shows the Nyquist plots of the three different configurations at V_{OC} in the dark. The interfacial charge transfer and bulk transport resistance in the high (10^3 – 10^5 Hz) and low (1 - 10^3 Hz) frequency regions were modelled by a parallel combination of a constant phase element (CPE) and a resistor element (R), depicted in the inset of Figure 9d), in which the subscript s is series and hf and lf is high and low frequencies, respectively. The obtained resistances at high (1st semi-circle) and low (2nd semi-circle) frequencies, as well as the CPE values are presented in table 3.

The trap-assisted recombination responsible for the different performances of the studied devices occurs at a timescale between 1 and 100 μ s (as depicted in the TPV plot), responding therefore at high frequencies. The series resistance (R_s) value is also relevant for this study since it is related with the parasitic resistances at the charge extraction contacts.²⁰ Both R_s and R_{hf} are higher for HTM-free carbon, followed by carbon with P3HT and finally gold, which indicates a higher dissipation of electrical energy for the carbon-based electrode devices, and is related with the lower FF of the carbon devices both at 1 sun and low-light (poorer carbon contact and higher sheet resistance of carbon comparing with gold). However, CPE_{hf} is higher for the spiroOMeTAD+gold device, indicating a higher charge storage capacity, which is most likely caused by the diffused gold atoms and amorphous properties of spiroOMeTAD, as stated previously.

Table 3 – Resistance and constant phase element values obtained by fitting results in the assumed model, for the three studied configurations: spiroOMeTAD+gold, P3HT+carbon, and HTM-free carbon.

configuration	R_s [Ω]	R_{hf} [Ω]	R_{lf} [Ω]	CPE_{hf} [F]	CPE_{lf} [F]
spiroOMeTAD+gold	96.96	773.8	43517	3.36×10^{-7}	1.03×10^{-5}
P3HT+carbon	187.8	6627	1.29×10^5	8.63×10^{-8}	4.97×10^{-6}
carbon	528.7	14350	1.94×10^6	7.82×10^{-8}	7.53×10^{-7}

3.3.4. Stability tests

Maximum Power Point Tracking

Operational stability of the three configurations was assessed by maximum power point tracking (MPPT) at 35-40 °C under a LED-lamp with an irradiance of 600 W m^{-2} (0.6 suns) inside the nitrogen-filled glove box. The values for the normalized and absolute current, voltage and power at MPP are presented in Figure 11. The HTM-free device with carbon-based electrode demonstrated to be the most stable, keeping about 84 % of its initial power density after 1000 h. Impressively, the voltage at the MPP (V_{MPP}) of this device was virtually unchanged after 1000 h. It is important to note that these devices are designed for low-light operation, in which irradiance is about 150 times lower than the one used at the MPPT experiment. Adding P3HT to enhance the charge extraction resulted in a poorer operational stability – device lost 41 % of its initial power density after 1000 h. This loss was mainly caused by a loss in V_{MPP} . The device with spiroOMeTAD and gold experienced a large drop in both V_{MPP} and J_{MPP} , consequently, after 300 h the device was producing only about 23 % of its initial power density. The perovskite degradation is visible in the spiroOMeTAD+gold and P3HT+carbon devices (near the electrode's edges), but not in the HTM-free carbon - Figure 10.

Since spiroOMeTAD easily allows ionic diffusion, it is a very weak barrier for gold migration towards the device's inner layers, even at room temperature.²¹

Therefore, the power density drop of the gold device after only 300 h at MPPT could be justified by the diffusion of gold atoms towards the device's inner layers, which was boosted by the temperature that the MPPT was performed. This higher temperature might also have boosted the degradation of the doped spiroOMeTAD.

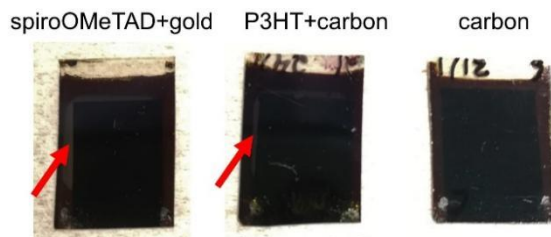


Figure 10 – Picture of the three configurations after the MPPT aging test.

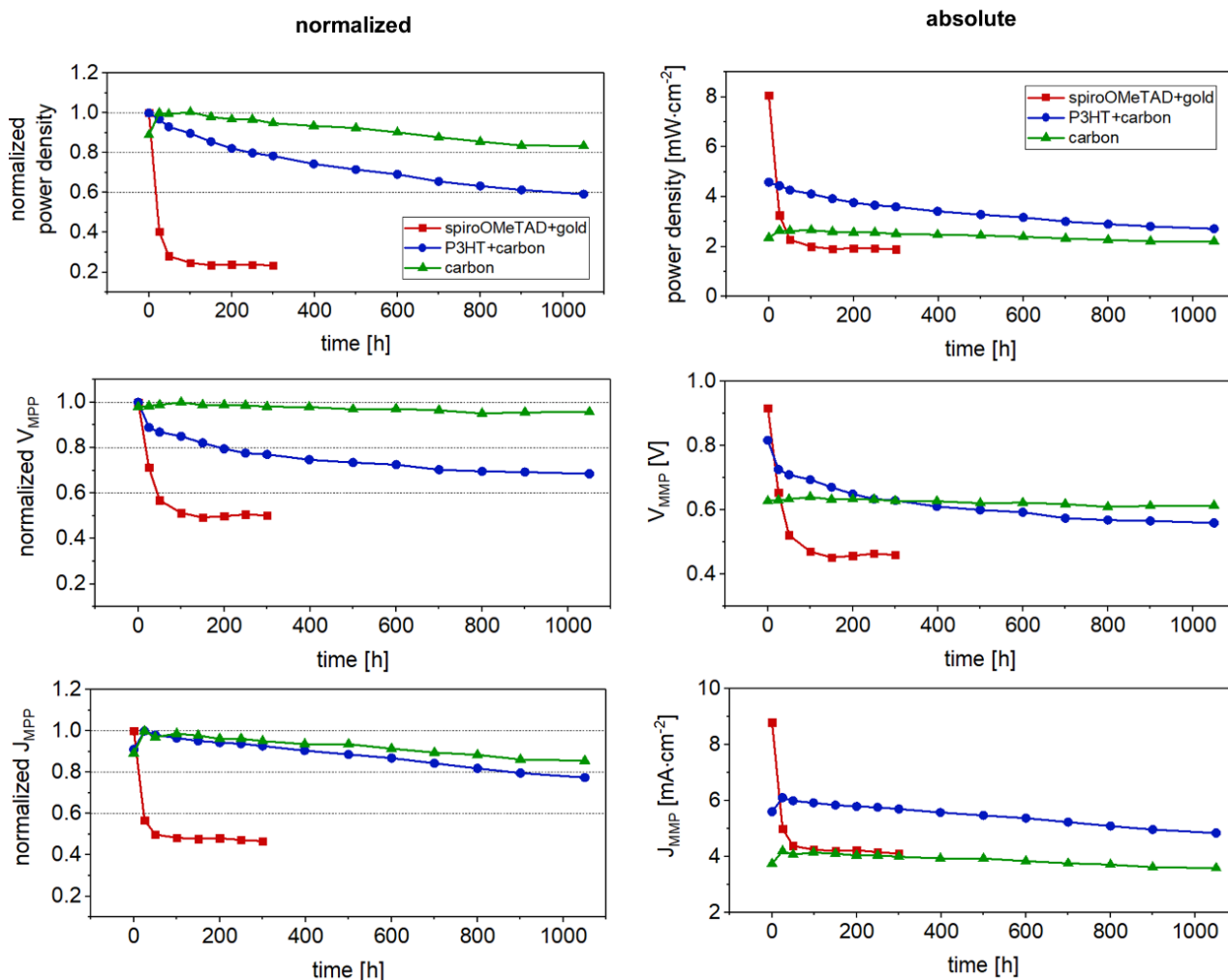


Figure 11 – Normalized and absolute values for the power density, current and voltage at MPPT at ~ 0.6 suns for over 1000 h for the three studied configurations.

Thermal and moisture stability

HTM-free carbon-based electrode configuration also presented a high thermal stability, keeping virtually the same photovoltaic performance after 1000 h at 85 °C. Again, adding P3HT compromised the stability of the device, with a loss of almost 0.1 V in V_{oc} after 1000 h at 85 °C, which resulted in a total loss in efficiency of about 16 %. Impressively, the gold-based device with spiroOMeTAD kept 87 % of its performance after the thermal test, despite the visual degradation of spiroOMeTAD and gold. The J-V curves at reverse and forward scan at the beginning and by the end of the thermal test is shown in Figure 12a,b,c). Some non-encapsulated devices were also left under ambient atmosphere (30 % relative humidity) for 1600 h, and there was virtually no change in efficiency - Figure 12d). In conclusion, after analyzing the operational and environmental stability of the three configurations keeping the same wide band-gap perovskite, it can be concluded that the limiting degradation process is the light-induced phase segregation, rather than temperature and moisture. Adding P3HT enhances the charge extraction but compromises both the thermal and operational stability.

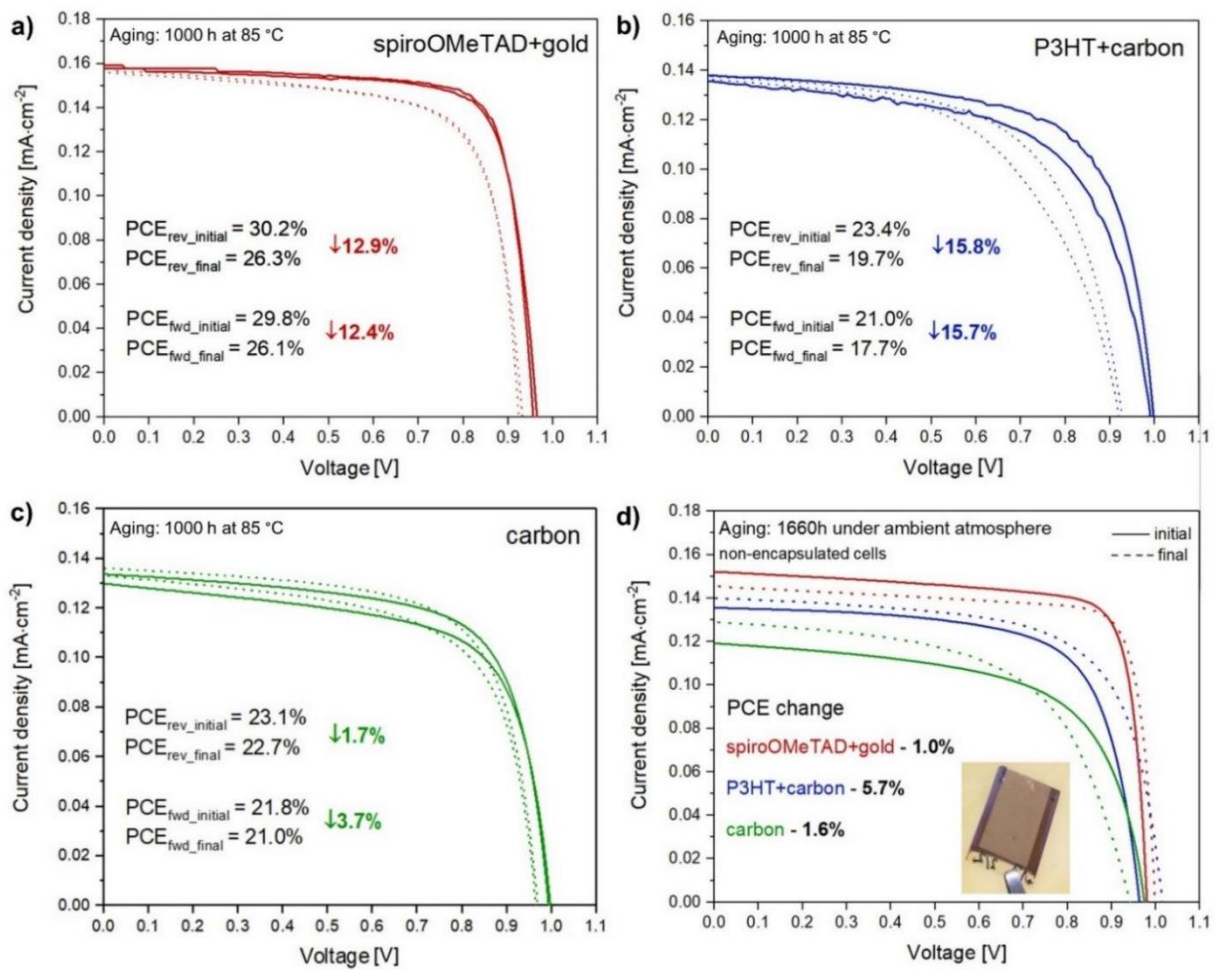


Figure 12 – J-V curves at reverse and forward scan under 1000 lux of non-encapsulated cells of the three configurations, before and after aging tests: a.b.c) 1000 h at 85 °C inside N₂ filled glovebox; d) 1600 h under air atmosphere (inset corresponds to a picture of the spiroOMeTAD+gold device after the thermal test).

Bending test

One of the main features of using a plastic substrate is the possibility of bending the solar device to fit the final application. However, the large deformation that the device is exposed to can damage the brittle electrode materials, lead to interfacial residual stress and lattice mismatch, affecting the charge transport and the device's performance.²² To test the stability of the fabricated devices to repetitive mechanical deformation, samples were bent 800 times, using a radius of 2 cm. The evolution of PCE (absolute and normalized) as a function of bending (cycles/time) is presented in Figure 13a,b). The J-V-curves before and after the test along with pictures of the test are presented in Figure 13c). For all configurations the main impact occurs during the first 100 bending cycles. From then onwards the change is not that significant. For the carbon devices with and without P3HT, PCE decreased by 13 % and 18 %, respectively. These results indicate an inferior mechanical adhesion of carbon to the perovskite surface (that is improved by adding a P3HT layer), which results in a gradual delamination of the carbon layer and consequently compromises the charge extraction at this electrode. Regarding to the device with gold electrode, the PCE actually increases up to 11 % after the first 200 bending cycles, followed by a slow decrease in PCE, finishing the test with 108 % of its initial PCE. In this case, the metal ductility might have allowed the enhancement of the interfacial contact with the underlying layer at the first stage of the test, followed by a gradual delamination of the metal layer.

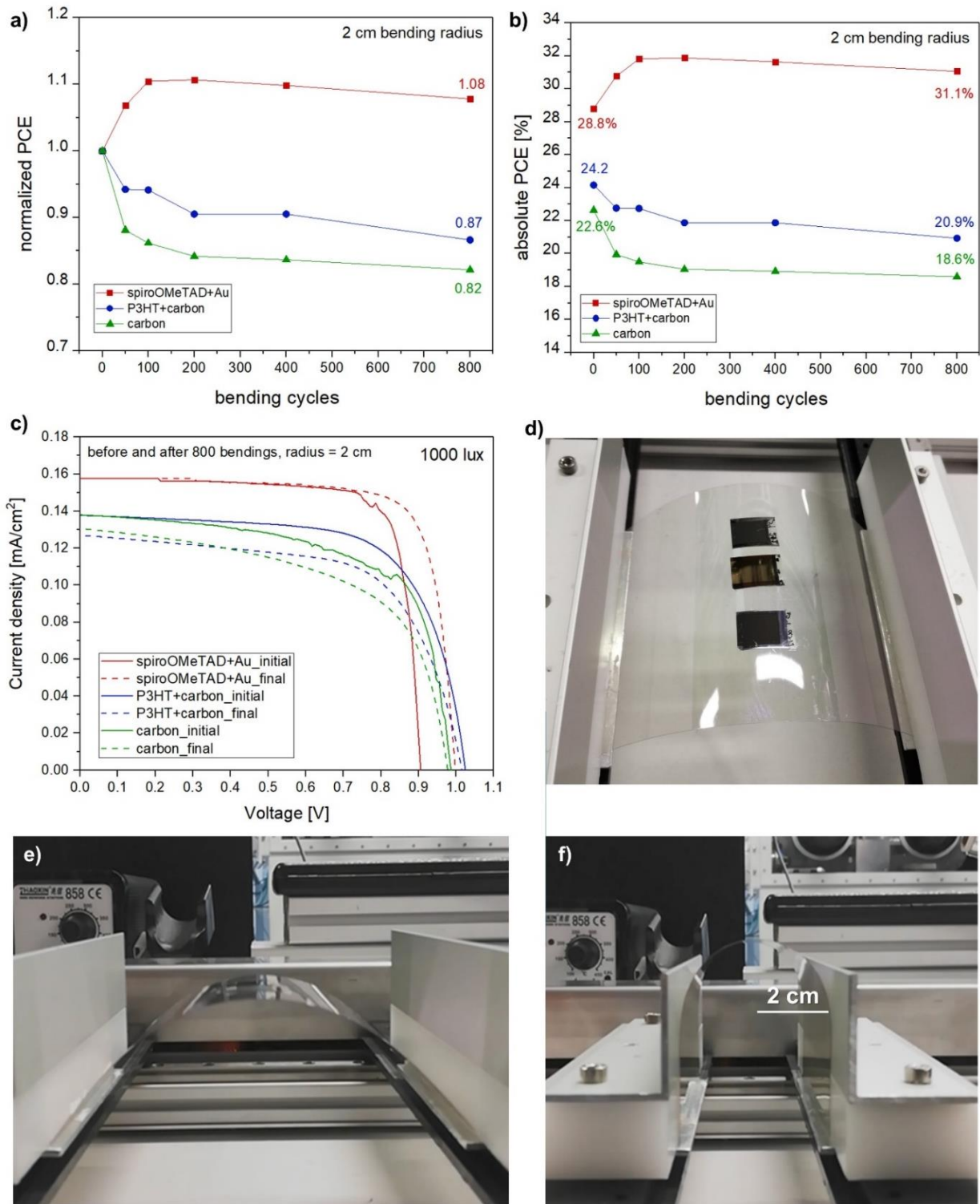


Figure 13 – Evolution of the a) normalized and b) absolute PCE during the bending test and c) the respective J-V-curves before and after 800 bending cycles with a radius of 2 cm. Pictures of the d) assembled samples, e) minimum bending and f) maximum bending.

3.4. Conclusion

In this chapter, a perovskite solar cell was designed and optimized for artificial low-light operation. A maximum efficiency (power density) of 30.9 % ($122 \mu\text{W cm}^{-2}$) at 1000 lux for a device with a metal electrode, and 25.4 % ($100 \mu\text{W cm}^{-2}$) and 23.1 % ($91 \mu\text{W cm}^{-2}$) for a device with a carbon-based electrode, was obtained with and without HTM, respectively. The selected lamp was a warm white LED ($\sim 3270 \text{ K}$). The high quality of the fabricated perovskite layer was validated with a calibrated photoluminescence mapping. The pseudo J-V curves indicated that the perovskite interfaces have reduced charge trap sites; that the carbon contact is deficient, resulting in a decrease in FF and J_{SC} ; and that the charge extraction efficiency at this interface is improved when an ultra-thin layer of P3HT is added. The EQE results suggested that the mirroring effect of gold results in an increase of J_{SC} both at low-light and 1 sun. Suns- V_{OC} (ideality factor) and TPC results revealed a superior perovskite-spiroOMeTAD interface, which is related with its better charge extraction. However, this configuration also presented the highest capacitance and recombination rate (indicted by the EIS and TPV, respectively) which might be the cause of the lower V_{OC} at artificial low-light, when compared with carbon-based electrode devices. Regarding stability, carbon-based electrode devices performed better than the device with gold – while gold-based device kept 23 % of their initial efficiency after 300 h at MPPT, carbon-based electrode devices with and without P3HT kept 59 % and 84 % after 1000 h, respectively. HTM-free carbon-based electrode devices also presented a very high thermal stability, keeping virtually the same performance after 1000 h at $85 \text{ }^\circ\text{C}$.

Acknowledgements

Cristina Teixeira and Dávid Forgács acknowledge funding from the European Regional Development funds provided by the National Centre of Research and Development (NCBR) under POIR.01.01.01-00-1482/19-00. P.S and K.W acknowledge funding from the National Science Centre (Poland) for the NCN Opus grant no. UMO-2016/23/B/ST5/02861. L.A.C. and A.D.C. acknowledge funding from the Italian Ministry of Economic Development in the framework of the Operating Agreement with ENEA for Research on the Electric System. D.M and U.W. acknowledge the funding from the German Federal Ministry for Economic Affairs and Energy (FKz. 03EE1007—Organaut). Cluster of Excellence livMatS: Funded by the Deutsche Forschungsgemeinschaft (DFG, German Research Foundation) under Germany's Excellence Strategy—EXC-2193/1—390951807. L.A. and A.M. acknowledges Project SolarPerovskite PTDC/EQU-EQU/28966/2017 - NORTE-01-0145-FEDER-028966 - funded by FEDER funds through Programa Operacional Regional do Norte (NORTE 2020) and by national funds (PIDDAC) through FCT/MCTES and LA/P/0045/2020 (ALiCE), UIDB/00511/2020 and UIDP/00511/2020 (LEPABE), funded by national funds through FCT/MCTES (PIDDAC). The authors also acknowledge the support of Dr. Mateusz Ścigaj in the bending tests, of Dra. Rosinda Fuentes Pineda in the experimental procedure development, and the support of Eng. Maciej Bizan in the stability tests.

References

1. Bati, A. S. R.; Zhong, Y. L.; Burn, P. L.; Nazeeruddin, M. K.; Shaw, P. E.; Batmunkh, M., Next-generation applications for integrated perovskite solar cells. *Communications Materials* **2023**, *4* (1), 2.
2. Hasan, M. State of IoT 2022: Number of connected IoT devices growing 18% to 14.4 billion globally *IoT Analytics* [Online], 2022. <https://iot-analytics.com/number-connected-iot-devices/>.
3. Park, J.; Kim, J.; Yun, H.-S.; Paik, M. J.; Noh, E.; Mun, H. J.; Kim, M. G.; Shin, T. J.; Seok, S. I., Controlled growth of perovskite layers with volatile alkylammonium chlorides. *Nature* **2023**.
4. Chen, C.-H.; Su, Z.-H.; Lou, Y.-H.; Yu, Y.-J.; Wang, K.-L.; Liu, G.-L.; Shi, Y.-R.; Chen, J.; Cao, J.-J.; Zhang, L.; Gao, X.-Y.; Wang, Z.-K., Full-Dimensional Grain Boundary Stress Release for Flexible Perovskite Indoor Photovoltaics. *Advanced Materials* **2022**, *34* (16), 2200320.
5. Liang, X.; Ge, C.; Fang, Q.; Deng, W.; Dey, S.; Lin, H.; Zhang, Y.; Zhang, X.; Zhu, Q.; Hu, H., Flexible Perovskite Solar Cells: Progress and Prospects. *Frontiers in Materials* **2021**, *8*.
6. Hin Lee, H. K.; Barbé, J.; Tsoi, W. C., Chapter Ten - Organic and perovskite photovoltaics for indoor applications. In *Solar Cells and Light Management*, Enrichi, F.; Righini, G. C., Eds. Elsevier: 2020; pp 355-388.
7. Jagadamma, L. K.; Wang, S., Wide-Bandgap Halide Perovskites for Indoor Photovoltaics. *Frontiers in Chemistry* **2021**, *9*.
8. Knight, A. J.; Borchert, J.; Oliver, R. D. J.; Patel, J. B.; Radaelli, P. G.; Snaith, H. J.; Johnston, M. B.; Herz, L. M., Halide Segregation in Mixed-Halide Perovskites: Influence of A-Site Cations. *ACS Energy Letters* **2021**, *6* (2), 799-808.
9. Prathapani, S.; Bhargava, P.; Mallick, S., Electronic band structure and carrier concentration of formamidinium–cesium mixed cation lead mixed halide hybrid perovskites. *Applied Physics Letters* **2018**, *112* (9).
10. Babu, V.; Fuentes Pineda, R.; Ahmad, T.; Alvarez, A. O.; Castriotta, L. A.; Di Carlo, A.; Fabregat-Santiago, F.; Wojciechowski, K., Improved Stability of Inverted and Flexible Perovskite Solar Cells with Carbon Electrode. *ACS Applied Energy Materials* **2020**, *3* (6), 5126-5134.
11. Caprioglio, P.; Stolterfoht, M.; Wolff, C. M.; Unold, T.; Rech, B.; Albrecht, S.; Neher, D., On the Relation between the Open-Circuit Voltage and Quasi-Fermi Level Splitting in Efficient Perovskite Solar Cells. *Advanced Energy Materials* **2019**, *9* (33), 1901631.
12. Stolterfoht, M.; Grischek, M.; Caprioglio, P.; Wolff, C. M.; Gutierrez-Partida, E.; Peña-Camargo, F.; Rothhardt, D.; Zhang, S.; Raoufi, M.; Wolansky, J.; Abdi-Jalebi, M.; Stranks, S. D.; Albrecht, S.; Kirchartz, T.; Neher, D., How To Quantify the Efficiency Potential of Neat Perovskite Films: Perovskite Semiconductors with an Implied Efficiency Exceeding 28%. *Advanced Materials* **2020**, *32* (17), 2000080.
13. Ortega, P. R.; Piñol, J. M.; Martín, I.; Orpella, A.; Masmitjà, G.; López, G.; Ros, E.; Voz, C.; Puigdollers, J.; Alcubilla, R., Low-Cost High-Sensitive Sun-

- formula> V_{oc} </tex-math></inline-formula> Measurement Instrument to Characterize c-Si Solar Cells. *IEEE Transactions on Instrumentation and Measurement* **2020**, 69 (9), 6429-6435.
14. Davies, C. L.; Filip, M. R.; Patel, J. B.; Crothers, T. W.; Verdi, C.; Wright, A. D.; Milot, R. L.; Giustino, F.; Johnston, M. B.; Herz, L. M., Bimolecular recombination in methylammonium lead triiodide perovskite is an inverse absorption process. *Nature Communications* **2018**, 9 (1), 293.
 15. Courtier, N. E., Interpreting Ideality Factors for Planar Perovskite Solar Cells: Ectypal Diode Theory for Steady-State Operation. *Physical Review Applied* **2020**, 14 (2), 024031.
 16. Ryu, S.; Nguyen, D. C.; Ha, N. Y.; Park, H. J.; Ahn, Y. H.; Park, J.-Y.; Lee, S., Light Intensity-dependent Variation in Defect Contributions to Charge Transport and Recombination in a Planar MAPbI₃ Perovskite Solar Cell. *Scientific Reports* **2019**, 9 (1), 19846.
 17. Caprioglio, P.; Wolff, C. M.; Sandberg, O. J.; Armin, A.; Rech, B.; Albrecht, S.; Neher, D.; Stolterfoht, M., On the Origin of the Ideality Factor in Perovskite Solar Cells. *Advanced Energy Materials* **2020**, 10 (27), 2000502.
 18. Ren, G.; Han, W.; Deng, Y.; Wu, W.; Li, Z.; Guo, J.; Bao, H.; Liu, C.; Guo, W., Strategies of modifying spiro-OMeTAD materials for perovskite solar cells: a review. *Journal of Materials Chemistry A* **2021**, 9 (8), 4589-4625.
 19. Contreras-Bernal, L.; Ramos-Terrón, S.; Riquelme, A.; Boix, P. P.; Idígoras, J.; Mora-Seró, I.; Anta, J. A., Impedance analysis of perovskite solar cells: a case study. *Journal of Materials Chemistry A* **2019**, 7 (19), 12191-12200.
 20. von Hauff, E.; Klotz, D., Impedance spectroscopy for perovskite solar cells: characterisation, analysis, and diagnosis. *Journal of Materials Chemistry C* **2022**, 10 (2), 742-761.
 21. Rombach, F. M.; Haque, S. A.; Macdonald, T. J., Lessons learned from spiro-OMeTAD and PTAA in perovskite solar cells. *Energy & Environmental Science* **2021**, 14 (10), 5161-5190.
 22. Zheng, Z.; Li, F.; Gong, J.; Ma, Y.; Gu, J.; Liu, X.; Chen, S.; Liu, M., Pre-Buried Additive for Cross-Layer Modification in Flexible Perovskite Solar Cells with Efficiency Exceeding 22%. *Advanced Materials* **2022**, 34 (21), 2109879.

CHAPTER 4

FABRICATION OF A FLEXIBLE PEROVSKITE SOLAR CELL BY SLOT-DIE COATING IN AMBIENT CONDITIONS

Adapted from the peer-reviewed article:

Manufacturing optimization of a flexible Perovskite Solar Cell for indoor applications by slot-die coating in ambient conditions

Cristina Teixeira, Rosinda Fuentes-Pineda, Luísa Andrade, Adélio Mendes, Dávid Forgács; accepted by Materials Advances, in July 2023.

FABRICATION OF A FLEXIBLE PEROVSKITE SOLAR CELL BY SLOT-DIE COATING IN AMBIENT CONDITIONS

4.1. Introduction

In the previous chapter it was optimized a procedure to fabricate a highly efficient and stable PSC on a flexible substrate for low-light indoor applications. Still, if the goal is moving towards perovskite devices industrialization, designing a stable device (materials and architecture), and developing a manufacturing process compatible with mass production is just as important as continuing to increase its efficiency. Ideally, the manufacturing process of the whole photovoltaic stack should be done under an ambient atmosphere, using scalable and low-energy consumption techniques (i.e. low temperature and no requirement for high vacuum). Several large-scale solution-based deposition methods have already been developed, such as blade-coating, spray coating, slot-die coating and inkjet printing.¹ However, one-step slot-die coating is currently the most promising one, given its straightforward integration into a roll-to-roll (R2R) system (which enables a high-throughput production capability), and the high photovoltaic performances already attained using this technique.² In 2023, Jinzhao et al. reported an astonishing 22.3 % efficiency in a 0.2 cm² cell under 1 sun using a metal electrode and rigid substrate. Furthermore, encapsulated devices withstood more than 1 year under continuous maximum power point tracking (MPPT) in outdoor real conditions, with virtually no decrease in efficiency.³ If considering only flexible substrate and processing under ambient atmosphere, moderately high efficiencies

are still possible: in 2020 Watson's group reported a 13.4 % efficiency for a n-i-p PSC with slot-die coated extraction layers and perovskite, and evaporated electrode;⁴ and in 2023 the same group reported 9.7 % of efficiency for a fully slot-die coated device with carbon-based electrode.⁵ Also, the latter devices kept ~85 % of their initial efficiency after 1000 h under 70 % relative humidity with no encapsulation.⁵ However, there is currently no available data on the efficiency of flexible PSC deposited exclusively by scalable deposition methods under indoor lighting conditions.

Here, we report the design and development of an experimental procedure to fabricate flexible low-cost PSC based on slot-die coating focusing on mass production. The device architecture and the materials were selected to minimize the number of fabrication steps (depositions and treatments), minimize energy consumption (low temperature and no need for high-vacuum) and maximize the stability of the device, without significantly compromising its PCE. The chosen architecture was a 4-layered n-i planar device with metal oxide electron transport material - SnO₂, mixed-halide 3D perovskite - (FAPbI₃)_{0.85}(MAPbBr₃)_{0.15}, 2D perovskite capping/passivation layer - n-octylammonium iodide (OAI), and carbon-based electrode (deposited by blade-coating) - Figure 3.

The solvent system of each material was carefully selected aiming for low viscosity, high volatility and appropriate polarity (for obtaining a stable solution with uniform and fine particle size distribution, and a good adhesion with the underlying surface). The coating window of each material was determined using the viscocapillary model for slot-die coating technique and the measured rheological data. According to the low flow limit plot, all solutions form a stable meniscus at the specified speed of 1 m min⁻¹, which is a speed that enables industrially relevant production throughput. The optimized manufacturing process produces a PSC with a maximum PCE of 18.6 % under 1000 lux (372 μW cm⁻²; 0.64 cm² active area). The PSC with bare 3D perovskite kept 96 % of its initial efficiency after 550 h under MPPT under 0.25 sun. Overall, this work demonstrates a successful process transfer from small-scale techniques into large-scale production.

4.2. Experimental Section

4.2.1. Materials and experimental procedure

Materials

All materials were used as received without further purification. The reactants used were: lead iodide, PbI_2 (Sigma-Aldrich, 99.9 %), lead bromide, PbBr_2 (Sigma-Aldrich, 98 %), formamidinium iodide, FAI (Dyename, 99.99 %), methylammonium bromide, MABr (Sigma-Aldrich, ≥ 99 %), n-octylammonium iodide, OAI (Greatcell Solar, >99 %), acetonitrile, ACN (Sigma-Aldrich, anhydrous 99.8 %), 2-methoxyethanol, 2-ME (Sigma-Aldrich, anhydrous 99.8 %), dimethyl sulfoxide, DMSO (Sigma-Aldrich, anhydrous ≥ 99 %), 2-propanol, IPA (Sigma-Aldrich, anhydrous 99.5 %), tin (IV) oxide, SnO_2 (Alfa Aesar, 15 % in H_2O colloidal dispersion), carbon paste (DN-CP01 from Dyename).

Substrate

The substrate consisted of a 125 μm thick PET foil covered with a layer of ~ 100 nm thick ITO (Eastman, $60 \Omega\text{sq}^{-1}$), with a size of 12 cm x 30 cm. The PET/ITO substrates were patterned (P1) using NIR laser (Rofin PowerLine E Air 25). The substrates were then cleaned twice with IPA and blow-dried with nitrogen (N_2).

Slot-die coater

SnO_2 , perovskite and OAI layers were deposited using the film applicator from Erichsen (COATMASTER 510 XL), air-knife from NEX FLOW, and slot-die coating head (SC100) and syringe pump from SCIPRIOS GmbH. The slot-die attachment part, the shims (inox), and the accessories to change the flow direction of the air-knife (polymer based) were developed in-house. In this set-up, the substrate is fixed onto the applicator bed while the slot-die head and air-knife move throughout the whole length of the substrate. After coating, the substrates are immediately transferred into a convection oven from Binder for annealing. To avoid disturbing the wet film uniformity during this transfer, it is important to ensure that the freshly coated film reaches saturation and most of the solvent evaporated before

removing the substrate from the applicator bed. The distance between film applicator and meniscus guide lower edge was set using feeler gauges and the N_2 flow in the air-knife was set using a flowmeter EK-SR from Kytola. The whole set-up was assembled inside a fume hood located in a clean room (ISO9) with a relative humidity of $(23 \pm 3) \%$ and temperature of $(26 \pm 1) ^\circ C$ - Figure 1. For the first trials of the 2D spacer cations, a blade coater (Zehntner ZUA 2000.200 Universal Applicator) was used instead.

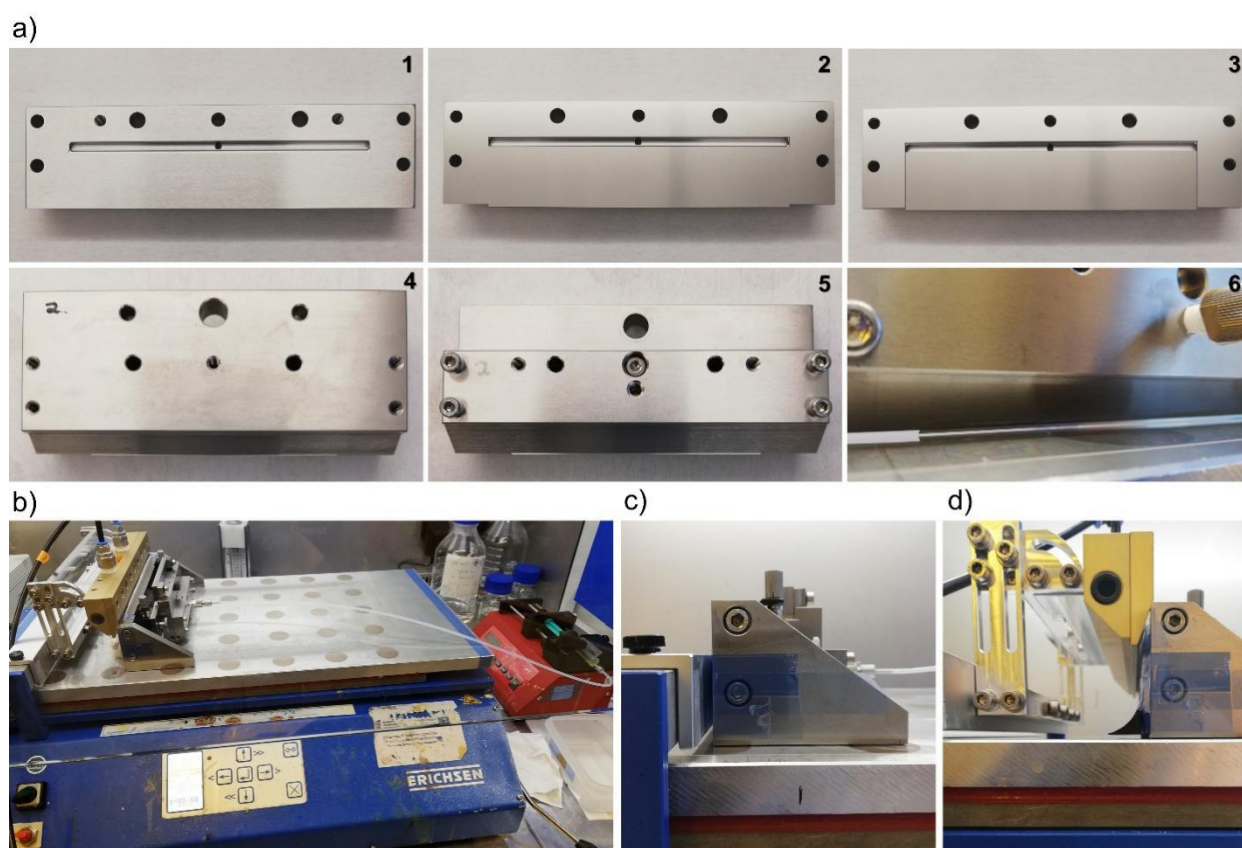


Figure 1 – a) Shims assembly with meniscus guide; b) pump and film applicator with air-knife and slot-die coater assembled; slot-die head and attachment part c) for the SnO_2 and d) for the 3D perovskite deposition.

SnO_2 layer fabrication

The SnO_2 solution was diluted with deionized water and IPA (60:40 v:v) to 1 wt %. A surfactant based on octyl-pyrrolidone (0.2 wt % with respect to SnO_2 solution) was added to the final mixture. It was used a shim 10 cm wide and 150 μm thick,

and a meniscus guide shim with a length of 800 μm . Before the coating, the PET/ITO surface was treated with N_2 plasma for 2 min at a power of 75 W and 20 mL min^{-1} using a plasma system from PLASMA ETCH. The optimized parameters for the deposition of this solution are: 925 μm gap (distance between the substrate's top surface and slot-die head lips), a speed of 1 m min^{-1} , a pumping rate of 800 $\mu\text{L min}^{-1}$ (wet film thickness of about 8 μm), a bed temperature of 65 $^\circ\text{C}$, followed by annealing at 100 $^\circ\text{C}$ for 45 min. Alternatively, a high-quality layer can also be obtained at a speed of 0.45 m min^{-1} if using a temperature of 40 $^\circ\text{C}$ and pumping rate of 350 $\mu\text{L min}^{-1}$. Air-knife is not required for this deposition.

Perovskite solution

For the perovskite deposition, a 0.6 M solution was prepared inside a N_2 filled glovebox by dissolving PbI_2 , PbBr_2 , FAI and MABr in a solvent mixture of ACN:2-ME 60:40 (v:v) according to the composition $(\text{FAPbI}_3)_{0.85}(\text{MAPbBr}_3)_{0.15}$. DMSO was added in a 50 % molar ratio with respect to the perovskite solution. This solution was stirred during 3.5 h to ensure a good particle size distribution (single peak at 1.7 nm) - Figure 2a), and filtered with 0.22 μm PTFE filter prior deposition.

Perovskite layer fabrication

Regarding the slot-die settings, it was used a shim 10 cm wide and 50 μm thick, and a 800 μm long meniscus guide. A 19 cm wide air-knife was assembled to the film applicator, and a tool to make the N_2 flow parallel to the surface was attached to the slot-die attachment part, with a distance from the bed of around 2 mm. N_2 pressure was set to 2 bar, corresponding to a flow of 75 L min^{-1} . SnO_2 samples were pre-treated with N_2 plasma for 2 min and the perovskite solution was subsequently coated by slot-die using the following parameters: 925 μm gap, 1 m min^{-1} speed, 500 $\mu\text{L min}^{-1}$ pumping rate (wet film thickness of 8 μm), 25 $^\circ\text{C}$ bed temperature. The impact of the N_2 flow from the air-knife causes the evaporation of the major part of solvents, triggering the film saturation and the formation of the perovskite's intermediate phase – Figure 2b). After coating, the

films were immediately transferred to the oven to be annealed at 120 °C for 20 min – Figure 2c,d). A small purge was made in between each deposition.

OAI layer fabrication

A solution of 10 mM OAI in IPA was deposited on the annealed perovskite films at 1 m min⁻¹ and 25 °C, using air-knife with a N₂ flow of 60 L min⁻¹. It was used a 9 cm wide and 50 μm thick shim, and a meniscus guide with a length of 500 μm. The gap was set to 575 μm and pump rate to 270 μL min⁻¹, producing a wet film thickness of 3.0 μm. For the first trials with the 6 different spacer cations (OAI, PEAI, ThMAI, 4FPEAI, BAI and 5-AVAI), air-knife assisted blade coating method was used instead for process simplification - gap of 275 μm.

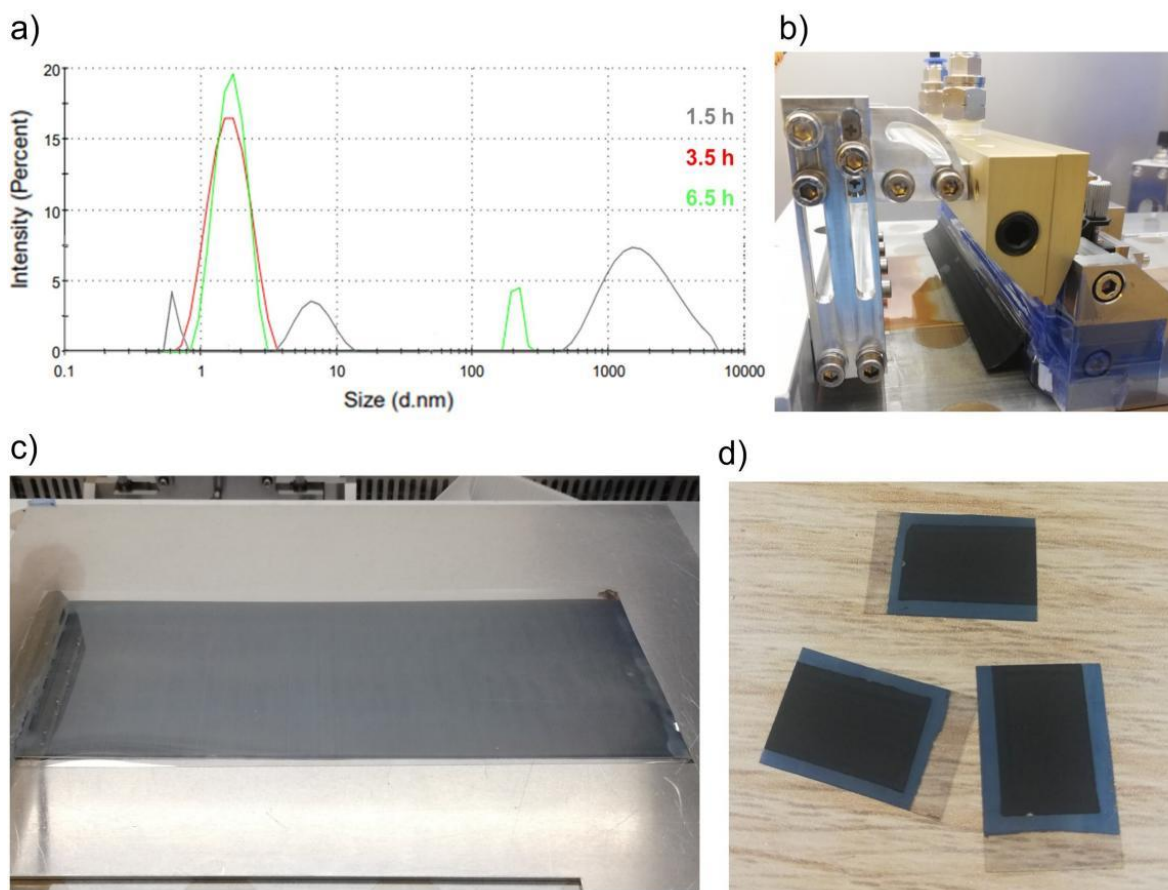


Figure 2 – a) Particle size distribution of 3D perovskite solution for different stirring times; b) perovskite's intermediate phase after parallel N₂ flow exposure during slot-die coating; c) slot-die coated 3D perovskite film after annealing: 10 cm x 20 cm; and d) complete perovskite solar cells of 1.8 cm x 1.2 cm.

Carbon layer fabrication

Small cells of 1.2 cm x 1.8 cm were cut from the slot-die coated films. Carbon paste was then manually blade-coated using a glass rod on top of the perovskite layer, with a final area of approximately 1 cm x 1.2 cm and annealed in a convention oven at 85 °C for 30 minutes (carbon thickness ~15 μm).

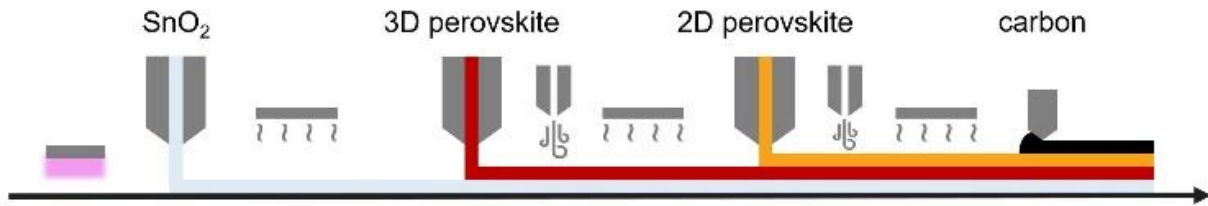


Figure 3 – Illustration of the fabrication procedure: slot-die coating of SnO₂, 3D and 2D perovskite layers, and blade coating of the carbon electrode layer.

4.2.2. Characterization methods

Current density–voltage (JV), stabilized power output (SPO) and maximum power point tracking (MPPT) measurements - JV and SPO measurements were performed using a Keithley 2461 source measure unit (SMU). For the indoor low-light conditions, we used a warm white LED (CLU028-1201C4-303H7M5-F1, Citizen Electronics, ~3270 K), and illuminance was set to 200 lux (76.1 μW cm⁻²) and 1000 lux (372.2 μW cm⁻²). The absolute spectrum - Figure 4 - at each illuminance value was determined using a spectrometer SEKONIC C-800 Spectromaster, and irradiance was then calculated by integrating the area of the spectrum obtained. For the measurements at simulated AM1.5G irradiation (100 mA cm⁻²), an AAA-rated solar simulator (Abet Technologies, sun 2000) was used, calibrated against an RR-208-KG5 silicon reference cell (Abet Technologies). Solar cells were masked to 0.64 cm². JV measurements were performed in two scan directions, from forward bias to short-circuit and from short-circuit to forward bias. The scanning rate was set to 0.5 V s⁻¹. The stabilized power conversion efficiency (SPO) was measured at the maximum power point voltage for a duration of 54 seconds. MPPT was performed with equipment and software designed by the engineers at Saule S.A.

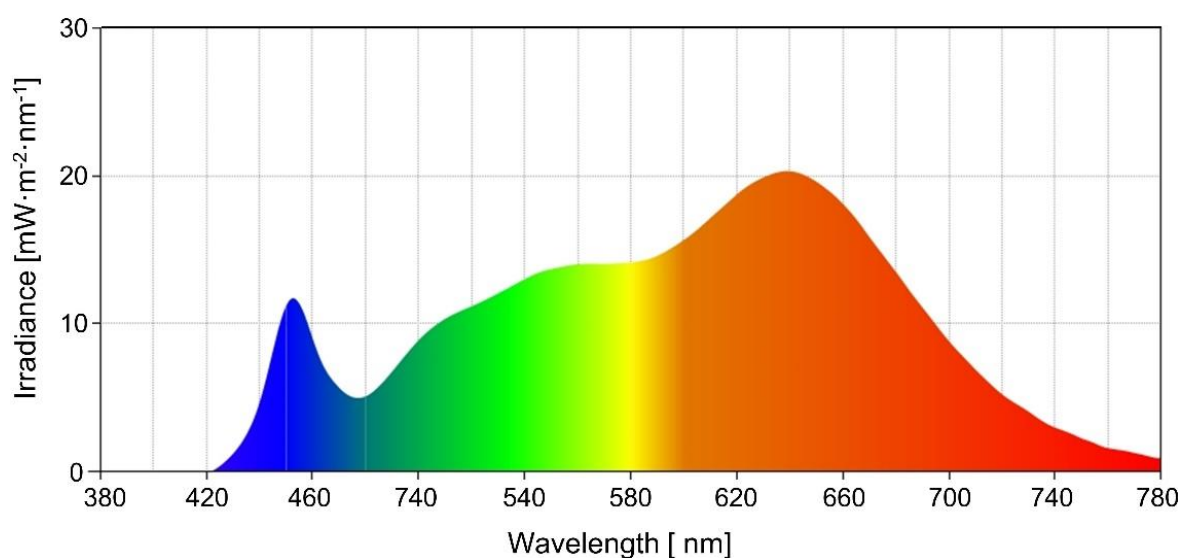


Figure 4 – Spectrum of the warm white ~3270K LED used at 1000 lux ($372 \mu\text{W cm}^{-2}$).

Hyperspectral imaging – photoluminescence Photoluminescence measurements were performed in a hyperspectral imaging microscope (Photon Etc). A green laser (wavelength: 532 nm, irradiance) was used as excitation source. The laser was focused onto the surface of the perovskite layer using a 100x objective, resulting in a spot size with 330 μm diameters. The photoluminescence from the perovskite layer was collected through the same objective and analyzed with the hyperspectral imager (IMA-VISTM, Photon Etc). The illumination intensity was varied between 1 and 0.01 sun by changing the laser power and using optical neutral density filters.

Scanning electron microscopy (SEM) images were obtained using the Phenom Pro-X microscope. Cross-section images (focused ion beam scanning electron microscopy, FIB-SEM) were taken with the SEM/Ga-FIB Microscope FEI Helios NanoLab™ 600i. X-ray diffraction (XRD) patterns were recorded using the Rigaku MiniFlex diffractometer with the $\text{CuK}\alpha$ ($\lambda = 1.541 \text{ \AA}$) radiation at room temperature. External quantum efficiency (EQE) spectra were obtained using Bentham PVE300 photovoltaic characterization system and the control software BenWin+. UV-Vis absorption spectra were obtained with the Edinburgh Instruments

Spectrofluorometer FS5, using a Xe lamp light source and an excitation wavelength of 405nm. A rheometer from Brookfield (DV3T) was used to determine the viscosity of each solution at 25°C and shear rate of 375 s⁻¹. Contact angle measurements were performed with a Attension® Theta Lite optical tensiometer. Dynamic light scattering was used to determine the particle size distribution of the perovskite solution after different stirring times were measured with the rheometer Zetasizer nano ZS from Malvern.

4.3. Results and discussion

4.3.1. Solutions optimization

SnO₂ dispersion

SnO₂ is one of the most widely used materials for flexible planar n-i-p PSC, given its high stability, low cost and annealing temperatures compatible with flexible substrates (lower than 140 °C).⁶ Furthermore, SnO₂ is an aqueous based colloidal dispersion, thus posing no risks to health or the environment. To increase the adhesion of the SnO₂ dispersion to the PET/ITO surface and maximize the coating speed (or minimize the coating temperature), a volatile solvent - 2-propanol (IPA) - was added into the dispersion. The maximum ratio of IPA in a 1 % (wt) dispersion is 45 % (v). Above this concentration, the SnO₂ nanoparticles start agglomerating due to a change in pH from basic to neutral, resulting in a milky dispersion that is not proper for deposition, as shown in Figure 5a).⁷ To prevent particle agglomeration is beneficial to keep the dispersion cold. We used 40 % (v) IPA for having a better dispersion stability. This amount of IPA and surfactant proved sufficient to reduce the contact angle from 31° to 17° (after 2 min N₂ plasma treatment on PET/ITO substrate) - Table 1. To further increase the wettability of the dispersion, a small amount of surfactant was added (0.17 uL mL⁻¹).

Table 1 – Contact angle at different times of water, diiodomethane, SnO₂ solvents and perovskite solvents on PET/ITO and SnO₂ films with different surface treatments.

Contact angle [°]					
solvent	surface	pre-treatment	after 0.5s	after 2s	after 4s
water	PET	none	62.0	missing data	
		UV/ozone	50.9	50.6	49.8
		plasma	31.1	29.8	28.7
diiodomethane	PET	none	51.4	50.9	50.1
		UV/ozone	50.6	50.3	50.1
		plasma	32.2	31.7	31.2
SnO ₂ solvents	PET	none	33.7	32.9	32.5
		UV/ozone	30.8	29.6	28.4
		plasma	17.4	15.1	14.0
water	SnO ₂	none	37.3	36.7	36.1
		UV/ozone	15.5	13.0	10.0
		plasma	7.8	3.7	-
diiodomethane	SnO ₂	none	37.4	36.7	36.5
		UV/ozone	38.1	37.6	37.7
		plasma	31.5	31.2	31.4
perovskite solvents	SnO ₂	none	10.8	5.0	-
		UV/ozone	12.9	11.0	10.3
		plasma	6.7	3.7	-
OAI solution	perovskite	none	6.9	<3	-

3D perovskite solution

The perovskite composition has a major impact on the photovoltaic performance and stability of the final device. Theoretically, wide-band gap perovskites offer the potential for higher efficiencies under low-light conditions, since they have a better overlap with the spectrum of the lamps and are capable of generating higher photovoltage.⁸ Usually, adding bromide to the perovskite composition widens the

band-gap of perovskite materials, however it compromises their stability due to phase segregation triggered by light soaking, particularly for bromide molar ratios higher than 0.2.⁹ This effect can be significantly reduced by adding a specific amount of a cesium salt to the perovskite composition, for instance, ratio of 0.17 of cesium (0.83 formamidinium) when using 0.30 of bromide (0.70 iodide).¹⁰ Nevertheless, these two substances and in particular cesium salts, have major solubility issues on most of the solvents used for perovskite, and have a narrower coating window for obtaining a high-quality defect-free perovskite film.¹¹ In this context, since the rheology and properties of the solvents are essential for the slot-die coating, it is preferable to avoid cesium and thus minimize bromide content. Using a low methylammonium concentration is also preferable given its low stability to humidity and high volatility. Previous researches have confirmed the suitability of the $(\text{FAPbI}_3)_{0.85}(\text{MAPbBr}_3)_{0.15}$ composition for large-scale deposition techniques under ambient atmosphere, and exhibits improved operational stability for over 1000 hours in outdoor conditions.¹²⁻¹⁴ Thus, despite the lower band-gap (1.61 eV), this composition was chosen for the present work.

Tuning the physico-chemical and rheological properties of the solvents is essential for obtaining a high-quality film by slot-die coating. The most important properties to be considered for the perovskite deposition are the volatility, polarity, viscosity, and toxicity. To achieve an optimal coating deposition at a high coating speed and low temperatures, it is important to maximize volatility, and minimize viscosity. This enables fast and efficient coating processes while maintaining the desired film quality. The solvent should have the right polarity to be able to effectively solubilize the perovskite without damaging the underlying layer and it should not be hazardous for human health or environment. In this context, acetonitrile (ACN) is a good option, however, when no other solvent is added, ACN results in the precipitation of perovskite. Adding 2-methoxyethanol (2-ME), even though it is not classified as a green solvent, hinders perovskite precipitation: the minimum amount required is 40 % (v) for a 0.6 M solution - Figure 5b). In fact, the ratio ACN:2-ME ratio of 60:40 (v:v) has already been demonstrated to be a good

solvent mixture for large-scale coating techniques at room temperature.¹⁵ Furthermore, DMSO was used as additive (with a molar concentration of 50 % of the perovskite - 0.3 M), since its high coordination ability with the perovskite results in the enhancement of the perovskite crystallinity and adhesion to the underlying layer.¹⁵

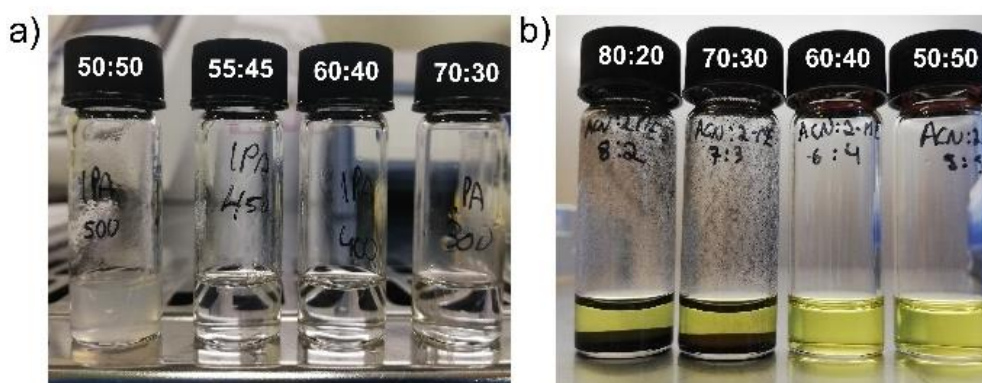


Figure 5 – a) SnO₂ dispersion with different water:IPA ratios, and b) perovskite solutions with different ACN:2-ME ratios.

2D perovskite solution

The free charge carrier's density generated with indoor lamps is significantly lower than the density generated at 1 sun (irradiance is ~300 x lower at low-light). Thus, the recombination within the trap-sites present in a PSC has a much greater impact on the photovoltaic performance under low-light conditions. In particular, a major part of this recombination happens at the perovskite crystal surface due to the high density of crystallographic imperfections, such as uncoordinated sites (Pb⁺, I⁻), uncoordinated ions (Pb²⁺, I⁻ or Br⁻), Pb clusters, and organic cation vacancies.¹⁶ Coating an ultra-thin layer of long chain organic cations on top of the perovskite surface - forming a hybrid 2D/3D perovskite layer - is a promising way of passivating these defects while simultaneously creating a "moisture shielding" effect that enhances ambient stability. These spacer cations replace MA⁺ and FA⁺ sites, forming a 2D perovskite layer.¹⁷ It is important to ensure that the solvent used to dissolve the 2D spacer organic cation does not damage the 3D perovskite, thus a test was done using six different solvent systems - Figure 6a). IPA was

selected given its low toxicity, high volatility, relatively low viscosity, and proper polarity. The most relevant properties of the solvents are presented in Table 2.

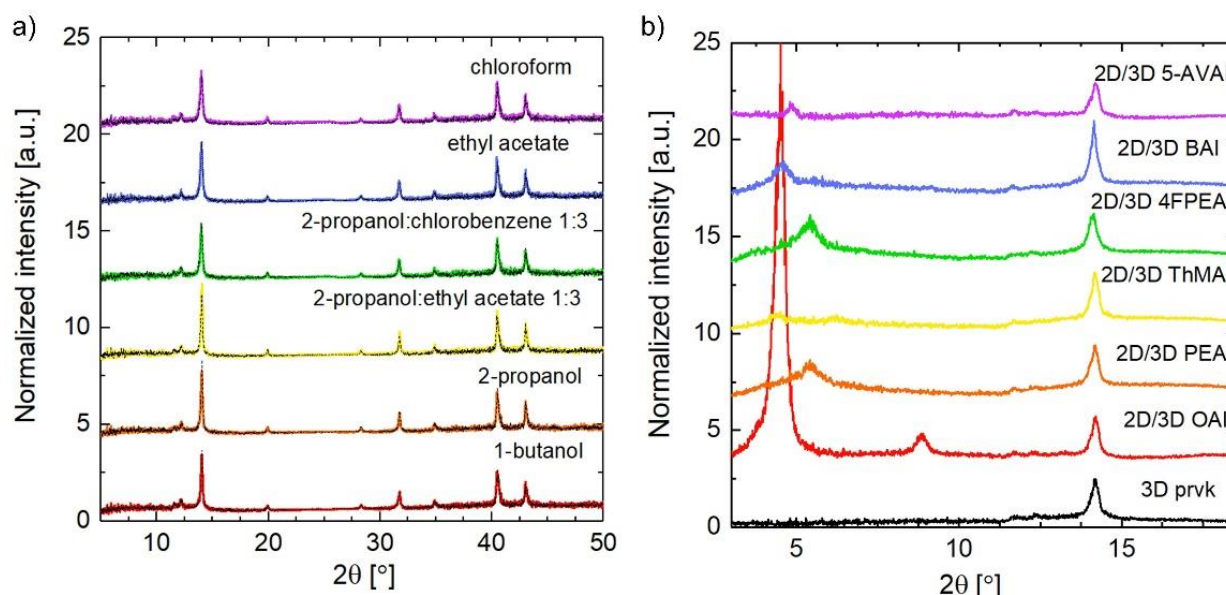


Figure 6 - XRD data of a) 3D perovskite before and after blade coating different solvents, and b) after blade coating 10 mM of 6 different spacer cations on 3D perovskite, followed by annealing at 85 °C for 5 min.

Table 2 – Most relevant properties of the solvents used in the slot-die coating depositions.¹⁸

Solvents	Abr.	Boiling point at 1 atm [°C]	Viscosity at 20-25°C [cP]	Dielectric Constant	Toxicity
acetonitrile	ACN	81	0.38	38.8	problematic
2-methoxyethanol	2-ME	124	1.72	16.9	hazardous
dimethyl sulfoxide	DMSO	189	1.99	47.2	problematic
water	H ₂ O	100	1.00	80.1	recommended
chloroform	CF	61	0.57	4.81	highly hazardous
ethyl Acetate	EA	77	0.43	6.4	recommended
chlorobenzene	CBZ	132	0.80	5.6	hazardous
1-butanol	BuOH	118	2.98	7.8	recommended
2-propanol	IPA	83	2.40	19.9	recommended

Also, in a preliminary study six long-chain ammonium iodides were selected and deposited by blade coating (with same molarity and ensuring the best possible approximation to the slot-die conditions/parameters): n-octylammonium iodide (OAI), phenethylammonium iodide (PEAI), 2-thiophene methylammonium iodide (ThMAI), 4-fluoro-phenethylammonium iodide (4FPEAI), n-butylammonium iodide (BAI) and 5-ammonium valeric acid iodide (5-AVAI). XRD data confirms the presence of a 2D perovskite phase for all the organic salts (XRD peaks located between 4.4° and 8.8°) – Figure 6b).¹⁹ However, the intensity of the 2D peak for the OAI salt is much higher than the 2D peaks for the other salts, which indicates that the 2D layer of OAI has a higher crystalline structure. Indeed, this was the sample that provided the best photovoltaic performance both at 1000 lx and 1 sun - Figure 7. In general, spacer cations with longer alkyl chains and higher hydrophobicity, such as octylammonium (OA^+), have shown to be more efficient in reducing defects, improving charge transport, and enhancing device performance.²⁰ The remaining spacer cations resulted in a decrease in photovoltaic performance, most likely due to the unfavorable tendency to crystallize with the organic layers perpendicular to the direction of charge transport.

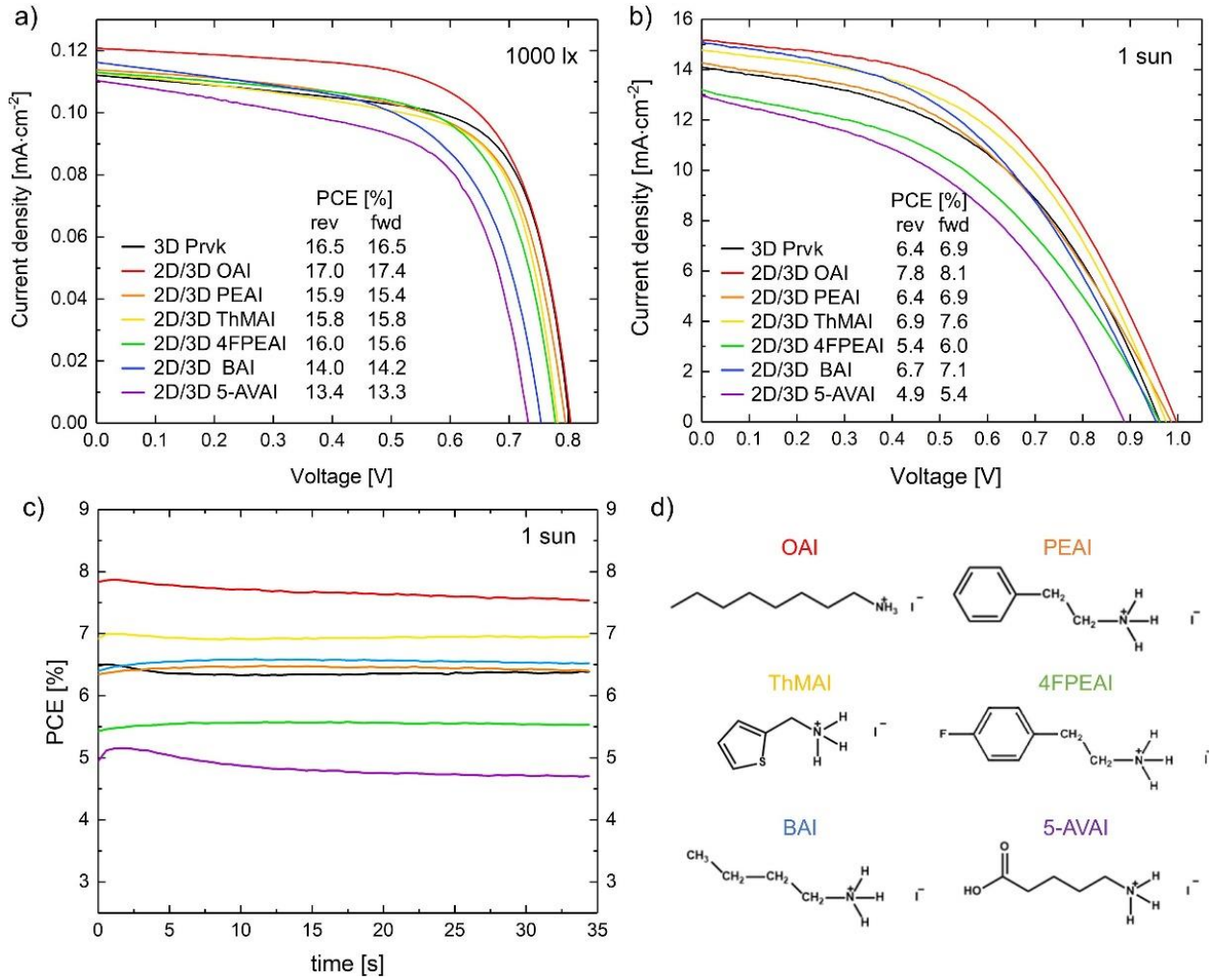


Figure 7 – a) JV curves of slot-die coated samples with each 2D perovskite salt at a) 1000 lx and b) 1 sun with the respective PCE values at reverse and forward scan; c) and stabilized power output at 1 sun; and d) molecular structure of the six long-chain alkylammonium iodides selected for the 2D perovskite.

4.3.2. Pre-treatment

The deposition methods and treatments selected are all compatible with a R2R deposition. However, at this initial stage and considering the available equipment, it was adopted a batch sheet-to-sheet (S2S) model of production. The first step of manufacturing was the P1 laser patterning, followed by the coating of SnO₂ and perovskite layers. For obtaining an uniform film with good adhesion to its underlying layer, it is very advantageous to functionalize the surface of the substrate by removing organic contaminants and by adding specific functional groups to the surface. This functionalization will increase the wettability of the solutions to the substrate without damaging it and promote a high-quality growth of the coated material.²¹ Furthermore, according to the viscocapillary model of the slot-die coating technique, increasing the surface energy of the coating surface results in a wider coating window, i.e. broadens the range of possible variables for the rheology and operating parameters.²² Two of the most used techniques for ultrafine cleaning and functionalization of surfaces are N₂ plasma and UV/ozone.²³

To understand the impact of each surface modification treatment on the quality of the coating, SnO₂ and perovskite solutions were coated on PET/ITO and SnO₂ (respectively), before and after N₂ plasma and UV/ozone – Figure 8. To avoid any damage to the 3D perovskite surface, the 2D solution was coated on perovskite with no treatment. In fact, the contact angle of OAI in IPA on 3D perovskite is so low that there is no need for modifying the surface energy. Contact angle values and images of each configuration are presented in Table 1 and Table 3, respectively. Also, the contact angle of diiodomethane and water on each substrate before and after the surface treatments was also determined in order calculate the surface energy by the Owens, Wendt, Rabel and Kaelble (OWRK) method – Table 3.²⁴ The total surface energy corresponds to the sum of the polar and the dispersive components. Since water reacts with the perovskite, and given the similar contact angle results, the surface energy of the perovskite surface with no treatment was assumed to be close to the N₂ plasma treated SnO₂.

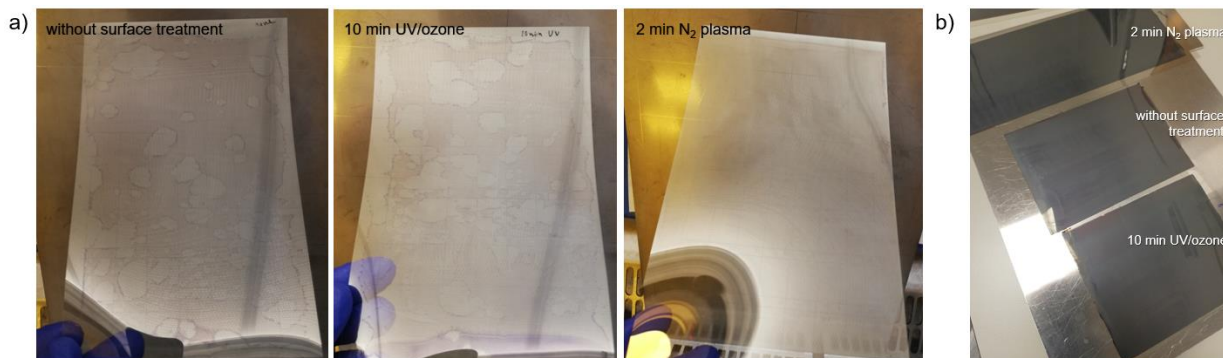


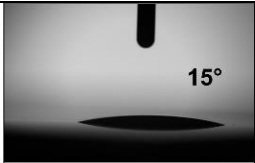






Figure 8 – Pictures of the a) SnO₂ and b) perovskite films coated on PET/ ITO and SnO₂ (respectively), after different surface treatments.

Table 3 - Contact angle of SnO₂ dispersion, 3D and 2D perovskite solutions on the respective substrates before and after 15 min UV/ozone and 2 min N₂ plasma surface treatments.

Contact angle				
Pre-treatment	None	15 min UV/ozone	2 min plasma	
SnO ₂ solution on PET	 33°	 30°	 15°	
3D perovskite solution on SnO ₂	 5°	 11°	 4°	
2D perovskite solution on 3D perovskite	 < 3°			
Surface energy [mN m ⁻¹]				
Substrate	Treatment	Polar component	Dispersive component	Total
PET	none	13.74	33.49	47.23
	UV/ozone	20.28	33.94	54.21
	N ₂ plasma	26.62	43.29	69.91
SnO ₂	none	24.71	40.89	65.6
	UV/ozone	34.17	40.55	74.72
	N ₂ plasma	33.99	43.59	77.58

The low surface energy of PET/ITO (47 mN m^{-1}) results in a very high contact angle with the SnO_2 solution (33°), consequently the freshly coated SnO_2 film dewets before reaching the saturation point, resulting in a film with very low coverage and uniformity – Figure 8a). Removing the organic contaminants from this surface by applying 15 min UV/ozone results increases the polar component of surface energy by 48 %, but has virtually no effect on the dispersive component. Overall, the total surface energy increases only by 15 %, which is not enough to avoid dewetting. On the other hand, N_2 plasma both increases the polar and dispersive components by 94 % and 29 %, respectively - total increase/decrease of 48 % in the surface energy/contact angle, which enables the coating of highly uniform SnO_2 film. Apart from surface ultra-fine cleaning, N_2 plasma triggers the co-generations of N_2 doping species and oxygen vacancies on the surface, which is the most likely cause of the significant surface energy modification.²⁵

Regarding the SnO_2 film, it already presents a high surface energy (66 mN m^{-1}), and perovskite can be grown on this layer without any treatment - Figure 8b). Interestingly, exposing the SnO_2 surface to UV/ozone resulted in a higher contact angle of the 3D perovskite solution - the long hydrophobic chains of the surfactant might have been broken by the ozone generated by the UV light, decreasing the intermolecular forces between the SnO_2 layer and the 3D perovskite solution - slight decrease in the dispersive component. On the other hand, N_2 plasma pre-treatment doesn't damage the surfactant molecules, actually it increases the surface energy by 18 % and might enhance its structural, optical and electrical properties²⁶. Thus, N_2 plasma pre-treatment was employed to have a more flexible coating window.

4.3.3. Slot-die coating

Before coating the optimized solutions, the viscocapillary model of slot-die coating was used to determine the range of operating parameters (volumetric pumping rate, coating speed, meniscus guide length, and gap) that produce a stable

meniscus and high-quality defect-free film.²⁷ The capillary number is a dimensionless quantity that represents the ratio between viscous forces and the surface tension forces of a specific solution. It can be obtained using equation (1):

$$Ca = \frac{\mu V}{\sigma} \quad (1)$$

where μ is the viscosity, V the coating speed and σ the surface energy.²⁷ Ca can also be calculated using operating parameters, using equation 2:

$$Ca = 0.65 \left(\frac{2}{\frac{H_0}{t_{wet}} - 1} \right)^{\frac{3}{2}} \quad (2)$$

where H_0 is the gap and t_{wet} the wet film thickness, which is calculated using the pumping rate (Q), width of coating (w), coating speed (V), and equation (3).²⁷ The ratio between H_0 and t_{wet} is called the dimensionless gap number.

$$t_{wet} = \frac{Q}{w \cdot V} \quad (3)$$

For this optimization, meniscus guides are used to avoid flooding of the edges and increase the coating uniformity. The H_0 corresponds to the distance between slot-die head lips and the surface of substrate, so in this case corresponds to the sum of the meniscus guide length and distance between the lower edge of the meniscus guide and surface of the substrate. Better coatings are usually achieved for solutions with low Ca , e.g., low viscosity, low coating speed and high surface energy. These parameters can be adjusted according to the coating restrictions, but there is a maximum value for Ca in which defects such as rivulets and ribbing start appearing - $Ca_{critical}$. By plotting equation (2) (set H_0 and vary t_{wet}) it is possible to identify the limit between stable and unstable coating - low flow limit - Figure 9. For the SnO_2 and 3D perovskite, the gap and meniscus guide length used was 925 μm and 800 μm , respectively. Since the t_{wet} of OAI is expected to be very small, the gap was reduced to 575 μm and meniscus guide to 500 μm . Using these values and the rheological values obtained for each solution, the maximum coating speed and minimum pumping rate and wet film thickness were determined – inset table in Figure 9.

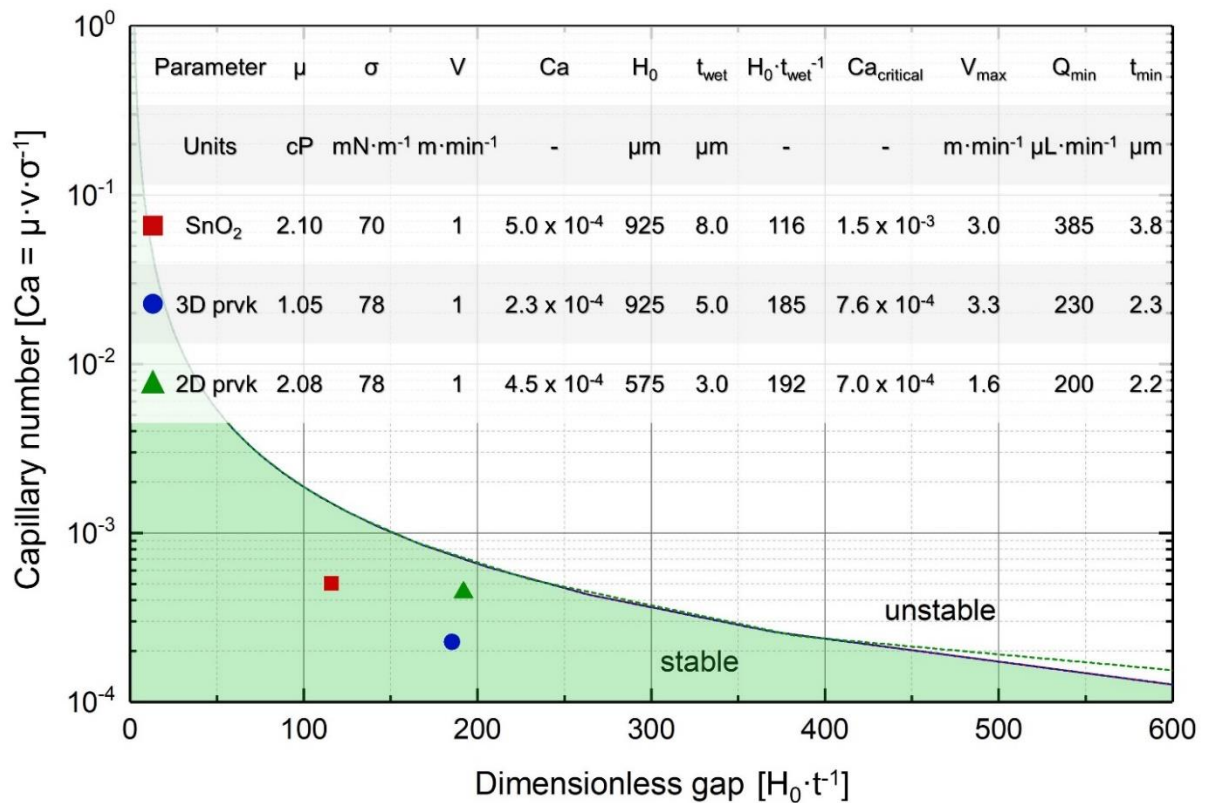


Figure 9 – Low flow limit model for the SnO₂, 3D and 2D perovskite solutions, and respective Capillary number. Inset table: Rheological and operational parameters for each solution and low flow limit values obtained with the viscocapillary model.²⁷

The maximum coating speed for the SnO₂, 3D perovskite and 2D perovskite is 3.0 m min⁻¹, 3.3 m min⁻¹ and 1.6 m min⁻¹. It is interesting to note that the maximum coating speed for SnO₂ is almost twice that 2D perovskite, despite the very similar rheological parameters (viscosity and surface energy). This happens due to the lower wet film thickness of the 2D perovskite and clearly shows that a way for increasing the coating speed is by increasing the wet film thickness and decreasing the concentration of the solution, so the same final dry film thickness is achieved. Still, another way to increase the coating speed is by adjusting the solvent system to decrease the viscosity of the solution - 3D perovskite solution has a thinner wet film than SnO₂ dispersion and still has similar maximum coating speed due to the lower viscosity. If solutions (solvent system and concentration) cannot be changed, decreasing the gap enables the use of higher coating speeds and thinner wet films without compromising the meniscus stability. Additionally, if

the coating window is still too narrow, stronger surface treatments and additives (such as surfactants) can be employed. Overall, in the slot-die coating technique, the large number of variables and the interplay between them makes it difficult and time-consuming to achieve consistent and high-quality coatings. Thus, to overcome this challenge it is often necessary to fix some variables and cautiously design a set of experiments that allows to optimize the remaining variables.

To mimic a R2R process, the coating speed was set to 1 m min^{-1} . At this speed, a coating temperature of $65 \text{ }^\circ\text{C}$ is required for having a good drying of the SnO_2 solution - solvent evaporates and SnO_2 film forms uniformly $\sim 5 \text{ cm}$ behind the slot-die head (experimentally verified). The pumping rate was defined to obtain $8 \text{ }\mu\text{m}$ wet film thickness, which corresponds to $800 \text{ }\mu\text{L min}^{-1}$ (coating width is 10 cm). This is the ideal wet film thickness for obtaining a compact $\sim 40 \text{ nm}$ thick SnO_2 . Alternatively, it was experimentally verified that the coating temperature can be reduced to 40°C by reducing the coating speed to 0.45 m min^{-1} . For the 3D perovskite deposition, the coating bed was kept at room temperature - $(26 \pm 1) \text{ }^\circ\text{C}$ - and an air-knife was assembled to the coater, with a fixed N_2 flow of 75 L min^{-1} .

To reduce the wet film disturbance by the strong impact of the N_2 flow from the air-knife, a toll was used to change the flow direction from perpendicular to parallel to the surface. This strategy minimizes chatter defects without compromising the fast evaporation rate. Chatter defects refer to the periodic variations in the thickness of the coated layer along the coating direction that were appearing at regular intervals.²⁸ Preliminary studies demonstrated that, with the selected operational parameters and solution, an ideal thickness of $\sim 500 \text{ nm}$ is obtained with a wet film thickness of $5\text{-}6 \text{ }\mu\text{m}$ (pumping rate of $500\text{-}600 \text{ }\mu\text{L min}^{-1}$) - Figure 10. For thinner wet film, the light absorption decreases, reducing the density of photo-generated charge carriers and consequently the current density produced, while for thicker wet films the roughness starts increasing and the photovoltaic performance slightly decreases due to the higher density of trap-assisted recombination.

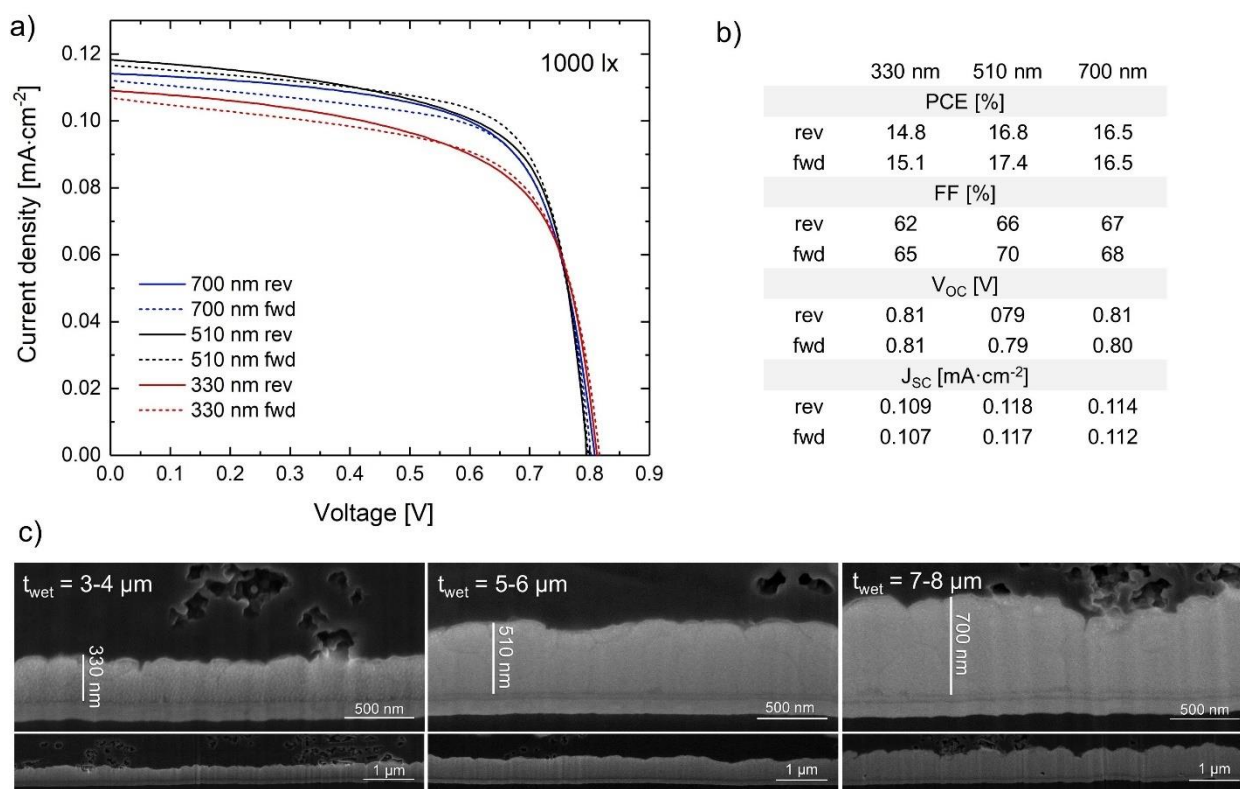


Figure 10 – a) JV curves, photovoltaic parameters, and SEM cross section images of the slot-die coated 3D perovskite film with different wet film thickness: 3-4 μm , 5-6 μm , and) 7-8 μm .

In the case of OAI, since it is an insulating long-chain salt, the thickness of the wet film was minimized to reduce the resistance to charge transfer at that interface with the 3D perovskite. According to the low flow limit plot, at 1 m min^{-1} , the minimum wet film thickness that does not compromise the meniscus stability is $2.2 \mu\text{m}$. To have a more comfortable coating window, the wet film thickness was set to $3 \mu\text{m}$ – pumping rate of $270 \mu\text{L min}^{-1}$ (coating width of 9 cm). XRD data - Figure 11e) - confirms the presence of the 2D perovskite phase - the 2 peaks at 3.7° and 4.3° which corresponds to the (020) crystal plane characteristic of 2D perovskite with dimensionality 2-3.¹⁹ Still, the obtained layer is so thin that is barely noticed in the cross section SEM images - Figure 11b) - and has no influence in the absorption spectrum - Figure 11d).

Carbon deposition

The high viscosity of the commercial carbon paste makes it extremely difficult to deposit by slot-die coating. It was then deposited by blade-coating, resulting in a thickness of $\sim 15 \mu\text{m}$. Future work includes the development of highly conductive carbon paste with low viscosity for solar cell applications. Another alternative is to optimize the carbon deposition by screen-printing, since this process can be also integrated in a R2R process.

4.3.4. Characterization

Adding the 2D perovskite layer resulted in an increase in the photoluminescence (PL) peak height both at low and high irradiance levels, which indicates that the 2D layer did passivate the surface defects, extending the charge carrier lifetime by reducing the recombination pathways. This passivating effect is more noticeable for lower light intensities, which was expected given greatest impact of the trap sites at this light range, and has an evenly positive impact throughout the whole spectrum, as confirmed by the external quantum efficiency EQE data - Figure 11c). The PL peak of 3D perovskite corresponds to a band gap of 1.61 eV, which is in accordance with the values presented in the literature for the selected perovskite formulation - Figure 11a).¹³ The quantum confinement effect of the 2D perovskite should result in the increase in band-gap.²⁹ However, PL peak shifts towards higher wavelengths and band gap decreases to 1.59 eV after the 2D perovskite passivation.

The formulated hypothesis is that during the 2D perovskite coating, the 3D perovskite surface is dissolved by the IPA solvent, and when it recrystallizes back together with the OAI molecule, the surface becomes smoother, enhancing in this way the contact with carbon and the carrier charge extraction, and the surface defects like ion vacancies and uncoordinated sites are healed, increasing the PL peak height. This new structure will also have a higher amount of iodide, which then decreases the bandgap. The large radius of iodide and lower

electronegativity causes an increase in the energy required to excite an electron from the valence band to the conduction band, i.e. band gap.³⁰

Interestingly, the increase in PCE due to this surface passivation at 1000 lux and 1 sun are both ~10 %: from 16.5 % to 18.6 % at 1000 lx ($372 \mu\text{W cm}^{-2}$), and from 6.9 % to 7.7 % at 1 sun - Figure 12a,b). Box charts of the photovoltaic parameters of samples with and without 2D perovskite layer under 1000 lux are presented in Figure 12e). The PCE increase is mainly caused by the higher photo-generated current density, which might be caused by the enhanced contact with the carbon layer after the recrystallization. Regarding stability, the device without the 2D layer kept 92 % of its initial PCE after 550 h at maximum power point tracking under 25 mW cm^{-2} inside a N_2 glovebox. Adding the 2D layer worsened the operational stability by ~20 % (the device kept only 71 % of its initial PCE) - Figure 12d). Although 2D perovskite capping layers are known to increase the stability of the device, they might compromise the long-term stability due to the ionic diffusion between these two layers, triggered and accelerated by constantly stressing the samples with light exposure and applied electrical field. According to Luo et al.³¹, after long time exposure to these stressing factor the 2D perovskite layer totally merges with the 3D perovskite, creating a disorganized 2D/3D perovskite heterostructure with high defect density.

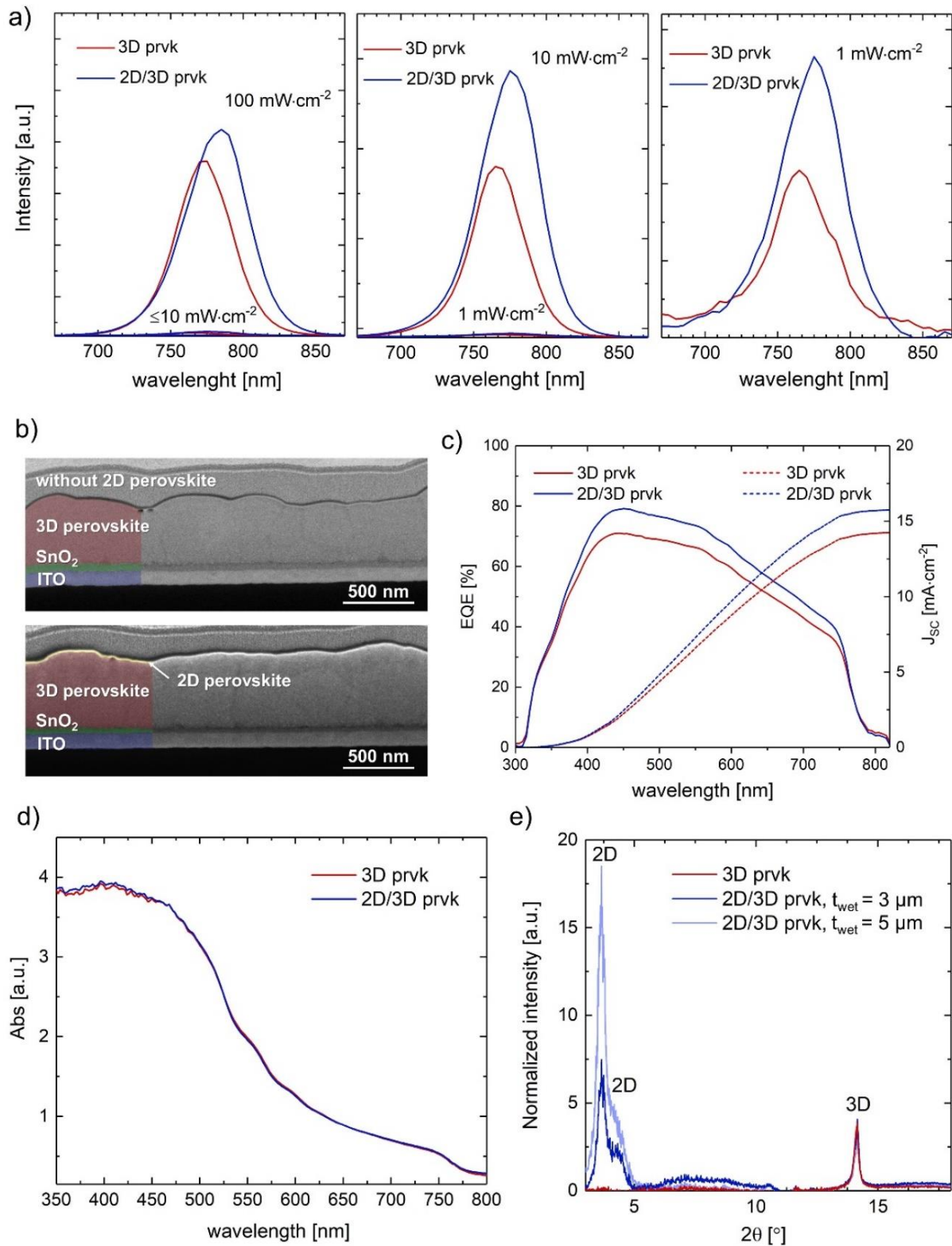


Figure 11 – Characterization data comparing the properties of the 3D perovskite and 2D/3D hybrid perovskite layers – a) PL spectrum at different light intensities (1, 10, and 100 mW cm^{-2}), b) SEM cross section images, c) EQE spectrum and respective cumulative current density, d) UV-visible absorption spectrum, and e) XRD spectrum.

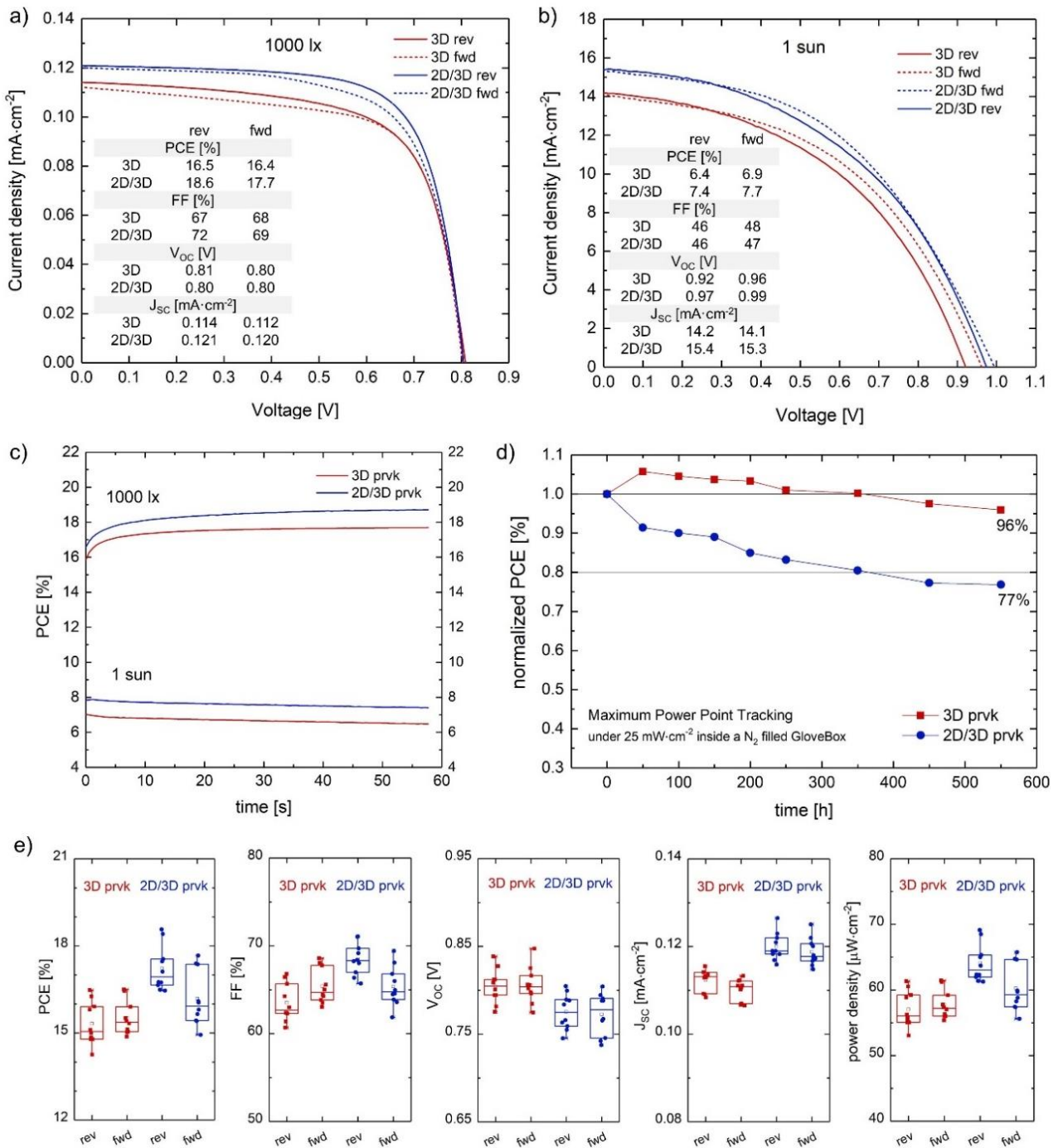


Figure 12 – Comparison of the photovoltaic performance and operational stability of devices with 3D perovskite and 2D/3D perovskite: JV curves at reverse and forwards scan at a) 1000 lx and b) 1 sun and respective photovoltaic parameters; c) stabilized power output at 1000 lx and 1 sun; d) MPPT test under 25 $\text{mW}\cdot\text{cm}^{-2}$ inside N_2 filled glovebox for over 550 h; and e) box charts of the photovoltaic parameters of 10 samples at 1000 lux.

4.4. Conclusion

A procedure for the fabrication of flexible and low-cost perovskite solar devices using a slot-die coating technique is described. The architecture and materials were selected to minimize the number of fabrication steps, energy consumption, and maximize stability and performance. The fabrication process involves coating a metal oxide electron transport material, a mixed-halide 3D perovskite, a 2D perovskite capping/passivation layer, and a carbon-based electrode. The 2D perovskite layer was studied with six different spacer cations, and it was found that the one obtained with n-octylammonium Iodide (OAI) salt yielded the best photovoltaic performance due to its longer alkyl chain and higher hydrophobicity. Surface treatments and coating windows for each material were determined according to the viscocapillary model for the slot-die technique, and the final optimized fabrication procedure resulted in a perovskite solar cell with a maximum PCE of 18.6 % at 1000 lux and 7.7 % at 1 sun. Furthermore, the 3D perovskite device kept 96 % of its initial efficiency after 550 hours of testing under maximum power point tracking. Surprisingly, adding a 2D layer worsened the long-term stability due to the ion diffusion between the 2D and 3D perovskite layers. Next steps consist in the development of a carbon paste compatible with slot-die coating (low viscosity); enhancement of the 2D perovskite; and module fabrication.

Acknowledgements

Cristina Teixeira and Dávid Forgács acknowledge funding from the European Regional Development funds provided by the National Centre of Research and Development (NCBR) under POIR.01.01.01-00-1482/19-00. Luísa Andrade and Adélio Mendes acknowledge Project InPSC (PTDC/EQU-EQU/4193/2021), LA/P/0045/2020 (ALiCE), UIDB/00511/2020 and UIDP/00511/2020 (LEPABE), all supported by national funds through FCT/MCTES (PIDDAC). The authors also

acknowledge the support of Dr. Vivek Babu, Dr. Mario Escobar, Dr. Felipe Vinocour, and Dr. Pierpaolo Spinelli in the experimental procedure development.

References

1. Li, Z.; Klein, T. R.; Kim, D. H.; Yang, M.; Berry, J. J.; van Hest, M. F. A. M.; Zhu, K., Scalable fabrication of perovskite solar cells. *Nature Reviews Materials* **2018**, *3* (4), 18017.
2. Tu, Y.; Ye, J.; Yang, G.; Zang, Y.; Zhang, L.; Wang, Y.; Li, G.; Chu, L.; Yan, W., Slot-die coating fabrication of perovskite solar cells toward commercialization. *Journal of Alloys and Compounds* **2023**, *942*, 169104.
3. Li, J.; Dagar, J.; Shargaieva, O.; Maus, O.; Remec, M.; Emery, Q.; Khenkin, M.; Ulbrich, C.; Akhundova, F.; Márquez, J. A.; Unold, T.; Fenske, M.; Schultz, C.; Stegemann, B.; Al-Ashouri, A.; Albrecht, S.; Esteves, A. T.; Korte, L.; Köbler, H.; Abate, A.; Töbrens, D. M.; Zizak, I.; List-Kratochvil, E. J. W.; Schlatmann, R.; Unger, E., Ink Design Enabling Slot-Die Coated Perovskite Solar Cells with >22% Power Conversion Efficiency, Micro-Modules, and 1 Year of Outdoor Performance Evaluation. *Advanced Energy Materials* **2023**, *n/a* (n/a), 2203898.
4. Burkitt, D.; Patidar, R.; Greenwood, P.; Hooper, K.; McGettrick, J.; Dimitrov, S.; Colombo, M.; Stoichkov, V.; Richards, D.; Beynon, D.; Davies, M.; Watson, T., Roll-to-roll slot-die coated P–I–N perovskite solar cells using acetonitrile based single step perovskite solvent system. *Sustainable Energy & Fuels* **2020**, *4* (7), 3340-3351.
5. Beynon, D.; Parvazian, E.; Hooper, K.; McGettrick, J.; Patidar, R.; Dunlop, T.; Wei, Z.; Davies, P.; Garcia-Rodriguez, R.; Carnie, M.; Davies, M.; Watson, T., All-Printed Roll-to-Roll Perovskite Photovoltaics Enabled by Solution-Processed Carbon Electrode. *Advanced Materials* *n/a* (n/a), 2208561.
6. Uddin, A.; Yi, H., Progress and Challenges of SnO₂ Electron Transport Layer for Perovskite Solar Cells: A Critical Review. *Solar RRL* **2022**, *6* (6), 2100983.
7. Richards, D.; Burkitt, D.; Patidar, R.; Beynon, D.; Watson, T., Predicting a process window for the roll-to-roll deposition of solvent-engineered SnO₂ in perovskite solar cells. *Materials Advances* **2022**, *3* (23), 8588-8596.
8. Freunek, M.; Freunek, M.; Reindl, L. M., Maximum efficiencies of indoor photovoltaic devices. *IEEE Journal of Photovoltaics* **2013**, *3* (1), 59-64.
9. Draguta, S.; Sharia, O.; Yoon, S. J.; Brennan, M. C.; Morozov, Y. V.; Manser, J. S.; Kamat, P. V.; Schneider, W. F.; Kuno, M., Rationalizing the light-induced phase separation of mixed halide organic–inorganic perovskites. *Nature Communications* **2017**, *8* (1), 200.

10. Knight, A. J.; Borchert, J.; Oliver, R. D. J.; Patel, J. B.; Radaelli, P. G.; Snaith, H. J.; Johnston, M. B.; Herz, L. M., Halide Segregation in Mixed-Halide Perovskites: Influence of A-Site Cations. *ACS Energy Letters* **2021**, *6* (2), 799-808.
11. Wan, X.; Yu, Z.; Tian, W.; Huang, F.; Jin, S.; Yang, X.; Cheng, Y.-B.; Hagfeldt, A.; Sun, L., Efficient and stable planar all-inorganic perovskite solar cells based on high-quality CsPbBr₃ films with controllable morphology. *Journal of Energy Chemistry* **2020**, *46*, 8-15.
12. He, M.; Li, B.; Cui, X.; Jiang, B.; He, Y.; Chen, Y.; O'Neil, D.; Szymanski, P.; Ei-Sayed, M. A.; Huang, J.; Lin, Z., Meniscus-assisted solution printing of large-grained perovskite films for high-efficiency solar cells. *Nature Communications* **2017**, *8* (1), 16045.
13. Fong, P. W.-K.; Hu, H.; Ren, Z.; Liu, K.; Cui, L.; Bi, T.; Liang, Q.; Wu, Z.; Hao, J.; Li, G., Printing High-Efficiency Perovskite Solar Cells in High-Humidity Ambient Environment—An In Situ Guided Investigation. *Advanced Science* **2021**, *8* (6), 2003359.
14. Reyna, Y.; Salado, M.; Kazim, S.; Pérez-Tomas, A.; Ahmad, S.; Lira-Cantu, M., Performance and stability of mixed FAPbI₃(0.85)MAPbBr₃(0.15) halide perovskite solar cells under outdoor conditions and the effect of low light irradiation. *Nano Energy* **2016**, *30*, 570-579.
15. Deng, Y.; Van Brackle, C. H.; Dai, X.; Zhao, J.; Chen, B.; Huang, J., Tailoring solvent coordination for high-speed, room-temperature blading of perovskite photovoltaic films. *Science Advances* **2019**, *5* (12), eaax7537.
16. Lu, H.; Krishna, A.; Zakeeruddin, S. M.; Grätzel, M.; Hagfeldt, A., Compositional and Interface Engineering of Organic-Inorganic Lead Halide Perovskite Solar Cells. *iScience* **2020**, *23* (8).
17. Koh, T. M.; Shanmugam, V.; Guo, X.; Lim, S. S.; Filonik, O.; Herzig, E. M.; Müller-Buschbaum, P.; Swamy, V.; Chien, S. T.; Mhaisalkar, S. G.; Mathews, N., Enhancing moisture tolerance in efficient hybrid 3D/2D perovskite photovoltaics. *Journal of Materials Chemistry A* **2018**, *6* (5), 2122-2128.
18. Di Girolamo, D.; Pascual, J.; Aldamasy, M. H.; Iqbal, Z.; Li, G.; Radicchi, E.; Li, M.; Turren-Cruz, S.-H.; Nasti, G.; Dallmann, A.; De Angelis, F.; Abate, A., Solvents for Processing Stable Tin Halide Perovskites. *ACS Energy Letters* **2021**, *6* (3), 959-968.
19. Chang, Y.-H.; Lin, J.-C.; Chen, Y.-C.; Kuo, T.-R.; Wang, D.-Y., Facile synthesis of two-dimensional Ruddlesden–Popper perovskite quantum dots with fine-tunable optical properties. *Nanoscale Research Letters* **2018**, *13* (1), 247.
20. Choi, H. S.; Kim, H. S., 3D/2D Bilayered Perovskite Solar Cells with an Enhanced Stability and Performance. *Materials (Basel)* **2020**, *13* (17).
21. University, J. H. Plasma Cleaner: Physics of Plasma 2016. <https://labs.jhu.edu/wp-content/uploads/2016/04/All-About-Plasma-Cleaning.pdf>.
22. Ding, X.; Liu, J.; Harris, T. A. L., A review of the operating limits in slot die coating processes. *Aiche Journal* **2016**, *62*, 2508-2524.

23. Nicole Zander, D. P., Ben Stein *Oxidation of Polyethylene: A Comparison of Plasma and Ultraviolet Ozone Processing Techniques*; Defense Technical Information Center: 2009.
24. Annamalai, M.; Gopinadhan, K.; Han, S. A.; Saha, S.; Park, H. J.; Cho, E. B.; Kumar, B.; Patra, A.; Kim, S.-W.; Venkatesan, T., Surface energy and wettability of van der Waals structures. *Nanoscale* **2016**, *8* (10), 5764-5770.
25. Ji-Won, J.; Hyeok, J. E. E.; Hye-Won, S. E. O., Study of Nitrogen Plasma Treatment on Indium Tin Oxide Thin Films. *NPSM* **2020**, *70* (1), 103-106.
26. Nitrogen Plasma Effect On The Physical Properties Of Tin Oxide Thin Film. *Egyptian Journal of Solids* **2011**, *34* (1), 7-18.
27. Carvalho, M. S.; Kheshgi, H. S., Low-flow limit in slot coating: Theory and experiments. *AIChE Journal* **2000**, *46* (10), 1907-1917.
28. Ossila Slot-Die Coating: Theory, Design, & Applications. <https://www.ossila.com/en-pl/pages/slot-die-coating-theory>.
29. Saffari, M.; Soleimani, H. R.; Tagani, M. B., Quantum confinement and strain effects on the low-dimensional all-inorganic halide Cs₂XI₂Cl₂ (X= Pb, Sn) perovskites: A theoretical approach for modulating electronic and optical properties. *Physica E: Low-dimensional Systems and Nanostructures* **2020**, *124*, 114226.
30. Lin, C.; Li, S.; Zhang, W.; Shao, C.; Yang, Z., Effect of Bromine Substitution on the Ion Migration and Optical Absorption in MAPbI₃ Perovskite Solar Cells: The First-Principles Study. *ACS Applied Energy Materials* **2018**, *1* (3), 1374-1380.
31. Luo, L.; Zeng, H.; Wang, Z.; Li, M.; You, S.; Chen, B.; Maxwell, A.; An, Q.; Cui, L.; Luo, D.; Hu, J.; Li, S.; Cai, X.; Li, W.; Li, L.; Guo, R.; Huang, R.; Liang, W.; Lu, Z.-H.; Mai, L.; Rong, Y.; Sargent, E. H.; Li, X., Stabilization of 3D/2D perovskite heterostructures via inhibition of ion diffusion by cross-linked polymers for solar cells with improved performance. *Nature Energy* **2023**, *8* (3), 294-303.

CHAPTER 5

GENERAL CONCLUSIONS AND OUTLOOK

GENERAL CONCLUSIONS AND OUTLOOK

The increase in environmental concern has boosted the market of energy production from renewable sources. Investments in silicon solar panels grow each year and, if this trend is maintained, photovoltaic power will represent *ca.* 20 % of the global energy market by 2027.¹³⁴ This rise in interest on silicon-based devices also stimulates the growth of other photovoltaic technologies. Perovskite Solar cells (PSC), for instance, have quickly become a hot topic in the energy research field due to their advantages when compared with the silicon technology. First, perovskite presents benefits regarding the energy consumption for its production: perovskite is a synthetic material while silicon is extracted from nature and purified using very high temperatures (~ 1400 °C) and high-vacuum. The perovskite synthetic characteristics will also contribute for de-monopolization of the photovoltaic market by silicon-producing countries, where the environmental impacts associated with this extraction and purification processes are not adequately regulated.

Additionally, perovskite devices can be fabricated on flexible and lightweight substrates, using entirely solution-based processes at low-temperature that allow for the customization of the final design. Furthermore, perovskite photovoltaic technology is one of the most efficient at converting light into electricity and breakthroughs regarding stability and the transition into large-scale manufacturing are often reported, making it likely that PSC will enter the commercialization stage in the near future. Still, the presence of lead in PSC poses significant issues related to toxicity. Lead is a well-known toxic heavy metal with severe health

effects on the nervous system, and if the PSC life-cycle is not managed properly, serious environmental contaminations might happen. To address these issues, researchers and industry experts are actively working on developing lead-free alternatives or implementing strategies to minimize lead usage and enhance the environmental and public health of PSC technologies. However, this topic is out of the scope of this thesis.

In this Ph.D. work, a stepwise work plan was designed aiming for a low-cost, stable, and efficient PSC, with a manufacturing process compatible with mass production. To reach this goal, several stages of development were considered. First, the fabrication process of a n-i-p PSC with the structure glass FTO / mesoporous TiO_2 / compact TiO_2 / $\text{CsI}_{0.05}((\text{FAPbI}_3)_{0.83}(\text{MAPbBr}_3)_{0.17})_{0.95}$ / spiroOMeTAD / gold was optimized. The next task consisted in replacing the expensive and unstable gold electrode by a highly conductive carbon paper (sheet resistance of $0.5 \Omega \text{ sq}^{-1}$). This material consists of a network of $\sim 7 \mu\text{m}$ thick carbon fibers coated with a $\sim 40 \text{ nm}$ thick microporous layer of carbon black and graphite deposited by lamination.

Three different carbon papers were studied to assess the influence of their different properties (sheet resistance, surface roughness, flexibility, and polytetrafluoroethylene content) on the photovoltaic performance. The best performing carbon paper displayed a PCE of 12.9 %, corresponding to 89 % of the PCE obtained with the typical gold back-contact (relative PCE). This PCE and relative PCE were further improved to 13.9 % and 92 % by applying a charge extraction enhancer interlayer of 5 nm of gold. The contact between the carbon paper and the hole transport material (HTM) was demonstrated to be nearly ohmic, resulting in no V_{oc} loss when compared with gold back-contact behavior. Although PCE is compromised, using a carbon-based material as the electrode is definitely a better option than using gold, due to the carbon's lower cost, higher stability, and compatibility with easily scalable deposition processes with low energy consumption.

At this point, the research was directed towards indoor applications on flexible substrates, given the good photovoltaic performance of PSCs at this light range. Moreover, the market for flexible indoor photovoltaics is growing fast, representing an opportunity for perovskite technology. SAULE Technologies in Poland is one of the leading companies developing Perovskite Solar Modules on an industrial scale, and the following studies were developed in their facilities under their financing and supervision. First, the optimized architecture was adapted to match the low-temperature requirements (≤ 140 °C) of flexible devices and the perovskite composition was tailored to maximize absorption under low-light: planar+mesoporous TiO_2 was replaced by planar SnO_2 and the chosen perovskite composition was $\text{Cs}_{0.17}\text{FA}_{0.83}\text{Pb}(\text{I}_{0.7}\text{Br}_{0.3})_3$ (band gap of 1.71 eV). Three different structures were studied: one with spiroOMeTAD HTM and gold electrode; another with poly(3-hexylthiophene (P3HT) HTM and carbon electrode; and a final one without HTM (HTM-free) and with carbon electrode. The carbon papers were replaced by a commercial carbon paste for allowing a solution-based deposition compatible with a R2R production, and facilitate the future patterning for module fabrication.

A thorough opto-electrochemical characterization was performed on these three configurations, using hyperspectral imaging, photoluminescence, quasi-fermi level splitting calculations (based on pseudo-JV curves), external quantum efficiency, ideality factor (calculated using the Suns- V_{oc} plot), transient photocurrent/photovoltage decay, scanning electron microscopy and electrochemical impedance spectroscopy. The maximum PCEs obtained were: 30.9 % at 1000 lux and 30.0 % at 200 lux for the metallic electrode configuration; 25.4 % and 23.1 % at 1000 lux and 24.7 % and 22.3 % at 200 lux for the carbon-based electrode configurations with and without P3HT, respectively. Regarding stability, the carbon devices with and without P3HT kept 49 % and 84 % of their initial PCE after 1000 h under maximum power point tracking, respectively, while the gold device lost 77 % in the first 300 h of aging alone. The HTM-free carbon-

based device also withstood 1000 h at 85 °C with virtually no efficiency loss and demonstrated high resistance to both the bending test and moisture aging.

Finally, given the high stability, moderate efficiency, simple architecture and low fabrication cost of the HTM-free carbon device, this architecture was scaled up using a slot-die coating technique in ambient atmosphere and low temperature (≤ 65 °C), using a fixed speed of 1 m min^{-1} for mimicking a roll-to-roll (R2R) process. These settings were defined according to the manufacturing requirements of the new pilot-line of SAULE Technologies. The viscosity, surface tension after different surface treatments, and deposition parameters of each solution were studied using the low-flow limit plot associated with the slot-die coating technique. Following this strategy, it was concluded that, for all solutions, it is possible to obtain a stable meniscus and a resulting high-quality layer using the desired wet film thickness and set speed. The optimized procedure resulted in a PSC with a maximum PCE of 16.5 % at 1000 lux, which kept 92 % of its initial PCE after 550 h under maximum power point tracking. Also, by slot-die coating a 2D perovskite passivation layer (n-octylammonium iodide), the PCE was increased to 18.6 %, due to the reduced recombination trap-sites and enhanced charge extraction at that interface.

Overall, the final goal of increasing the technology readiness level of PSCs was attained by a stepwise work plan developed at two different research institutions. The final PSC design and manufacturing process are much closer to meeting the requirements for industrialization compared to the initial ones. Firstly, the gold layer used as an electrode was replaced by a cheap and stable carbon-based material; then, the glass substrate was replaced by a lightweight and flexible polymer, the HTM was removed, and the temperature of the entire process was kept below 120 °C; and finally, the whole structure was scaled up using slot-die coating in ambient atmosphere. To complete the transition into a R2R production at an industrial scale, however, there are still some issues pending further research. The main topics for future work are listed below:

- Although the main component of the solvent system used for the perovskite solution is non-hazardous (acetonitrile), one of the major priorities should be finding a greener alternative for the hazardous 2-methoxyethanol. Since large quantities of solvents are required for a large-scale continuous process, it is crucial to eliminate any solvents that pose risks to human health and the environment.
- Since N₂ plasma treatment requires vacuum, it can only be used in a batch (sheet-to-sheet) model. Thus, this surface treatment should be replaced with one compatible with R2R production, like UV/ozone. Another alternative is removing the surface treatment and adding a surfactant to the solution to adjust the surface energy level.
- The high viscosity of the commercial carbon paste used for the electrode makes it impossible to deposit by slot-die coating. Thus, the 20 m long R2R pilot-line acquired by SAULE Technologies will have a rotary screen-printer for carbon deposition. A high-priority task in the work that follows is to optimize this fabrication step.
- After the three previous tasks are complete, the stability and efficiency of the PSC can be enhanced by further optimization of the 2D capping/passivation layer, or by other strategies such as the use of additives in the perovskite, until the obtained values are good enough to proceed to the next stage of developments and begin operations in the pilot-line.
- The fabrication of large modules (instead of small cells) and their encapsulation are topics that must also be addressed to maximize the active area and durability of devices, and finally obtain a commercial perovskite solar product. The module fabrication (design, P1 and P2 parameters) and the encapsulation method are already being optimized at SAULE Technologies.